INFORMATION TO USERS

This manuscript has been reproduced from the microfilm master. UMI films the text directly from the original or copy submitted. Thus, some thesis and dissertation copies are in typewriter face, while others may be from any type of computer printer.

The quality of this reproduction is dependent upon the quality of the copy submitted. Broken or indistinct print, colored or poor quality illustrations and photographs, print bleedthrough, substandard margins, and improper alignment can adversely affect reproduction.

In the unlikely event that the author did not send UMI a complete manuscript and there are missing pages, these will be noted. Also, if unauthorized copyright material had to be removed, a note will indicate the deletion.

Oversize materials (e.g., maps, drawings, charts) are reproduced by sectioning the original, beginning at the upper left-hand corner and continuing from left to right in equal sections with small overlaps.

ProQuest Information and Learning
300 North Zeeb Road, Ann Arbor, MI 48106-1346 USA
800-521-0600

Design, Analysis and Implementation of Free-Space Optical Interconnects

Frédéric Lacroix

Department of Electrical and Computer Engineering
McGill University
Montréal, Québec, Canada
August 2001

A thesis submitted to the Faculty of Graduate Studies and Research in partial fulfillment of the requirements of the degree of Doctor of Philosophy

C'est là sans appui

Je ne suis pas bien du tout assis sur cette chaise
Et mon pire malaise est un fauteuil où l'on reste
Immanquablement je m'endors et j'y meurs.

Mais laissez-moi traverser le torrent sur les roches
Par bonds quitter cette chose pour celle-là
Je trouve l'équilibre impondérable entre les deux
C'est là sans appui que je me repose.

Hector de Saint-Denys Garneau

Abstract

Optical interconnects represent an attractive alternative technoiogy for the implementation of dense, high-speed interconnects, as they do not suffer from many of the problems plaguing electrical interconnects such as frequency-dependent crosstalk and attenuation.

However, optics has still not been accepted commercially as an interconnect technology. There is concern regarding the cost and complexity of the optomechanics needed to achieve the very fine alignments necessary to guarantee that the light emitted from the source actually falls on the receiver. The demonstration of a simple-to-assemble, dense and robust optical interconnect would constitute an important proof of the practicality of this technology. The photonic backplane demonstrator system presented in this thesis addresses these issues through a novel approach; the system uses slow Gaussian beams (f/16) and a clustered design to maximize misalignment tolerances. This in turn relaxes the positioning and packaging requirements for the components, thus simplifying assembly.

This thesis pursues two sets of complementary goals: the first set is concerned with the demonstration of some desirable optomechanical characteristics for optical interconnects such as passive alignment, repeatability and stability while the second set of goals is concerned with a verification of hypotheses often used in the design and implementation of optical interconnects. Such hypotheses are often used in practice to design optical interconnects despite the fact that little data exists in the literature to warrant their use. It

therefore makes good sense to spend some time verifying the accuracy of these models. This will provide a solid engineering foundation for the design of future systems.

Résumé

L'optique représente une alternative technologique attrayante pour l'implémentation d'interconnexions denses à haute-vitesse dans les systèmes électroniques distribués. L'utilisation de fréquences optiques (THz) pour transmettre l'information permet d'éviter les nombreux problèmes associés à l'utilisation de fréquences plus basses communes à l'électronique (GHz) tels que les problèmes d'atténuation du signal et de diaphonie dépendents en fréquence.

Par contre, l'optique n'est pas encore acceptée commercialement comme technologie d'interconnexion. Les tolérances de positionnement de tels systèmes sont généralement de l'ordre du micron pour les tolérances latérales et de l'ordre d'une fraction de degré pour les tolérances angulaires. L'alignement d'interconnexions optiques est une opération délicate nécessitant généralement des systèmes optomécaniques complexes et très dispendieux. Cela constitue une barrière au déploiement commercial de cette technologie. Le démonstrateur de bus photonique présenté dans cette thèse attaque ce problème de front en utilisant des faisceaux Gaussiens lents (f/16) ainsi qu'une technique de regroupement de plusieurs faisceaux autour de l'axe optique d'une lentille afin de maximiser les tolérances de positionnement.

Deux séries d'objectifs sont poursuivis dans cette thèse: 1) la première série concerne la démonstration de certaines propriétés optomécaniques souhaitables afin de rendre cette technologie commercialement attrayante telles que l'alignement passif, la stabilité mécaniques ainsi que le répétabilité d'insertion et d'extraction des composantes 2) la

deuxième série d'objectifs concerne la vérification d'hypothèses de design. Cette deuxième série d'objectifs permettra d'établir une base solide pour le design des prochaines générations d'interconnexions optiques.

Remerciements

La liste des personnes à remercier pour leur aide, appui ou support au cours de ces années d'études est trop longue pour qu'ils ou elles soient tous et toutes énumérées içi. Une thèse de doctorat telle que celle qui est présentée içi est presque toujours le résultat d'un effort collectif, même si une seule signature est apposée au bas du document. Mais voici, en vrac et en désordre, quelques remerciements:

J'aimerais premièrement remercier mon directeur de recherche, le professeur Andrew Kirk, pour son support infatigable tout au long de mes études graduées. Le système a été originalement conçu par le Dr. Brian Robertson. La méthode d'alignement interférométrique lui est également due. Une partie importante des résultats de cette thèse sont ainsi attribuables à sa rigueur et à sa créativité.

L'implémentation du système a été rendue possible par plusieurs personnes. Entres autres: Eric Bernier (conception optomécanique), Rhys Adams (assemblage du système et support moral), Daniel F. Brosseau (assemblage et conception de l'OPS), David Rolston (conception de la puce électronique), Micheal Ayliffe (responsable du grand TOUT). Les calculs de tolérances du chapitre 4 ont été faits par Xin Xue (calculs de diffraction scalaire) et Marc Châteauneuf (calculs d'optique géométrique). Merci bien sûr à tout le groupe de recherches en systèmes photoniques pour leur support et leur aide périodique ou continue.

Finalement, un gros merci à mes parents sans qui cette thèse n'aurait sûrement jamais été écrite!

Ce travail a été soutenu financièrement par l'ICRT (Institut canadien de recherches en télécommunications), par la chaire Nortel/CRSNG en systèmes photoniques, par le Conseil de Recherches en Sciences Naturelles et en Génie(CRSNG)(OGP0194547) ainsi que par le Fonds pour la Formation de Chercheurs et l'Aide à la Recherche (FCAR)(NC-1778).

Table of Contents

Associated Publications

The work reported in this thesis has been published or is being published in the form of the following :

Refeered Journal Publications:

F. Lacroix, E. Bernier, M. H. Ayliffe, F.A.P. Tooley, D. V. Plant, A G. Kirk, "Implementation of a Compact, Four-stage, Scalable Optical Interconnect for Photonic Backplane Applications", submitted to Apllied Optics

F. Lacroix, M.H. Ayliffe, and A. G. Kirk, « Tolerancing of Polarization Losses in Free-Space Optical Interconnect Systems », Optics Express, Vol. 7, No. 12, December 4 2000, Pages 381 - 460

F. Lacroix, M. Châteauneuf, X. Xue and A. G. Kirk, « Experimental and numerical analyses of misalignment tolerances in free-space optical interconnects », *Applied Optics*, Vol. 39, No. 5, 10 February 2000.

D.F.- Brosseau, **F. Lacroix**, M. H. Ayliffe, E. Bernier, B. Robertson, F. A. P. Tooley, D. V. Plant, A. G. Kirk, "Design, Implementation, and Characterization of a Kinematically Aligned, Cascaded Spot- Array Generator for a Modulator-Based Free-Space Optical Interconnect", *Applied Optics*, Vol. 39, No. 5, p. 733-745, February 2000

R.Iyer, Y.S.Liu, G.C.Boisset, D.J.Goodwill, M.H. Ayliffe, B.Robertson, W.M. Robertson, D.Kabal, **F. Lacroix**, and al., " Design, implementation and caracterization of an optical power supply spot-array generator for a four-stage free-space optical backplane", *Applied Optics*, Vol.36, No.35, 10 December 1997.

Refeered Conference Proceedings and Technical Digests:

F. Lacroix and A. G. Kirk, « Tolerance stackup effects in optical interconnect systems », Optics in Computing, Québec, Canada, 2000.

E. Bernier, **F. Lacroix**, M.H. Ayliffe, F. A. P. Tooley, D. V. Plant, and A. G. Kirk, « Implementation of a compact, four-stage, scaleable optical interconnect », Optics in Computing, Québec, Canada, 2000.

F. Lacroix, M. Châteauneuf, X. Xue and A. G. Kirk « Experimental and numerical analyses of misalignment tolerances in free-space optical interconnects », Optics in Computing, Snowmass, Colorado, 1999.

F. Lacroix and al., " Design and implementation of a four-stage clustered free-space optical interconnect", Optics in Computing Brugges, Belgium, 1998.

A.Kirk, F.Mathieu, **F. Lacroix** and al.," Two-Dimensional Optical Interconnects with Fiber Arrays", MOC/GRIN, Tokyo 1997.

A.Kirk, F.Mathieu, **F. Lacroix** and al., "Demonstration of a free-space optical broadcast network", Optics in Computing 1997.

Chapter 1: Introduction

The digital processing of information requires both circuits to perform logical operations on the data and devices to store and transmit the information from place to place. The insatiable demand for information in our society is exerting pressure on these processing, storage and transmission systems for them to process, store and transmit more and more data at ever faster rates. Electronic processing technology is being constantly improved to increase processing speeds. Technological shifts from electrical to optical technology have already been implemented to solve the problem of the limited bandwidth and high cost of electrical-based long-haul transmission systems. However, a severe imbalance is emerging between our ability to process (for example in an integrated circuit) and our ability to transmit data over short distances (i.e. in the millimeter to meter range). High-speed, short-distance interconnects are needed.

1.1 Current Interconnect Challenges

Ever since the invention of the integrated circuit in 1959, the semiconductor industry has sought to make chips that are faster, more complex and cheaper. In doing so, it has doubled the number of functions implemented on a chip approximately every eighteen months for the last thirty years [1]. The Semiconductor Industry Association (SIA) roadmap shown in table 1 outlines a variety of technology requirements on feature sizes, number of transistors, on and off-chip clock rates etc., that will have to be met to continue this increase [2].

Table 1. Semiconductor Industry Association Projections for Silicon ICs

Year	Gate Length (μm)	Number of Transistors (millions/cm^2)	On-Chip Clock (MHz)	Off-Chip Clock (MHz)	Number of Pads
1999	0.18	20	1250	480	1400
2000	0.165	28	1486	589	1800
2001	0.15	40	1767	722	2200
2002	0.13	54	2100	885	2600
2003	0.12	73	2490	932	3000
2004	0.11	99	2952	982	3400
2005	0.1	133	3500	1035	3800

The continuous downscaling of feature sizes or transistor gate length is the driving force behind the evolution in technology requirements outlined in table 1. It has a number of important consequences. More and more transistors can be integrated on a single chip. The number of output pads must therefore increase proportionately. The scaling in transistor channel length also decreases the switching speed meaning that transistors can operate at higher frequencies.

While transistors can operate faster as they are downscaled and can thus process information faster, it has been known for some time that metal-based interconnect lines do not scale so favorably. In fact, interconnect lines, whether of a resistive-capacitive (RC) or inductive-capacitive (LC) nature, possess an "aspect-ratio" limit meaning that the total bit rate that can be sent down a line is proportional to the cross-sectional area of the line divided by its length squared [3]. This means that scaling the line proportionately in cross-sectional area and length will not change its bit rate capacity. In fact, as feature sizes are reduced and transistors become smaller, interconnect lines tend to become longer, thus reducing their overall bit rate capacity. Bit-rates can still be increased

through the use of techniques such as repeatering, multilevel modulation or equalization [4] but recourse to these adds cost and complexity. The interconnect capacity might still not scale sufficiently to keep up with the increase in transistor processing capacity and density.

These factors are putting pressure on interconnect resources and mean that interconnect delays are becoming dominant in limiting information flow on and off-chip [4]. Already, system performance is dominated by the interconnect rather than by the processing speed of transistors in multi-chip systems. It is expected that interconnect problems will also soon limit information transfer on chip.

Interconnect limitations arise from two sources: 1) space constraints and 2) fundamental physical limits associated with the use of electrical signals to establish connections. The space constraints limit the number and density of interconnect lines and bondpads that can be placed on a chip or printed circuit board (PCB) of a given size and complicates the routing process while the use of electrical lines to transmit high speed data affects the electrical signal integrity (because of crosstalk, signal skew and termination problems) and thus limits the available bandwidth [4][5]. The interconnect technology must be changed.

1.2 Optics versus Electronics: Basic Considerations

The use of optical instead of electrical technology offers a number of potential advantages to solve these interconnect problems. While optics offers some advantages in terms of voltage isolation, timing accuracy and access to new architectures and

topologies, there are other, more fundamental reasons that drive the push towards optical technology. These reasons will be briefly reviewed here. Note that the arguments presented here are exposed in greater detail in [4] and [6].

It is important to emphasize that both electrical and optical interconnects use electromagnetic waves (and therefore photons) to carry signals. A distinction between optical and electrical interconnects therefore cannot be made by stating that one type uses photons and the other electrons to carry information.

The difference between optics and electronics lies in the wavelength or frequency or photon energy of the electromagnetic waves that carry the signal. Note that the terms wavelength, frequency and photon energy are all various ways of expressing the same physical characteristic as these quantities are related through the formulas $\nu\lambda = c$ (where ν is the frequency, λ is the wavelength and c is the speed of light) and $E = h\nu$ (where E is the photon energy and h is Planck's constant which is equal to 6.626×10^{-34} joule-sec). The frequency of the carrier used in optics is usually very high compared to the frequency of the waves used in electronics (500Thz compared to 10MHz-10GHz). This difference can equivalently be stated in terms of wavelength or photon energy by saying that optics uses wavelengths in the range of 500-1500nm or photons having an energy in the 1 electro-volt (eV) range while electronics uses wavelengths between 3cm and 30m and photon energies around 40neV - 40μeV.

These differences have important consequences. There are at least four advantages to using light as an information carrier: 1) no frequency dependent losses 2) no interaction between beams 3) no frequency dependent crosstalk and 4) ease of impedance matching. Other advantages like lower power consumption will not be discussed here.

1) The very high frequency of light means that there is little frequency dependent loss since the frequency of any modulation that can be applied to the signal is usually insignificant relative to the frequency of the carrier. In contrast, electrical RC or LC lines have intrinsic losses that are strongly dependent on the frequency used; through low-pass filtering effects for RC lines (the capacitance of the line has to be charged and this limits the frequency response) and the skin effect for LC lines (conduction takes place only on the surface at high frequencies).

2) Beams of light propagating in free-space or in dielectric media in general do not interact because the non-linear susceptibility is very small in such materials. The electric and magnetic fields composing the waves will thus superpose linearly and their propagation vectors will not be affected. However, note that nonlinear effects can appear when field intensities reach a certain threshold (the threshold varies greatly with the type of material).

3) Frequency-dependent crosstalk will appear because time-varying electric and magnetic fields can be induced in metallic materials due to the presence of free charges. Ampère's law states that a time-varying electric field will give rise to a current and a magnetic field

while Faraday's law states that a time-varying magnetic field will give rise to an electric field. This means that there will be electromagnetic induction between adjacent electrical lines transporting electromagnetic waves. The intensity of the fields that will be created is directly proportional to the frequency of the time-varying electric or magnetic field. This generates frequency dependent crosstalk.

4) Electrical lines and devices respond proportionately to the magnitude of the electric field of the wave traveling in them which means that impedances need to be matched at every termination point to prevent back reflections. The large photon energy of light leads to "quantum impedance conversion" that is impedances do not need to be matched between emitter and detector in optical interconnects because the current generated at the photodetector is dependent on the number of photons arriving and not on their electric field strength. The wave reflections that do occur as light travels through materials of different impedances can be virtually eliminated by the use of simple quarter wavelength resonators (anti-reflection coatings).

1.3 Optics versus Electronics: Architectural Impacts

The choice of optics as an interconnect technology will also have a significant impact on the architecture of the systems that can be constructed. The difference between optical wavelengths (500-1500nm) and electronic wavelengths (3cm to 30m) has major implications. These can be summarized as follows: 1) less severe diffraction effects 2) harder to implement arbitrary interconnection patterns but easier to implement global patterns and 3) easier beam splitting and combination.

1) The amount of diffraction suffered by a wave is proportional to its wavelength, which means that waves having a wavelength in the centimeter to meter range will diffract much more than waves having wavelengths in the micron range. In electrical systems the path from source to detector is almost always defined using a waveguide structure (except in radio systems). Waveguides are used to confine the electromagnetic waves to thin metal traces and direct them from point A to point B. If no waveguiding structures were used to confine the waves, they would rapidly spread out in space due to diffraction. Another consequence of diffraction is that waves cannot be focused to dimensions smaller than approximately one wavelength. This means that the minimum spot size that can be achieved in free-space using electrical wavelengths lies in the centimeter to meter range. This drastically limits the interconnection density that can be established and confines electrical interconnects to the role of low density interconnects such as radio systems.

Optical wavelengths being much shorter than electrical ones, the typical diffraction limited spot sizes of optical beams are in the micron range. Moreover, the beams may physically overlap as they propagate through free-space but this will not affect their propagation direction or characteristics. A simple lens can be used to angularly multiplex or demultiplex beams. Two dimensional interconnects can be established between two planes. Thousands of spots can potentially be imaged on a surface a few centimeters on the side. This provides access to huge spatial bandwidths.

2) One of the practical advantages of electrical interconnections is that it is relatively easy to construct arbitrary interconnection patterns as the signal lines are usually defined

using a lithographic process. Although diffractive optical elements or volume holograms can theoretically be used to establish arbitrary interconnection patterns in free-space as well, diffraction efficiency problems can be encountered when working with a large number of beams. However, it is easy to perform certain global mapping functions (mirroring for example) between a series of inputs and a series of outputs by using various bulk and micro-optical components [3]. Various algorithms such as Fourier transforms and sorting operations can thus be implemented [7].

3) Beam splitting (fan-out) operations are simpler to perform at the physical level in optics. Any fraction of power can be extracted from a beam by simply using a beam splitter or a diffractive optical element. It is thus easy to make multiple connections to a given signal "line" so that the data can be made available to multiple parts of a system. In contrast, this is relatively difficult in electronics as all terminations must be impedance matched in order to eliminate back reflections. Another disadvantage of electronics is that it is not possible to add new lines to tap the signal off an existing line without readjusting the impedance.

Beam combination (fan-in) operations are more difficult to perform optically because combining mutually incoherent optical beams will generally result in power loss. The constant radiance theorem states that if N identical and mutually incoherent optical beams are combined to form a single beam with the same cross-sectional area and the same numerical aperture as the incident beams, then the total optical power delivered into the resultant beam cannot exceed 1/N of the total incident power [8]. Thus, combining two

identical beams will generally result in 50% power loss. However, beam combination can be performed without loss when one of the parameters between the two beams differs (such as the polarization state or the wavelength).

In summary, optics represents a potential solution to many of the problems plaguing electrical interconnects. A free-space optics approach is particularly interesting because free-space provides access to huge two-dimensional spatial bandwidths.

1.4 Organization of the Thesis

This thesis will be concerned with the design and implementation of optical interconnects for use in linking electronic processing elements. Once the motivation for optical interconnects has been presented, the design of a point-to-point optical interconnect for a four node ring-based photonic backplane will be presented. This high-density interconnect design is thought to represent a good candidate for the construction of a passively aligned optical backplane. Note that the interconnect design was done by Dr. Brian Robertson [9]. The implementation of this interconnect led to the formulation of a series of questions that constitute the drive of the research that will presented in this thesis. In order to design the optical interconnect, a set of assumptions and simplifications were assumed. These simplifications were typical of many if not of all of the optical interconnects that have been implemented by various research groups to date, so although a specific system is implemented in this thesis, the questions raised and the answers found, will, it is hoped, be applicable to a wide range of systems.

The tolerances for the components of the interconnect were calculated assuming that diffraction of the beam due to clipping was not important. Chapter four will verify the validity of this assumption. It was also assumed that error accumulation or tolerance stackup effects were not important. Chapter five will try to answer whether this is the case or not. Chapter six will verify that power losses due to imperfections in the polarization properties of the components do not degrade the system performance. Chapter seven will be concerned with the implementation and characterization of the point-to-point interconnect described in chapter three. This will experimentally confirm of infirm the design hypotheses.

1.5 Original Contributions

The original contributions presented by the author in this thesis are:

1) First implementation of a representative portion of a scalable, clustered, ring-based optical interconnect. The interconnect provides 1024 optical channels to each chip. It is one of the most dense optical interconnects ever built.
2) First analysis of the accuracy of various numerical models when calculating misalignment tolerances in an optical interconnect. First comparison of numerical results with experimental results.
3) First analysis of tolerance stackup effects in free-space optical interconnects.
4) First tolerancing of polarization losses in free-space optical interconnects. First analysis of polarization tolerance stackup effects.

1.6 References

[1] Robert R. Schaller, "Moore's law: Past, present and future", IEEE Spectrum, p. 52-59, June 1997.

[2] International Semiconductor Manufacturing Technology, http://www.sematech.org/public/publications/index.htm

[3] J.W. Goodman, "Optical Interconnections for VLSI Systems", *Proceedings of the IEEE*, Vol. 72, 850-866, 1984.

[4] D.A.B. Miller, "Physical Reasons for Optical Interconnections", *International Journal of Optoelectronics*, Vol. 11, No.3, 155-168, 1997.

[5] F.A.P. Tooley, "Challenges in Optically Interconnecting Electronics", *IEEE Journal of Selected Topics in Quantum Electronics*, Vol. 2, No 1, April 1996.

[6] D. A. B. Miller, "Rationale and Challenges for Optical Interconnects to Electronic Chips", To be published in Proceeding of the IEEE.

[7] H. Scott Hinton, "An Introduction to Photonic Switching Fabrics", Plenum Press, New York, 1993.

[8] Joseph W. Goodman, "Fan-in and fan-out with optical interconnections", *Optica Acta*, Vol. 32, No. 12, p 1497-1507, 1985.

[9] B. Robertson, "Design of an Optical Interconnect for Photonic Backplane Applications", *Applied Optics*, Vol. 37, No. 14, 10 May 1998.

Chapter 2: Optical Interconnect Technologies

2.1 Introduction

This chapter explores the design choices that must be made when using optics as an interconnect technology. Its purpose is to present enough background information so that the reader will be able to clearly understand the issues discussed in the following chapters. A brief review of the systems implemented to date by various research groups is also presented.

Figure 1 below illustrates the standard interconnection hierarchy and indicates the required interconnection lengths and the maximum bit rate achievable with electrical interconnects (non-transmission lines). The illustration is drawn from [1]. Although the research dates from 1995, and electrical technology has since then improved, it nonetheless illustrates the fact that the maximum bit rate achievable decreases with distance and that there is a limit to the bit rate that can be achieved at a certain distance when using electrical technology.

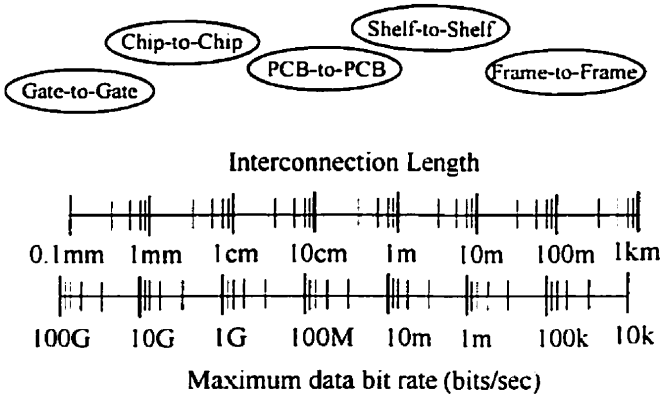

Figure 1. Interconnection Hierarchy of Digital Systems with Typical Lengths and Data Rates.

Optical interconnects can be implemented throughout this interconnection hierarchy. They can be implemented using either waveguides, free-space or a combination of both to guide the optical beam from one point to another. Modulator or emitter type devices can be used as sources. These design choices influence the capabilities of the technology. Although optical technology constitutes a very interesting candidate for the establishment of high speed, high-density interconnects, there is still some skepticism regarding the commercial potential of this technology. This is essentially related to issues of packaging and implementation. Easy-to-assemble, dense, low-cost and robust interconnects have yet to be demonstrated.

2.2 Guided-Wave versus Free-Space

It is important to establish a clear distinction between the guided-wave and free-space approaches when speaking of optical wave propagation. The guided-wave approach makes use of a support medium to confine and guide the waves to their destination whereas the free-space approach relies on diffraction and refraction in bulk optical components to focus the beam on to the detectors.

Both approaches have been used successfully to implement long range point-to-point or point-to-multipoint links. Commercial products using both approaches are available. Guided-wave optics has been used to establish long-range high-speed point-to-point links using dielectric optical fibers as the waveguide. Single wavelength fiber-based systems operating at 10Gb/s data rates per wavelength are already deployed and 40Gb/s systems should be available soon [2]. Parallel optical interconnects using a linear array of 12

optical fibers to interconnect as many channels are also available [3]. Free-space rooftop-mounted systems operating at optical frequencies and providing last-mile access to data networks are now starting to be deployed [4].

Most products available so far using guided-wave or free-space approaches provide long-haul point-to-point or point-to-multipoint links using a single spatial channel. However, short range interconnects between electronic processing elements require access to multiple channels due to the large number of pin-outs of optoelectronic chips. Techniques such as time-division multiplexing (TDM) or wave-division multiplexing (WDM) can be employed to increase the number of channels. However, these require multiplexers which add cost and increases latency in the system. Implementations offering multiple spatial channels (also known as space-division multiplexing (SDM)) are desirable. No commercial products providing two-dimensional arrays of channels are available although much research has been performed in this area (see section 2.4).

A recent approach to guided-wave interconnects uses fiber image guide-based interconnects (FIGs). Fiber image guides consist in a bundle of many thousands of fibers. Each fiber acts as a pixellated image point so each beam is guided in multiple fibers. This technology is interesting to implement point-to-point interconnects because only two alignment steps are necessary: the alignment of the FIG relative to the source and the alignment of the FIG relative to the detectors. However, tradeoffs are present between spot size and power uniformity (each beam must be transmitted through many fibers to insure that power levels will remain uniform if the FIG is misaligned). This

limits the density of channels that can be transmitted. A system possessing a channel spacing of 250μm has been demonstrated [6]. Also, the bandwidth-length products are limited because of multimode dispersion, although modulation speeds up to a 1Gb/s have been demonstrated [6]. Note that this technology is also limited to implementing point-to-point interconnects as beam splitting and combination operations cannot be performed inside a FIG.

In contrast, the spatial bandwidth of free-space systems is limited by the spot size provided by the optical system. Typically, if each output spot that can be resolved in the image plane is equated to a pin-out, then more that 10000 pin-outs can theoretically be achieved in an area of 25mm diameter using a 10mm focal length lens at 850nm if the optical system is diffraction limited. Channel spacings of 90μm have been demonstrated using free-space optical interconnects [5]. In contrast, dielectric optical fibers possess an outer cladding diameter of 125μm. This dictates the minimum channel spacing achievable. Free-space interconnects are therefore at an advantage in terms of channel density because no bulky waveguides need be used to guide the light. They can be implemented using either compound lenses or arrays of microlenses or a mix of both.

2.3 Emitters versus Modulators

It is also necessary to make the distinction between emitter and modulator based-interconnects. Emitter-based systems employ arrays of directly modulated vertical-cavity surface-emitting lasers (VCSELs) or light-emitting diodes (LEDs) to create the array of optical beams propagating in the interconnect. Modulator-based systems use light-

sensitive diodes flip-chipped on to the silicon chip to modulate an array of continuous wave (CW) constant power beams impinging on them.

From an optical design perspective, the main difference between emitter and modulator-based systems is related to the complexity of the optical system. Modulator-based systems need to combine and route three arrays of optical beams: one array of CW beams that illuminate the modulators, one array of beams modulated and reflected from the chip and one array coming in from the previous chip and directed to the detectors. This renders system design and alignment more difficult as three arrays of beams must be registered to the same plane. Emitter-based systems need only to route and combine two arrays of optical beams. This simplifies system design and alignment.

The use of VCSELs is therefore attractive from an optical design perspective, however, their integration to conventional silicon technology remains a problem [7]. They also often exhibit polarization instability and multimode behavior at high power, rendering the design of an efficient optical system challenging. Intense research is focussing on solving these problems. If this is achieved, VCSELs should become the technology of choice to implement optical interconnects.

2.4 Brief Review of Previous Research

Much of the groundbreaking work in free-space optical interconnect technology was performed by researchers at AT&T Bell Laboratories [8, 10] in the early 1990s. They used optical interconnects to perform image mapping operations between optoelectronic chips inside telecommunication switching systems. Various switching

networks such as crossbars and banyans were implemented using self-electro-optic-effect devices illuminated by an external laser. A conclusion that can be drawn from their work is that alignment issues are critical in free-space optical interconnects because of the small size of the beams normally used (a few hundred microns in diameter). Components must often be aligned to a few microns precision laterally and fractions of a degree angularly in order to guarantee that the beams fall on the detectors. It is difficult to do this in a cost-effective fashion. Packaging and alignment issues are the biggest obstacle preventing free-space optical interconnects from gaining widespread commercial acceptance [7]. Researchers at AT&T were the first to demonstrate the usefulness of an "optical breadboard" based approach, that is, the use of a baseplate as a platform to align all the optical and optoelectronic components.

Since then, optical interconnects have been demonstrated at many levels of the interconnect hierarchy. These include: work at McGill University on systems using modulator [11, 12] or emitter [13] technology to interconnect PCBs at the backplane level and refining the baseplate-based approach pioneered at AT&T, work at George Mason University [14] and the University of San Diego [15] on systems implementing chip-to-chip interconnects and work at Heriot-Watt on sorting systems [16].

Recent work at NTT [17] uses VCSELs and adjustable prism arrays to actively align the beams onto the detectors. Such actively aligned systems could potentially solve packaging and alignment issues. Another approach described as planar optics [18] uses the precision afforded by lithographic etching processes to define various optical

components such as lenses and gratings on a glass substrate. The components are used in reflection mode and the beams propagate inside the substrate. The components in such systems are therefore "pre-aligned" to sub-micron precisions.

Some guided-wave systems employing arrays of fibers [3] or image guides [6][19] have also been demonstrated. Such systems dramatically reduce packaging and alignment issues however, channel density is reduced compared to free-space systems.

The free-space optical interconnect presented in this thesis [12] attacks the alignment problem at a fundamental level by designing the interconnect to be intrinsically misalignment tolerant. It constitutes a very dense free-space interconnect using modulator-based emitters.

2.5 References

[1] R. A. Nordin, W. R. Holland, M. A. Shahid, "Advanced optical interconnection technology in switching equipment", *Journal of Lightwave Technology* , **13**, p. 987-994 (1995).

[2] Nortel Networks Corporation www.nortelnetworks.com

[3] Paroli from Infineon Technologies AG www.infineon.com

[4] Terabeam Corporation www.terabeam.com

[5] E. Bernier, F. Lacroix, M. H. Ayliffe, F. A. P. Tooley, D.V. Plant, "Implementation of a compact, four-stage, scalable optical interconnect", Proceedings of Optics in Computing 2000, R. A. Lessard, T. Galstian editors, SPIE Vol. 4089 (2000) 0277-786X.

[6] T. Maj, A. G. Kirk, D. V. Plant, J. F. Ahadian, C. G. Fonstad, K. L. Lear, K. Tatah, M. S. Robinson, and J. A. Trezza, "Interconnection of a two-dimensional array of vertical-cavity surface-emitting lasers to a receiver array by means of a fiber image guide", *Applied Optics*, Vol. 39, No. 5, 10 February 2000.

[7] F. A. P. Tooley, "Challenges in optically interconnecting electronic", *IEEE Journal of Selected Topics in Quantum Electronics*, Vol. 2, No. 1, April 1996.

[8] F.B. McCormick et al., "Experimental investigation of a free-space optical switching network using S-SEED's", *Applied Optics*, Vol. 31, 5431-5446, 1992.

[9] F.B. McCormick et al., "Six-Stage digital free-space optical switching network using symmetric self-electro-optic-effect devices", *Applied Optics* 32, pp5153-5171, 1993.

[10] F.B. McCormick et al., "Five-stage free-space optical switching network with field-effect transistor self-electro-optic-effect-device smart-pixel arrays", *Applied Optics*, Vol. 33, No. 8, 10 March 1994.

[11] D.V. Plant et al., "An Optical Backplane Demonstrator System Based on FET-SEED Smart Pixel Arrays Diffractive Lenslet Arrays", *IEEE Photonics Technology Letters*, Vol. 7, No. 9, September 1995.

[12] B. Robertson, "Design of an optical interconnect for photonic backplane applications", *Applied Optics*, Vol. 37, No. 14, 10 May 1998.

[13] D.V. Plant et al., "A 4x4 VCSEL/MSM Optical Backplane Demonstrator System", *Applied Optics*, Vol. 35, No. 32, 10 November 1996.

[14] Michael W. Haney, Marc P. Christensen, Predrag Milojkovic, Jeremy Ekman, Premanand Chandramani, Richard Rozier, Fouad Kiamilev, Yue Liu, and Mary Hibbs-Brenner, "Multichip free-space global optical interconnection demonstration with integrated arrays of vertical-cavity surface-emitting lasers and photodetectors", *Applied Optics*, Vol. 38, No. 29, 10 October 1999.

[15] Xuezhe Zheng, Philippe J. Marchand, Dawei Huang, and Sadik C. Esener, "Free-space parallel multichip interconnection system", *Applied Optics*, Vol. 39, No. 20, 10 July 2000.

[16] S.M. Prince et al., "Implementation of Optical Perfect-Shuffle Module", *Applied Optics*, Vol. 34, No. 11, 10 April 1995.

[17] Katsuhiko Hirabayashi, Tsuyoshi Yamamoto, Shinji Matsuo, and Shigeki Hino, "Board-to-Board Free-Space Optical Interconnections Passing through Boards for a Bookshelf-Assembled Terabit-Per-Second-Class ATM Switch", *Applied Optics*, Vol. 37, No. 14, 10 May 1998.

[18] J. Jahns, "Integrated Free-Space Optical Interconnects for Chip-to-Chip Communications", *Massively Parallel Processing*, 1998. Proceedings. Fifth International Conference on , 1998 , Page(s): 20 –23.

[19] J. Ai and Y. Li, "Polymer fiber image guide circuits that incorporate free-space add-drop components", *Applied Optics*, Vol. 38, No. 29, 10 October 1999.

Chapter 3: Optics and Optomechanics for a Photonic Backplane.

3.1 Introduction

Although the use of optical technology to implement interconnects would eliminate or alleviate many of the fundamental problems currently facing electrical interconnects, there is still skepticism regarding the practicality of this technology. Much of this skepticism is related to implementation issues, in particular, the cost and complexity of the optomechanics often needed to align such systems is of concern. The demonstration of a simple to assemble, mechanically stable optical interconnect would accordingly go a long way towards proving not only the theoretical benefits of optical interconnects but also the practicality of this technology. The photonic backplane system presented in this thesis directly addresses those concerns. The goals of the demonstrator are listed below:

1) Passive alignment of the optical modules within the supporting optomechanical structure. This would guarantee simplicity of assembly. Modules could be simply inserted into the optomechanical structure.
2) Repeatable insertion and extraction of the modules making them easily replaceable in case of failure (this is especially important for the Optoelectronic Chip Module as it houses an active device).
3) Stability. The system stays aligned without needing adjustment once optimal alignment has been achieved.

However, this thesis also pursues another set of goals, which are more academic in nature. That is, the photonic backplane presented in this chapter is also used as a platform to test hypotheses related to design and assembly issues. These play a key role when designing complex optical systems such as the one presented here. If the demonstrator does not meet the three goals listed above, then the design hypotheses must be questioned. The assumptions verified in chapter four to six of this thesis are:

1) Gaussian beam propagation theory is accurate to calculate misalignment tolerances.
2) There is no simultaneous interaction between multiple tolerance parameters when assembling a system. Tolerance stackup is negligible.
3) Power losses due to imperfections in components that affect the state of polarization are negligible.

Such design hypotheses are commonly used in the optical interconnect community despite the fact that little data exists to support their use. This will provide a solid foundation upon which to design optical interconnects and will be of general interest to the optical interconnect community.

Note that the optical design of the point-to-point interconnect was done by Dr. Brian Robertson and the optomechanical design was done by Eric Bernier. A part of the work presented in this chapter is thus their work. The optical design of the interconnect is presented in [1]. A brief presentation of the optomechanical design is given in [2].

However, part of the material (such as issues related to the implementation of the optical system) has not been published before. It was therefore judged imperative to present this material here in order to acquaint the reader with the details of design necessary to understand the finer points of the implementation of the system (presented in chapter 7).

This chapter presents an overview of the design of the optics and the optomechanics for a four node photonic backplane. It begins with an overview of the design of the point-to-point free-space optical interconnect used to interconnect the optoelectronic chips at the backplane level. The grouping of the components into modules as well as the optomechanics for the alignment and support of the modules to form a four node photonic backplane are also briefly presented. An analysis of the scalability of the optical interconnect design concludes the chapter.

3.2 Optical Design Overview

The photonic backplane presented in this thesis is a specific implementation of the *Hyperplane* architecture [3]. The *Hyperplane* architecture seeks to provide a large quantity of interconnections among printed circuit boards (PCBs) for packet switching networks and massively parallel processing systems. Specifically, parallel electrical data in packet form is converted into parallel optical data and placed onto specific channels in the optical backplane. The optical data reaches its destination (or destinations) and is then converted back into electrical data. Since address headers are incorporated into the packet, address recognition is performed at each optoelectronic chip and the packet is routed to the correct PCB. Devices with routing abilities and incorporating photosensitive diodes connected to logical circuitry are termed "smart pixels". The

Hyperplane architecture can be configured to implement a large variety of interconnection networks such as 2D and 3D meshes, crossbars and shuffle networks. This allows application dependent interconnection schemes to be implemented, thus improving performance. Figure 1 presents a high-level diagram of an optical backplane.

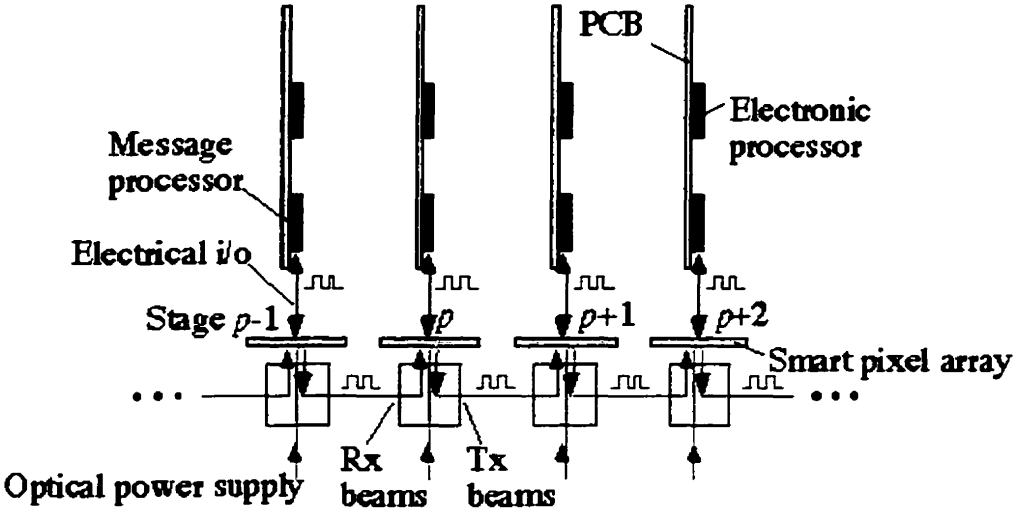

Figure 1. Schematic Diagram of an Optical Backplane

Arrays of constant power optical beams coming from the optical power supply are intensity modulated at the smart pixel array plane and routed from one stage to the next using a point-to-point optical interconnect.

The reader will have noticed that figure 1 explicitly shows a modulator-based system as an external optical power supply is illustrated. Modulators were used to intensity modulate the beams in this system. While the use of emitters such as vertical-cavity-surface-emitting-lasers (VCSELs) is attractive because they eliminate the need to route and combine three arrays of optical beams and decrease the system complexity, their integration to conventional silicon technology remains a challenge, especially for large arrays of VCSELs [4]. They also often exhibit polarization instability and multimode

behavior, rendering the design of an efficient optical system challenging. Modulators were chosen in this demonstrator system because large arrays (32x32) of devices with good characteristics have been demonstrated [5] and were available. However, a major part of the work presented in this thesis could be directly applied to a VCSEL-based optical system.

A four-stage (4 PCBs), ring based configuration (the last PCB is linked optically to the first) was chosen for the demonstrator. Using a ring configuration is advantageous because the data that is dropped at any node can be sent to any other node through multiple hops, even if the system is not bi-directional. This simplified the interconnect optical design as only a uni-directional interconnect needed to be used.

One of the key advantages of free-space optical interconnects is that use of this technology permits access to a high number of spatial channels. To make a convincing technology demonstration, a system must therefore possess a high channel density. This density criterion was met by designing a clustered system employing arrays of diffractive minilenses where many optical beams pass through the same minilens. This scheme achieves both a high channel or window density (2500 windows/cm^2) and a moderate window size (40μm). The smart pixel arrays (also termed the optoelectronic VLSI chips) are composed of optically sensitive GaAs/AlGaAs P-I-(MQW)-N diodes hybridized onto standard CMOS. The silicon CMOS chip incorporates logical circuitry enabling optical data to be transmitted, received or re-transmitted at each node [6].

Figure 2 presents a schematic diagram of the interconnect design. The interconnect implements a point-to-point link between the modulators located at stage 1 and the detectors at stage 2. A total of 512 optical beams (256 channels since the data is encoded using dual-rail logic) arranged in 32 4x4 clusters are relayed through 8x8 arrays of large (800μm) and long focal length (8.5mm) diffractive minilenses. Telecentric imaging is used since this increases misalignment tolerances (defocus errors will not translate to lateral misalignments on the modulators or detectors since the chief ray is perpendicular to each plane). The interconnect uses a beam combination method based on the use of polarization optics. Polarization variations induced by quarter-wave plates are used to route the beams between stages with the help of reflections off polarizing beam splitter (PBS) cubes and mirrors located on the Patterned Mirror Grating element (PMG) composed of alternating strips of diffractive fanout grating and mirror. The design of the interconnect is presented in detail in [1].

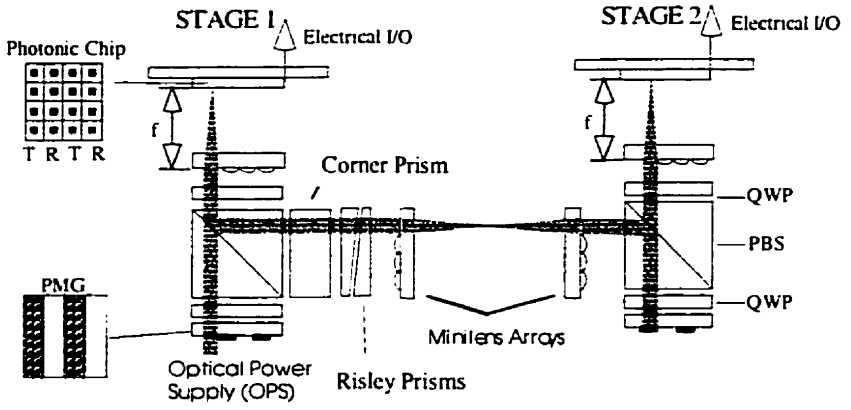

Figure 2. Schematic Diagram of the Interconnect Design

The details of the Optical Power Supply used to generate the input 4x8 array of collimated beams are not shown here. This subsystem is fully described in [7] and is composed of a polarization maintaining fiber, some collimation optics, a 4x8 diffractive fanout grating, a Fourier lens and a minilens array. Risley prisms and tilt plates are also included to allow adjusting the beam lateral and angular position.

A cascaded array generation technique is used to produce the 512 beam array incident on the modulators: a 4x8 array is first generated by the diffractive fanout present in the Optical Power Supply and each spot in this array is then fanned out by the Patterned-Mirror Grating into a 4x4 sub-array. A total of 512 optical beams pass through the PBS/QWP assembly and are focused by a minilens array placed one focal length in front of the modulators. Those beams are then modulated and sent back into the system where they pass through three minilens arrays arranged in a 4f relay configuration and reflect off stripes of mirror located on the PMG to be focused again on the detectors by another minilens array. Each Gaussian beam has a 13.1μm $1/e^2$ focused spot radius at the

modulator and detector planes. This 39.3μm diameter should be well accommodated by the oversized 50μm round modulators and the 70μm square detectors. Note that the interconnect is represented in two dimensions whereas it is actually of a three dimensional nature: the function of the Corner Prism element is to deviate the beams by 90° with the help of total internal reflection (in reality, the beams would actually propagate "into" the piece of paper) . The Risley prisms are used for beam steering purposes.

3.3 Modularization

The optical backplane is composed of four point-to-point optical interconnects (such as shown in figure 2) arranged in a uni-directional ring configuration. The optical system interconnecting the four OE-VLSI chips uses a total of 48 optical components. These components occupy a 55x55mm area and are housed in a 7cm on a side square baseplate. All 48 components must be aligned relative to each other in all six degrees of freedom. The alignment process can be simplified by grouping the components into pre-aligned modules. This reduces the number of degrees of freedom and relieves the tolerances on the optomechanics. A detailed tolerance analysis has been performed and the partitioning of the components into modules chosen so as to maximize the system misalignment tolerances. This analysis is not presented here but can be found in [8]. The grouping of components is done such that the intra-module alignment requirements are more severe than the inter-module alignment requirements. However, note that severe intra-module alignment requirements are not critical as the modules can be assembled independently using active alignment techniques and then passively aligned in the baseplate. Modularization thus shifts the critical active alignment steps away from the

system integration phase to the module assembly phase. In this way, it is hoped that the system can be assembled in a passive fashion, i.e. that the modules can be simply inserted in the baseplate to effect the final alignment. This would constitute a very interesting result and would demonstrate the practicality of this technology.

The system has been separated into four modules: Optical Power Supply (OPS), Beam Combination Module (BCM), Chip Module and Relay Module. The partitioning has been chosen so as to produce misalignment tolerant, easy to assemble and compact modules. Figure 3 presents a diagram of the module partitioning in the interconnect.

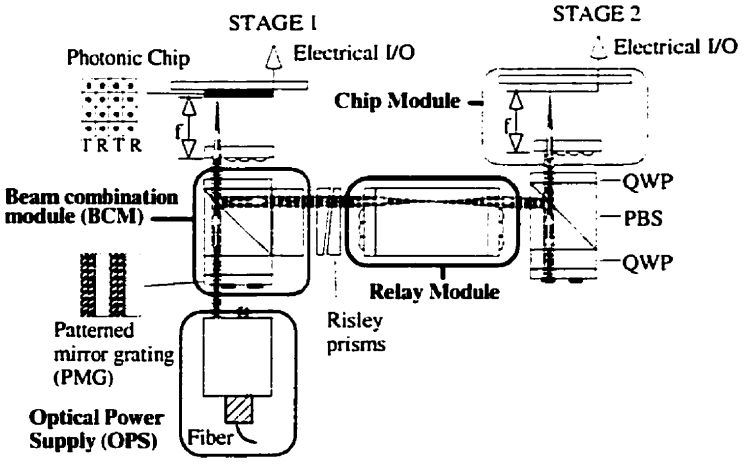

Figure 3. Diagram of the System Partitioning

Notice that the bottom quarter-wave plates are thicker to fill the empty space between the PMG and PBS and that a block of high-index glass has been added to provide mechanical support to the two minilenses composing the telecentric relay.

3.3.1 Optical Power Supply Module

A layout of the OPS components as well as the associated optomechanics is presented in Figure 4. A Gaussian beam output from a single-mode fiber is first

collimated to a $3\omega_0$ diameter of 1.75mm with the help of a low-aberration compound lens composed of an aspheric lens and a negative achromat. A quarter-wave plate oriented at 45° with respect to the linear p-polarized beam output by the PM fiber is used to produce right-hand circular polarization before the beam is fanned out to a 4x8 matrix by the binary-phase grating. Proper collimation of the matrix is insured by the use of a properly spaced Fourier lens minilens array combination. The Risley prisms are present to angularly and laterally steer the beams onto the modulators.

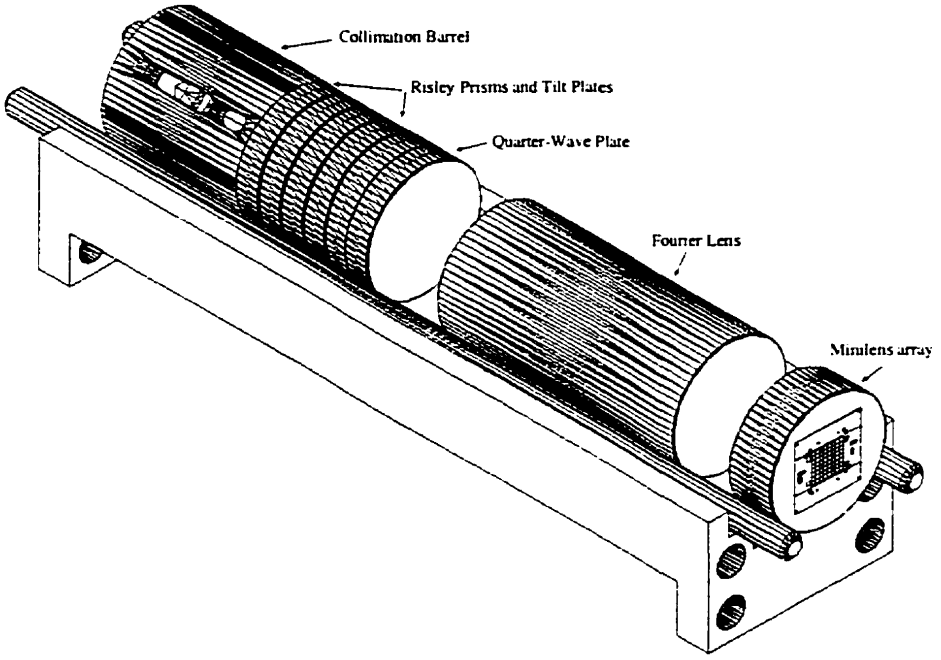

Figure 4: Layout of the OPS Module

3.3.2 Beam Combination Module

The BCM is a polarization-based unit designed to combine and route three arrays of beams: the continuous-wave (CW) spot array of beams incoming from the OPS and directed to the modulators, the modulated spot array reflected from the modulators and directed into the relay module and finally the spot array incoming from a previous stage

and directed to the detectors. It is composed of five elements: a patterned mirror-grating (PMG), two quarter-wave plates (QWP), a polarizing beam splitter (PBS) and an Interface Plate (IP). These various elements are assembled together as shown in figure 5.

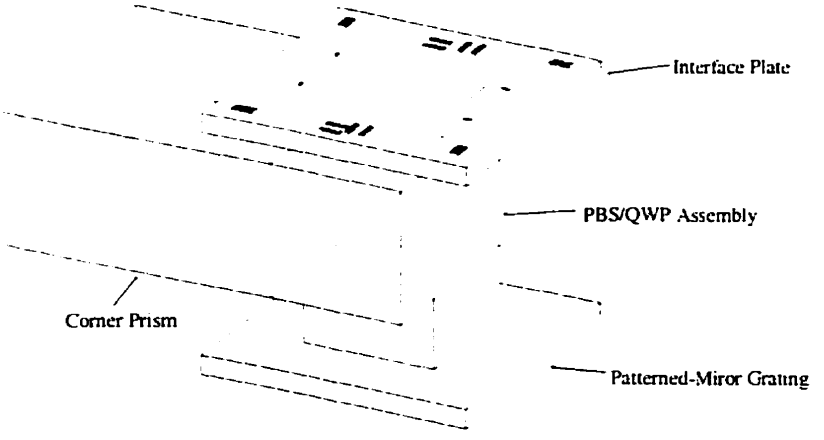

Figure 5. Drawing of BCM Module.

Note that the Corner Prism is not attached to the BCM but is mounted separately in the baseplate.

3.3.3 OE-VLSI Chip Module

The chip module packages the OE-VLSI chip with a minilens array in a module that can be repeatedly inserted in and out of the interconnect. Repeatable removal and insertion of the optoelectronic components is essential to insure that the system is easily serviceable once assembled. Figure 6 shows a schematic drawing of the Chip Module.

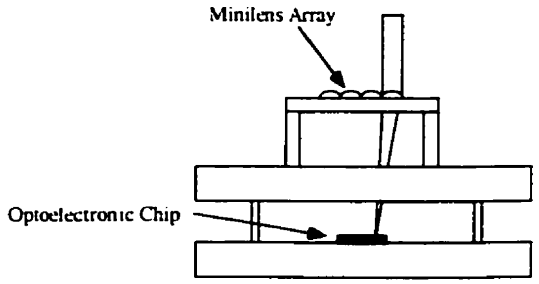

Figure 6: Schematic Drawing of the Chip Module.

3.3.4 Relay Module

The Relay Module shown in figure 7 is an assembly composed of an optical spacer (which is simply a block of high-index glass that provides mechanical support) and two minilens arrays. The minilens arrays are separated by a distance of 2f in order to constitute a telecentric relay.

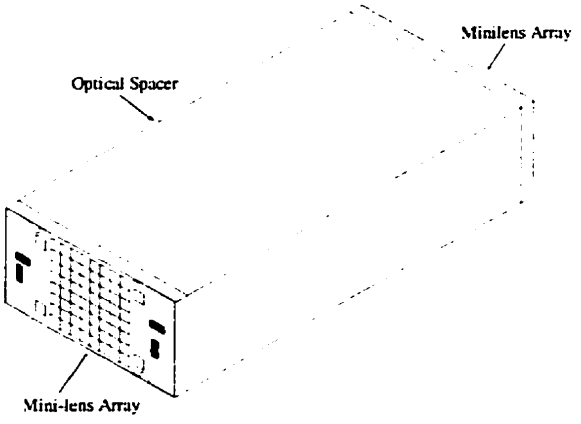

Figure 7. Diagram of Relay Module.

3.4 Optomechanics

The baseplate acts as the support structure for the entire optical system. All components and modules are attached to the baseplate or mounted into cells that rest on

the baseplate. Figure 8 shows an exploded view of the optical backplane. The baseplate is organized in the following manner: four through holes are machined at the corners and are linked by rectangular slots milled into the baseplate. The BCM module is aligned and mounted within the through hole. The OPS and Chip Modules are then aligned with respect to and connect to the BCM on either side of the baseplate.

Note that the baseplate was designed to fit in an industry standard U3 frame (13.97cm wide and 37.465cm deep). This is a self-imposed design criteria designed to show that the optical layer can be incorporated inside an electrical backplane chassis and is thus backward compatible with existing technology. Most optical parts were clamped in the baseplate using brass clamps. These clamps were designed to be flexible enough such that they would not damage the parts but sufficiently rigid to hold them in place. When the system alignment is complete, the optical parts are locked into position using UV curable adhesive. The Risley prisms are mounted into magnetic steel cells and maintained in place by magnets fixed to special slots machined in the baseplate. The OPSs are solidly fixed to the baseplate by using two machine screws inserted in the back of the baseplate.

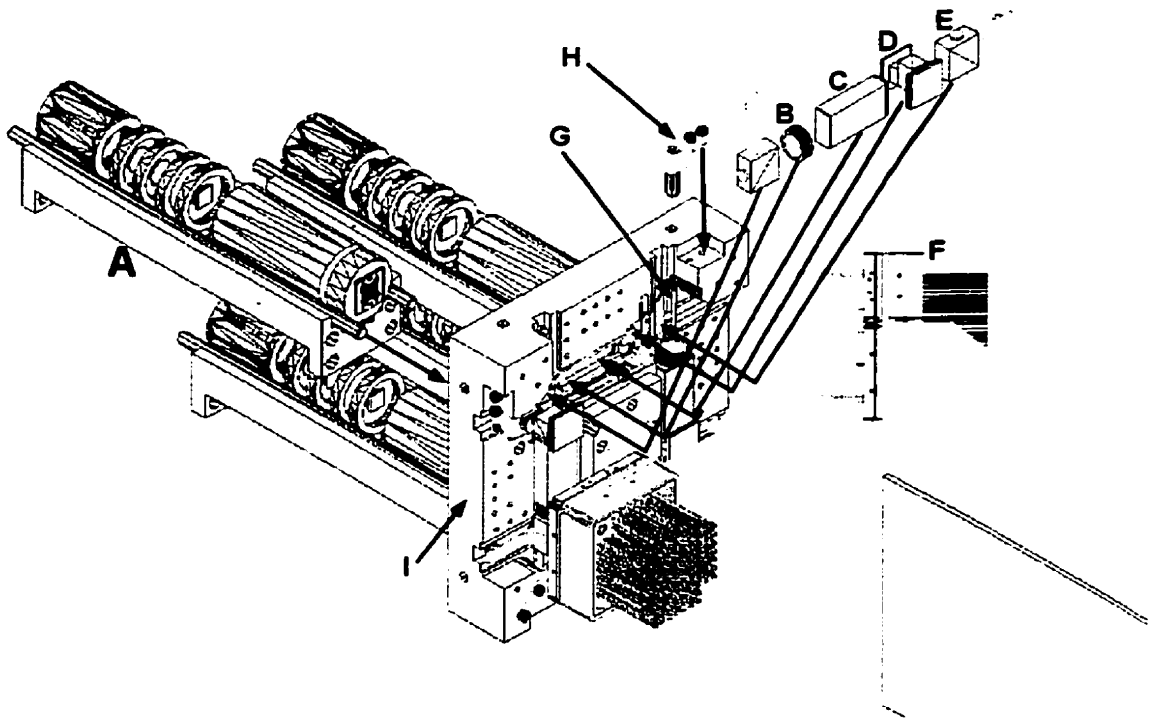

Figure 8. Drawing showing exploded 3D view of backplane.

(A: Optical Power Supply; B: Risley Prisms; C: Relay Module; D: Beam Combination Module; E: Corner Prism; F: OE-VLSI Chip Module; G: Hardened Steel rod; H: Adjustment screw; I: Baseplate)

Precision ground rods (G in figure 8) are positioned at the bottom of the rectangular slots milled into the baseplate. These rods are used as support structures to position the components and modules mounted into the baseplate such as the Corner Prism, the Risleys and the Relay Module. They define lines on which modules and components can be semi-kinematically aligned. In addition, these rods bridge part of the BCM positioning holes. The tolerance on the rod diameter is extremely severe (±5μm). This ensures that a minimum amount of tilt will be introduced when positioning the

components and modules. Such a scheme also has the advantage that it smooths any irregularities present in the milled baseplate groove.

The baseplate was fabricated in aluminium alloy 6061. Aluminium is a good material to use, as it is one of the easiest to machine and has a high strength-to-weight ratio, is easy to procure, inexpensive, and has a proven environmental resistance.

A standard computer numerical control (CNC) machine was used to perform the machining. Note that a high level of hole and slot location precision can be guaranteed as long as the precision features are all located on the same side of the part to be machined. The baseplate precision features were measured by a coordinate measurement machine to verify that the required tolerances were achieved. They were found to be within or better than the required tolerances.

3.4.1 Beam Combination Module (BCM)

The Beam Combination Module is housed in a fully kinematic mount. Figure 9 is a schematic diagram of the BCM optomechanical alignment scheme. The BCM rests on high-precision ruby balls lenses fixed on pads located at the bottom of the baseplate. These ball lenses provide contact points that define the height and tilt of the module with respect to the rest of the system. The diffractive optical elements located on the BCM are precisely diced and aligned with respect to dowel pins inserted into the baseplate to determine the lateral and angular position of the BCM module. This scheme guarantees a high degree of accuracy in the positioning of the BCM.

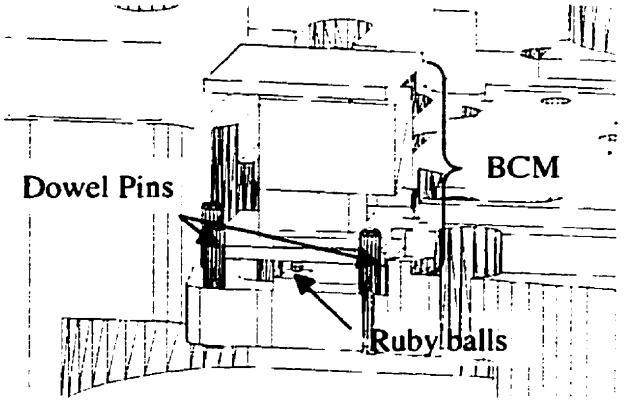

Figure 9. Diagram of BCM Kinematic Mount.

3.4.2 Relay Module, Risley Prisms and Corner Prism

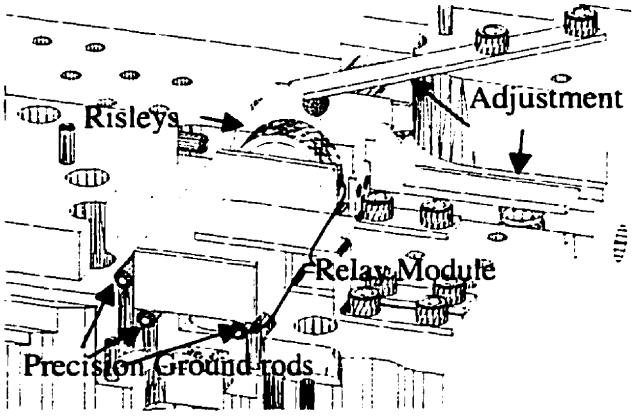

Figure 10. Diagram of Relay Module 5 DOF Mount.

The Relay Module is positioned in a semi-kinematic mount (the longitudinal position is not constrained). Figure 10 is a schematic diagram of the Relay Module alignment scheme. The microlens arrays located at each end of the block of glass rest on high accuracy rods placed at the bottom of the slots machined in the baseplate and thus define the alignment of the module. Finely threaded screws are used to vary the position of the

Corner Prism laterally (thus displacing the beams laterally with respect to the nominal optical axis). The Risley prisms are mounted in cells held in place by magnets. This mounting mechanism allows rotation of the Risley prisms to compensate for possible misalignments of the beams in the interconnect.

3.4.3 OE-VLSI Chip Module

Figure 11 is a schematic diagram of the Chip Module optomechanical alignment scheme. The lateral position of the Chip Module is defined by two precision dowel pins inserted in the baseplate. This method insures an alignment precision of ±20μm laterally. The tilt and longitudinal position are determined by the contact between the BCM Jointing Plate and the Chip Module minilens array. This contact is maintained by springs applying a constant retaining force on the package.

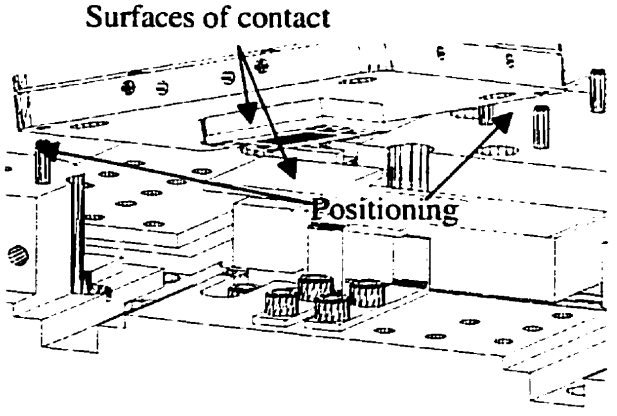

Figure 11. Diagram of Chip Module Mount.

3.4.4 Optical Power Supply (OPS)

The OPS components are mounted on precision ground rods which define the OPS optical axis (as shown in figure 4). Those rods are inserted in the baseplate to define the position of the OPS with respect to the other modules. This type of interface results

in easy interchangeability between modules. Measurements demonstrating the excellent insertion repeatability of this module can be found in [2].

3.5 Alignment Procedure

One the modules are constructed, they must be inserted in the baseplate in order to construct the backplane. The alignment steps for one stage (two Beam Combination Modules and one Relay Module) are outlined below:

1) Place and align the first BCM within its kinematic mount. Place and screw in the brass clamp around the BCM to secure it in place.
2) Position the Corner Prism.
3) Position the Relay Module.
4) Place and align the second BCM within its kinematic mount. Place and screw in the brass clamp around the BCM to secure it in place.
5) Verify Alignment at the detector plane. If alignment is not satisfactory, rotate the Risley prisms located before the Relay Module to bring the spots into alignment.

If the alignment is deemed satisfactory, the procedure is repeated for the next stage until the assembly of the ring is complete. Note that the alignment procedure given above assumes that the system can be passively aligned. Whether this is the case or not depends on the accuracy of the tolerances that were calculated in [8]. Chapters 4 to 6 will verify the accuracy of the calculation hypotheses and chapter 7 will confirm experimentally.

3.5.1 Risley Prisms and Tilt Plates

The interconnect contains a pair of Risley prisms that are located before the Relay Module. They are useful to adjust the tilt of the beams as they enter the Relay Module. Such a tilt adjustment will vary the angle of the beams on the Chip Module minilens thus changing their lateral position and allowing them to be brought on to the detectors. The Risleys consist of 2mm thick wedges possessing identical 25 minute angles (0.416°) and made of SF11 glass having an index of 1.762 at 852nm. Identical angles insures that the tilt introduced in the beams can be varied from 0 to a maximum angle of θ_d . The maximum deviation that can be obtained from a single Risley prism can be calculated using the following equation:

$$\theta_d = \sin^{-1}\left\{ n \sin\left\{ \theta_w + \frac{\sin\left(\sin^{-1}\left[(n\sin\theta_w) - \theta_w\right]\right)}{n} \right\} \right\} - \theta_w \qquad \text{Eq. (1)}$$

Where θ_w is the wedge angle and n is the refractive index. If the wedge angle is small, the above equation can be approximated as:

$$\theta_d = 2(n-1)\theta_w \qquad \text{Eq. (2)}$$

For a 25 minute wedge angle, the maximum deviation is calculated to be 0.633°. This corresponds to a lateral displacement of 94μm at the detector plane.

The Optical Power Supply Module houses a pair of Risley prisms as well as a pair of tilt plates. The tilt plates are 3mm thick plane parallel plates of glass (BK7) having an index of 1.48 at 852nm that are positioned at an angle (20°) relative to the optical beams. They

are useful to effect a lateral alignment of the beams on the Chip Module minilenses so as to eliminate clipping. The maximum lateral displacement produced by a pair of tilt plates can be calculated with the help of the following equation:

$$\Delta = \frac{2d}{\cos\left(\sin^{-1}\left(\frac{\sin(\theta)}{n}\right)\right)}\sin\left(\theta - \sin^{-1}\left(\frac{\sin(\theta)}{n}\right)\right) \qquad \text{Eq. (3)}$$

Where d is the thickness of the tilt plate, θ is the angle at which the tilt plate is positioned and n is the refractive index. The maximum displacement that can be obtained is calculated to be equal to 712μm. However, this is not the maximum lateral displacement that can be obtained on the Chip Module minilenses due to the demagnification produced by the OPS Fourier lens-minilens combination which act as a telescope whose magnification is the ratio of the focal lengths (8.5mm/30mm=0.2833). The maximum lateral displacement obtained on the Chip Module minilenses is therefore equal to 201.7μm.

3.6 Scalability Analysis

It is interesting to investigate what limits there are to the scalability of the system. Assuming that the optical design is not modified, then the system is scalable in the sense that:

1) The number of nodes in the system (OE-VLSI Chips) can be increased.
2) The number of clusters can be increased thus increasing the number of channels and the bandwidth between the nodes.

3.6.1 Increasing the Number of Nodes in the System

Increasing the number of nodes (the switching fabric size) in a system allows more data to be switched and routed. Reference [3] provides some considerations as to the scability of the Hyperplane architecture. The fabric size (the number of nodes that can be implemented), the channel width (the number of bits in a channel) and the number of smart pixels present on the chip are all related. More precisely, the number of smart pixels is equal to the fabric size times the channel width. The present implementation contains 16x16 smart pixels and a channel width of 8 bits. The maximum fabric size attainable with the present implementation is thus equal to 32. The size of the optoelectronic chip would have to be increased to house more smart pixels in order to achieve larger fabric sizes.

The backplane is presently implemented as a four node system arranged in a ring configuration. Figure 12 presents a flattened layout of the four node system.

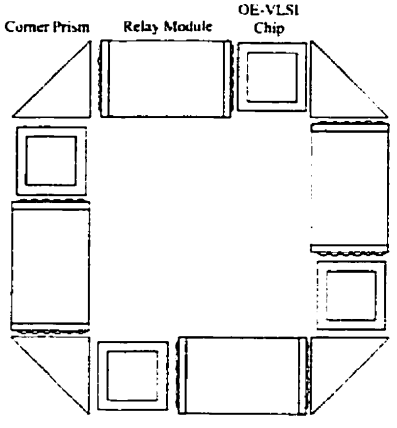

Figure 12. Flattened Four Node System in a Ring Configuration

The number of nodes can theoretically be increased (up to 32) by turning a Corner Prism and repeating the pattern in a serpentine fashion as shown in figure 13 illustrating an eight node system.

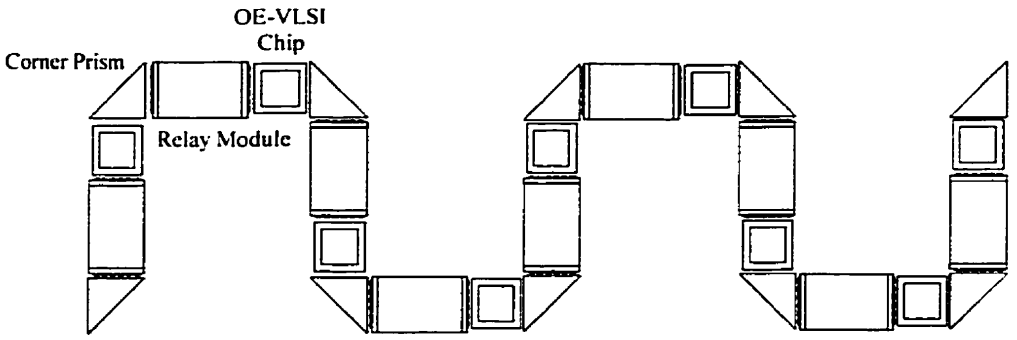

Figure 13. Eight Node System in a Linear Congifuration

Note that the eight nodes are arranged in a linear fashion. The last OE-VLSI chip in the chain is not optically linked to the first. This constitutes a problem for the present interconnect design since it is presently designed in a unidirectional ring configuration. The optical design of the interconnect would have to be modified to make it bidirectional in order to allow to scale the system in a linear fashion. This would seriously complicate the optical design. Another potential solution would be to retain a ring configuration but to implement the system as a closed polygon. The number of nodes would then be bounded by the area that the optical layer could occupy.

3.6.2 Increasing the Number of Clusters

Increasing the number of clusters increases the number of optical channels linking each node thus increasing the bandwidth between each node and the processing capacity of the system. However, assuming that the optical design of the interconnect remains the same, the number of clusters is constrained by a number of factors. While there is no minimum, a maximum exists due to the fact that if the focal length remains constant then

the space to fit more optical beams is simply not available. Figure 14 illustrates the geometry of a beam combination module.

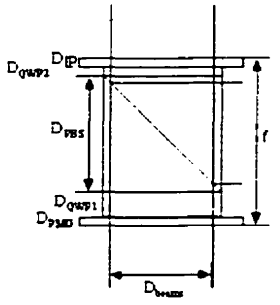

Figure 14. Layout of a Beam Combination Module.

A total distance of one focal length (f) separates the PMG from the IP plane. This a design constraint as one focal length must separate the Fourier plane array generator (the PMG) from the minilens attached to the Interface Plate (IP) in order for the system to remain telecentric. The focal length (f = 8.5mm) is assumed to be fixed. Note that increasing the focal length will not be beneficial as it will also increase the minilens dimensions and thus decrease the interconnection density. It can be seen from figure 14 that increasing the diameter of the input matrix of optical beams (D_{beams}) also increases the size of the PBS (D_{PBS}) by the same proportion. However, the size of the PBS has to remain smaller than one focal length. Ideally, having $D_{beams} = D_{PBS}$ would ensure that the area of the optical components is fully used and no space is lost. In equation form;

$$f = \frac{D_{PMG}}{n_{PMG}} + \frac{D_{QWP1}}{n_{QWP}} + \frac{D_{PBS}}{n_{PBS}} + \frac{D_{QWP2}}{n_{QWP}} + \frac{D_{JP}}{n_{JP}} \qquad \text{Eq. (4)}$$

Where f is the focal length. D_x represents the length of the components and n_x is the index of refraction of each component. Note that in practice, $D_{beams} < D_{PBS}$ guarantees that some margin is left for possible misalignments.

Equation four can be used to calculate the maximum D_{beams} that can be used assuming that the focal length is fixed and equal to 8.5mm.

We assume that the components have to be at least 1mm thick in order to insure mechanical robustness and that the index of refraction of the glass used can vary from 1.48 (BK7) to 1.76 (SF56A). If we want to maximize D_{beams} , then this means that we have to maximize n_{PBS} and minimize all the other terms. We are left with:

$$8.5 = \frac{1}{n_{PMG}} + \frac{1}{n_{QWP}} + \frac{D_{PBS}}{1.76} + \frac{1}{n_{QWP}} + \frac{1}{n_{JP}} \qquad \text{Eq. (5)}$$

If we choose the indices of refraction to be equal to 1.76, we are left with:

$$8.5 = \frac{4 + D_{PBS}}{1.76} \qquad \text{Eq. (6)}$$

Solving gives $D_{PBS} = D_{beams} = 10.96$mm.

The clusters are centered on a 800x800μm grid. This means that an 8x8 array occupies a 6.4x6.4mm square area. How many clusters can be fitted inside a 10.96mm square area? Calculations indicate that a 13x13 array occupies a 10.4x10.4mm area. A 13x13 array of 4x4 clusters will provide 2704 optical beams to the optoelectronic chips, more than

doubling the number of channels compared with the present implementation. This represents the absolute maximum achievable using this optical interconnect design.

Note that scaling to a 13x13 array might be challenging as the minimum feature size (the width of the minimum feature that can be etched) of the diffractive fanout grating will decrease from 2μm to 0.5μm. Half a micron is approximately the minimum feature size that can be commercially fabricated binary diffractive optics technology.

3.6.3 Image Mapping

Finally, some consideration of the image mapping properties of the optical system must be presented. The matrix of optical beams suffers a number of inversions when propagating through the optical interconnect. The inversions occur at two levels:

1) A « Macro-Level » inversion occurs at the 4x8 matrix level due to reflections off the reflecting surface of the PBS and Corner Prisms.
2) A "Micro-Level" inversion occurs at the 4x4 matrix level due to the two-dimensional imaging performed by the minilenses.

It is important to understand how the inversions occur in order to appropriately map the optical channels from one plane to the other. The functional description of image mapping is a particularly critical information for the chip designer. A matrix representation that allows calculating the mapping "function" through an optical interconnect has been developed by Liu et al. (see [5]).

The effect of the three "macro" reflections and the six "micro" imaging operations is shown in figure 15. The black triangle illustrates how the 4x8 matrix is inverted as it travels from one stage to the next while the "J" illustrates how each 4x4 cluster is inverted. The system is represented looking towards the baseplate (i.e. in the direction of the OPS).

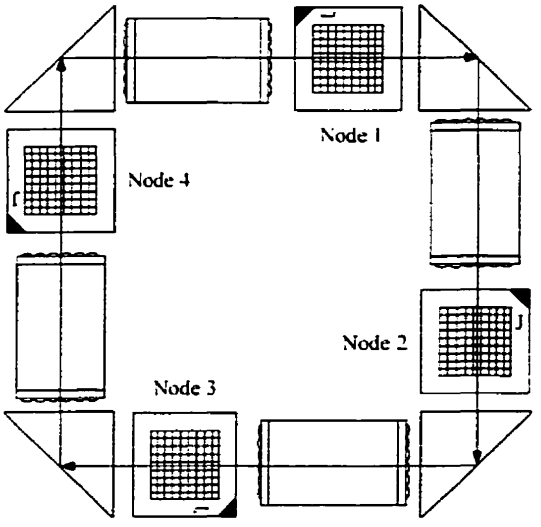

Figure 15. Schematic Diagram Illustrating the Image Mapping through the Backplane

Figure 15 shows that the effects of "Macro" and "Micro" inversions can be functionally described as:

1) A mirroring at the "Macro" level as shown in figure 16.

3) A mirroring and rotation at the "Micro" level as shown in figure 17.

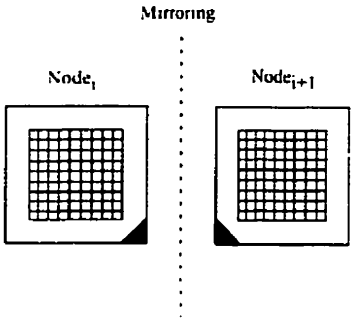

Figure 16. Mirroring of 4x8 Array upon Propagating from Node$_i$ to Node$_{i+1}$.

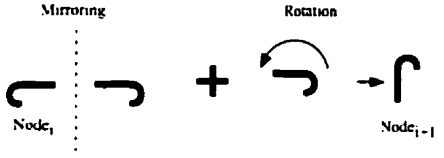

Figure 17. Mirroring and Rotation of 4x4 Cluster upon Propagating from Node$_i$ to Node$_{i+1}$.

These image mapping properties will be experimentally verified in chapter 7 (implementation).

3.7 Summary

The design of the optics and optomechanics for a dense, misalignment tolerant, four-node photonic backplane implemented as a uni-directional ring has been presented. The goals pursued with this project are two-fold: 1) Demonstrate a series of desirable optomechanical properties and 2) Test design assumptions.

The clustered interconnect design achieves both a high window density and a moderate window size. Grouping the components into modules relaxes the system tolerances and

shifts the critical alignment steps away from the system assembly phase. Kinematic and semi-kinematic alignment mounts have been designed to house the modules. Finally, a scalability analysis has shown that the interconnect design can support a maximum of 2704 optical beams.

3.8 References

[1] B. Robertson, "Design of an Optical Interconnect for Photonic Backplane Applications", *Applied Optics*, Vol. 37, No. 14, 10 May 1998.

[2] E. Bernier, F. Lacroix, M. H. Ayliffe, F. A. P. Tooley, D. V. Plant and A. G. Kirk, "Implementation of a compact, four-stage, scalable optical interconnect", Proceedings of *Optics in Computing* 2000, R. A. Lessard, T. Galstian editors, SPIE Vol. 4089 (2000) 0277-786X.

[3] T.H. Szymanski and H.S. Hinton, "Reconfigurable intelligent optical backplane for parallel computing and communications", *Applied Optics*, Vol. 35, No. 8, pp 1253-1268, March 1996.

[4] F.A.P. Tooley, "Challenges in Optically Interconnecting Electronics", *IEEE Journal of Selected Topics in Quantum Electronics*, Vol. 2, No 1, April 1996.

[5] A. V. Krishnamoorty and K. W. Goossen, "Progress in optoelectronic-VLSI smart pixel technology based on GaAs/AlGaAs MQW modulators", *International Journal of Optoelectronics*. 1997, Vol. 11, No. 3, 181-198.

[6] D.R. Rolston et al., "A Hybrid-SEED Smart Pixel Array for a Four-Stage Intelligent Optical Backplane Demonstrator", *IEEE Journal of Selected Topics in Quantum Electronics*, Vol. 2, No. 1, April 1996.

[7] Daniel F.-Brosseau, Frederic Lacroix, Michael H. Ayliffe, Eric Bernier, Brian Robertson, Frank A. P. Tooley, David V. Plant, and Andrew G. Kirk, "Design, Implementation, and Characterization of a Kinematically Aligned, Cascaded Spot- Array Generator for a Modulator-Based Free-Space Optical Interconnect", *Applied Optics*, Vol. 39, No. 5, 10 February 2000.

[8] F. Lacroix, "Analysis and Implementation of a clustered, scalable and misalignment tolerant optical interconnect", Master's Thesis, McGill University, 1998.

Chapter 4: Accuracy of Simulation Methods

4.1 Introduction

The first hypothesis used in the design of the optical interconnect presented in chapter 3 is that a Gaussian beam propagation model provides an accurate estimate of misalignment tolerances. However, Gaussian beam propagation theory cannot model aberrations introduced by the optical components or diffraction due to clipping of the beam as it propagates. Furthermore, its accuracy when calculating misalignment tolerances has never, to the authors' knowledge, been verified. This chapter will provide an analysis of the precision of various numerical models such as Gaussian beam propagation, ray tracing and scalar wave diffraction theory for tolerancing free-space optical interconnects.

Figure 1 illustrates the typical physical implementation of a board-to-board optical interconnect. It is a telecentric system which guides a beam emitted from a source located on a printed circuit board (PCB) to a detector located on another PCB. Such systems can be said to be "microchannel-based" because the energy and information transmitted in each beam is contained within the microchannel defined by the apertures of the relay microlenses.

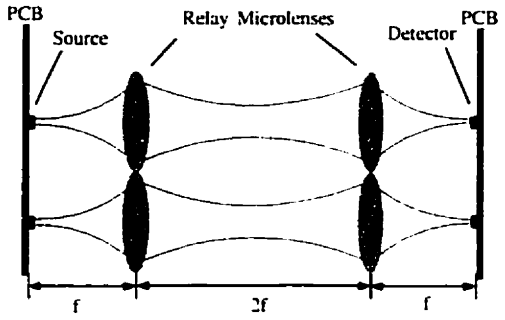

Figure 1. Typical implementation of board-to-board free-space optical interconnect.

The source typically consists of a vertical-cavity-surface-emitting-laser (VCSEL) or an electro-absorption modulator device (in which case an external readout beam is needed). The transverse intensity profile of beams emitted by single mode optical fibers or single mode VCSELs closely approximates a Gaussian function; Gaussian beam propagation theory is therefore a logical choice to model the propagation of such beams in an optical interconnect [1]. Typically, large two-dimensional arrays of devices are interconnected with the help of arrays of microlenses possessing circular or square apertures to achieve a high interconnection density.

Misalignment of the components modifies the direction of propagation as well as the waist size and position of the Gaussian beams guided by the microlenses. Lateral misalignments of the relay microlenses, for example, can deviate the beams angularly and cause lateral decentrations of the focused spot at the detector plane. Longitudinal misalignments shift the longitudinal position of the waist and modify its radius, which results in a defocus at the detector plane. Decentrations or magnifications at various planes in the system may cause part of the energy contained within the microchannel to

be clipped by the edge of the microlenses and to couple into adjacent channels. This decreases the amount of optical power reaching the detector which can limit the system operating rate [2]. It can also lead to possible crosstalk between channels as the clipped energy is susceptible to be directed to the wrong detector [3]. Recent work concerning the calculation of misalignment tolerances in free-space systems is described in references [4] and [5].

In addition to causing power losses and possible crosstalk, clipping at an aperture causes modifications in the transverse intensity profile of the diffracted beam. The magnitude of these modifications and the ability of Gaussian beam theory to model these diffracted beams depends largely on the amount of power that is subtracted by the aperture; a small power loss will only slightly modify the beam profile while a large power loss will cause substantial modifications in the intensity pattern. The effects of weak symmetrical clipping at a circular aperture have been investigated by a number of researchers: P. Belland and J. P. Crenn have shown that a weakly clipped Gaussian beam can still be approximated as a Gaussian after diffraction by a circular aperture but that the spot size, waist location and beam divergence substantially differ from that predicted by Gaussian beam theory for power losses as low as 1% [6]. K. Tanaka and O. Kanzaki have experimentally demonstrated that the waist of a clipped Gaussian beam is shifted longitudinally towards the aperture as the clipping increases [7]. Note that aberrations introduced in a beam by optical components also modify its transverse intensity pattern.

In the general case, however, the clipping of the beam is either asymmetrical due to the presence of square apertures and/or decentrations of the beam within a circularly symmetric aperture or the power loss is too severe and approximations such as Belland and Crenn's are not valid in those regimes. A rigorous wave propagation analysis based on diffraction theory would have to be employed but as this is often computationally prohibitive, less complex models such as ray tracing and Gaussian beam propagation are used instead.

This chapter compares the theoretical results provided by several optical beam propagation models (Gaussian beam propagation, ray tracing and scalar diffraction theory) with experimental data when tolerancing the components of a 4f telecentric, clustered free-space optical system which has square lens apertures.

4.2. Numerical Models used in Tolerance Calculations

A variety of numerical models can be used to simulate optical power propagation in an optical system. These include:

1) Gaussian beam propagation.
2) Ray tracing.
3) Wave propagation using the Fresnel-Kirchhoff scalar diffraction theory. Note that "wave propagation" and "scalar diffraction theory" are used interchangeably.

This section briefly introduces each model and their use in tolerancing optical systems.

4.2.1 Gaussian Beam Theory

Gaussian beam theory approximates the behavior of beams that are output from semiconductor lasers or single-mode optical fibers. While the diffraction spreading of the beam with propagation is included in the theory, diffraction from apertures and aberrations introduced in a beam by optical components are not modeled. Formulas describing the characteristics of Gaussian beams and their interaction with optical components are given in [1]. Following are formulas useful in misalignment tolerance calculations.

The intensity of the beam as a function of radial distance is given by:

$$I(\rho,z)=I_0\left[\frac{\omega_0}{\omega(z)}\right]^2\exp\left(-\frac{2\rho^2}{\omega^2(z)}\right) \qquad \text{Eq. (1)}$$

Where I_0 is the on-axis intensity, ω_0 is the waist radius and $\omega(z)$ is the beam radius at axial distance z (measured from the waist location). The power coupled into a rectangular aperture of width $(-a_1,a_2)$ in the x direction and $(-b_1,b_2)$ in the y direction can be calculated by numerically integrating the Gaussian beam intensity distribution on the aperture. A coordinate system change is necessary to convert the intensity from cylindrical to rectangular coordinates in order to account for the presence of square microlenses.

$$P=I_0\int_{-a_1-\Delta x}^{a_2-\Delta x}\int_{-b_1-\Delta y}^{b_2-\Delta y}\left[\frac{\omega_0}{\omega(z)}\right]^2\exp\left(-2\left(\frac{x^2+y^2}{\omega^2(z)}\right)\right)dxdy \qquad \text{Eq. (2)}$$

Where Δx and Δy are decentrations of the center of the Gaussian beam with respect to the center of the aperture. This integral can be separated in its x and y components and numerical integration carried out using error functions.

Tolerancing an optical interconnect system involves misaligning a component in a selected direction, propagating a beam using Gaussian beam formulas to calculate the beam size and position on various apertures in the system (minilens, detector) and calculating the amount of power that is coupled into each aperture using equation 2. The ratio of the power incident on the detector over the power that is launched from the source (known as throughput) versus misalignment of the component can be plotted and misalignment tolerance boundaries set using a metric that usually specifies the percentage of power falloff from the maximum (assumed to be obtained when a system is perfectly aligned) that is tolerable. This is termed a sensitivity analysis as it evaluates the sensitivity of throughout with respect to individual parameters. A 10% power falloff metric (commonly used in the litterature) is used to set the misalignment tolerance boundaries in this paper.

4.2.2 Ray Tracing using a Gaussian Apodization of the Source

Ray tracing simulates optical power propagation by sampling a wavefront with a number of rays that propagate normally to the wavefront at every point [8]. Although diffraction spreading due to clipping cannot be modeled, aberrations introduced by optical components are included in ray tracing calculations.

A Gaussian apodization of the source must be performed in order to simulate the propagation of a Gaussian beam. This is simply a weighting of the rays launched at the source according to a Gaussian intensity pattern. It is done by controlling the angle of the launched rays to match a Gaussian intensity profile at some predefined plane in the system (normally the entrance pupil). During this study, it was found that simply approximating the input Gaussian beam as a point source and apodizing the angle of the launched rays overestimated the longitudinal tolerances. This is thought to occur because the point source used to represent the Gaussian beam is imaged to a point on the detector rather than to a finite diameter spot thus allowing for a greater amount of defocus before power losses becomes noticeable. It is more accurate to use an extended source possessing a diameter set so as to contain 99% of the energy of the Gaussian beam and to apodize both the launch angle and position of the rays to simulate a Gaussian intensity profile. This was done using five thousand rays to sample the wavefront.

4.2.3 Wave Propagation based on the Fresnel-Kirchhoff Scalar Diffraction Theory

This formulation is based on the Huygens-Fresnel principle and treats a wavefront propagating in space as a result of the superposition of the secondary wavelets emitted by point sources located on a primary wavefront [9]. It includes both aberrations and clipping effects. The Huygens-Fresnel principle can be mathematically expressed by the following equation:

$$U(x_0, y_0) = \iint_{\Sigma} H(x_0, y_0; x_1, y_1)\, U(x_1, y_1)\, dx_1 dy_1 \qquad \text{Eq. (3)}$$

Where $U(x_1,y_1)$ is the primary wavefront, H is a weighting function that approximates each point on the primary wavefront as a point source of spherical waves and Σ is the

aperture. The wavefront diffracted by an aperture such as a microlens is calculated by numerically integrating the field present in the surface of the aperture as specified in equation 3. The surface of the aperture is divided in a series of square pixels and the contribution of each pixel summed to obtain the diffracted field. The power transmitted by the microlens is calculated by weighting each pixel contained in the microlens aperture according to the intensity of the field present at that point of the aperture. A quadratic phase term is added to the field to account for the phase transforming properties of the microlens. In a system containing multiple apertures, the diffracted field must be calculated anew after each aperture. No approximations to equation 3 such as the Fresnel or Fraunhofer approximations were used for the calculations done in this work.

4.2.4 Summary

The strengths and weaknesses of each model presented in the previous sections are summarized in table 1. It shows that only the wave propagation model accurately models diffraction effects from apertures. However, the complexity of the calculation (even with the use of a Fresnel approximation in the diffraction integral) increases rapidly with the number of surfaces and sampling points, which makes its use impractical when tolerancing complex systems possessing a large number of surfaces or requiring many sampling points.

Table 1: Summary of properties of numerical models.

Model	Gaussian Beam	Diffraction from Apertures	Aberrations	Complexity
Gaussian Beam	Yes	No	No	M
Ray Tracing	Yes*	No	Yes	NxM
Wave Propagation	Yes	Yes	Yes	$MxNlog_2N$

A Gaussian apodization of the source has to be used.
M: Number of surfaces.
N: Number of sampling points (rays or field points for the FFT).

4.3 Experimental System

The system chosen as a case study is a subsection of the optical interconnect designed for board-to-board applications presented in chapter 3 [10]. It consists in a clustered, telecentric relay system having a total length of 12f between each optoelectronic device plane. "Clustering" refers to the grouping of multiple beams around the optical axis of each minilens (see fig 2). Such systems can be termed minichannel-based because an array of beams (as opposed to only one beam in microchannel systems) is transmitted through each minilens. This achieves high interconnection densities while maintaining large misalignment tolerances.

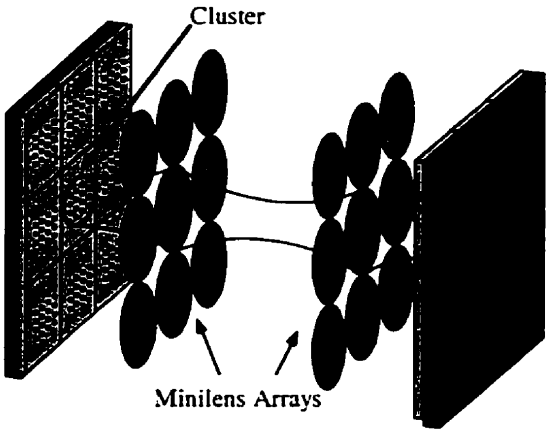

Figure 2. Diagram of clustering concept.

The potential impact of the misalignment of the minilenses can be appreciated by examining figure 3 which represents the 99% intensity footprint of the beam on the minilenses for a single 4x4 cluster array: any misalignment of the beam array with respect to the minilens will result in part of the energy contained in the beams being clipped. Notice that the 99% intensity diameter of a single beam does not fill the minilens aperture: a 4x4 array of beams is necessary to fill the surface of the minilens

(except for the corners). The beams in the 4x4 matrix are located on a 90μm square grid. The dots represent the center of the beams.

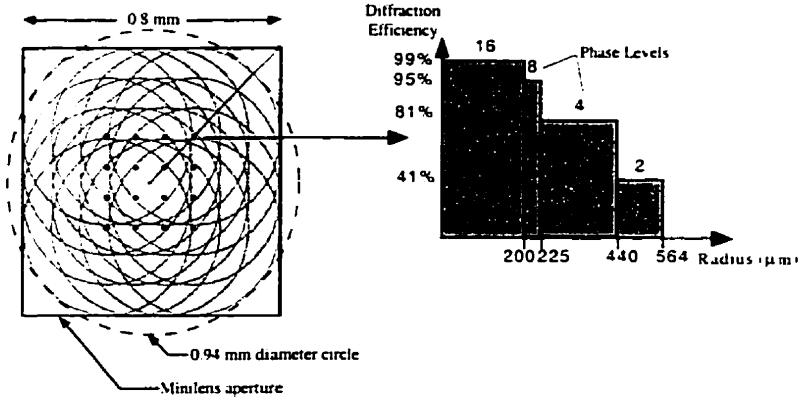

Figure 3. Beam footprint at minilenses (99% intensity) and diffraction efficiency profile.

Figure 3 also shows the variation in the number of phase levels and diffraction efficiency across the radius of the minilens. The diffractive minilenses possess a variable number of phase levels across their radius in order to maximize diffraction efficiency while maintaining a minimum feature size superior to 2 μm across their radius. The number of phase levels decreases progressively from sixteen phase levels in the center to only two phase levels in the corners.

The optical performance of the system was simulated on a commercial optical design software package and found to provide diffraction limited performance (the Strehl ratio was found to be equal to 0.99) across the field. Aberrations therefore do not modify the characteristics of the beams as they propagate through the optical system and can be ignored.

The experimental setup shown in figure 4 was constructed to measure lateral and longitudinal misalignment tolerances for the first minilens array. Measuring and modeling of angular tolerances was not done, as these are usually large for a microlens-based system (a ±2° microlens array tilt tolerance is quoted in [11]). The 4f system under study was mounted in the path of a Gaussian beam possessing a 13.1μm waist produced by a beam delivery system consisting of a delivery fiber, collimation lenses and a focusing lens. A 50 μm diameter pinhole simulated the detector aperture and the power through the pinhole was detected with a power meter. The power reading was done differentially, i.e. the impact of power fluctuations of the laser were minimized by dividing the output power (Power meter A) by a reference value (Power meter B).

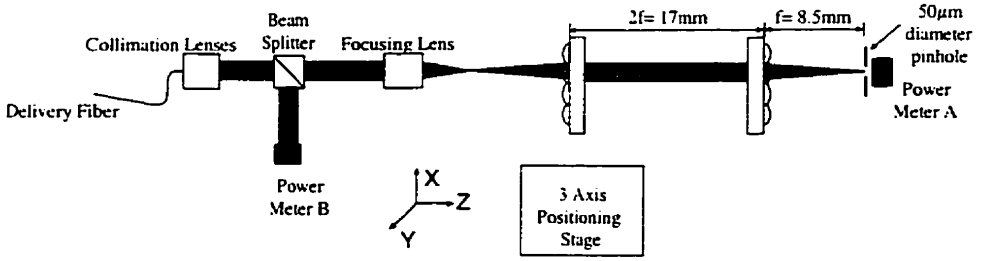

Figure 4. Diagram of the experimental setup.

The first minilens array was mounted on a computer controlled three axis positioning stage in order to misalign it in a controlled fashion. The second minilens array and pinhole representing the detector were mounted on three axis positioning stages. The correct longitudinal distances between each element (source-to-first minilens array, first minilens array-to-second minilens array and second minilens array-to-pinhole) were adjusted with the help of a precision caliper having a ±10 μm resolution. The angular alignment of the components was insured by measuring the longitudinal distance at several points of the components. It is estimated to be ±0.2°. The lateral alignment was

done by first visually centering the beam within the aperture of the minilenses with the help of a CCD camera equipped with a high magnification microscope objective and then optimizing the lateral position of the second minilens and pinhole in order to maximize the amount of power falling on the detector. From figure 7 and assuming that the power readings can be resolved to a precision of ±2% the absolute lateral alignment precision of the minilenses is then ±5 μm. Rotational alignment was insured by referencing the components with respect to the supporting optomechanics (the precision is estimated to be better than ±1°). The first minilens array was misaligned with respect to the rest of the 4f system in steps of 5μm laterally and 50μm or 100μm longitudinally in both positive and negative directions. The directions of the misalignments are provided by the coordinate system provided on figure 4. Note that the resolution of the positioning stage was 0.1 μm and the wavelength of the light was 852nm ± 0.1nm.

4.4. Experimental and Numerical Results

Measurements and simulations for a beam propagating on-axis and a beam propagating at the outermost corner in the array were performed in order to verify the effects of clipping on representative portions of the 4x4 array of beams. Because it is the first minilens array that is misaligned, the total power loss is distributed between the first and the second minilens.

The minilenses were modeled as thin, square lenses possessing a variable transmission coefficient across their radius. A continuous phase profile was assumed in the wave propagation analysis. Modeling true diffractive multilevel lenses would require using a prohibitively high sampling density to prevent aliasing errors due to the high spatial

frequencies present on the diffractive surface of the minilens. Note that the continuous phase profile provided accurate results for on-axis beams but failed to do so in the off-axis case. The symmetry present in the on-axis case probably insures fast convergence even when using a relatively low sampling density.

Many sources contribute to the experimental error when performing a measurement such as the one that is proposed here: the alignment accuracy in the various degrees of freedom of the components composing the 4f system, the precision of the longitudinal location and radius of the input beam waist with respect to the first minilens array, the alignment of the motorized positioning stage with respect to the 4f system, among others. Because of the large tolerances involved, it can be assumed that longitudinal and angular misalignments of the components do not contribute to the experimental error. Since the minilens arrays could not be mutually centered to better than ±5 μm, it was necessary to perform a curve fitting operation on the experimental lateral misalignment throughput curve with respect to the wave propagation results. This operation was not necessary in the longitudinal misalignment case as the placement accuracy of the components is two orders of magnitude smaller than available tolerances. The experimental error is estimated to be ±2 μm on the lateral position of the throughput curve in the lateral misalignment case (after curve fitting) and ±30 μm in the longitudinal misalignment case. The repeatability of the measurements was verified and measured powers were found to vary by less than ±5% between different series of measurements (the system was completely realigned each time).

4.4.1 On-Axis Beam

The first minilens array was misaligned in the lateral and longitudinal directions. Figure 5 is a plot of experimentally measured power versus lateral misalignment of the first minilens array in the XY plane. It can be observed on figure 5 that the experimental results are symmetrical in the X and Y axes and that the throughput falls off rapidly as the amount of lateral misalignment increases. Tilts introduced in the beam as the first minilens array is laterally misaligned result in a lateral decentration of the spot on the detector and this contributes to rapid throughput falloff. It can be shown that for a telecentric system the decentration of the spot on the detector is equal to the misalignment of the first minilens.

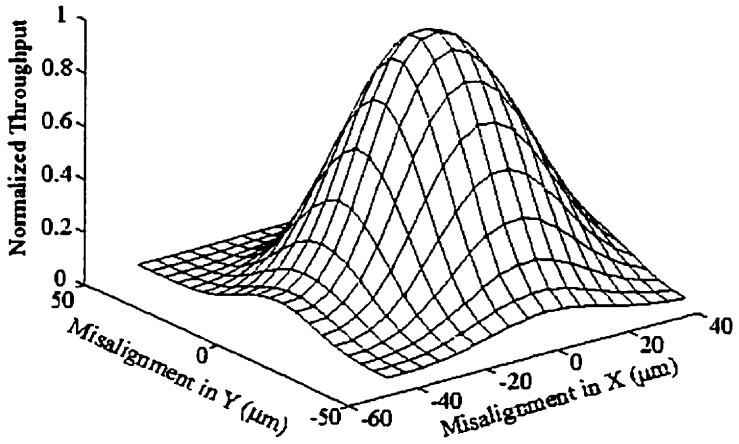

Figure 5. On-axis experimental data: Throughput versus lateral (XY) misalignment of the first minilens.

Figure 6 compares the experimental data with numerical calculations: it superposes the misalignment tolerance curves calculated with the help of the three models outlined in section 2 on a crosssection of figure 5 taken at the Y = 0 plane. The tolerance boundaries corresponding to a 10% power falloff metric are indicated on the graph.

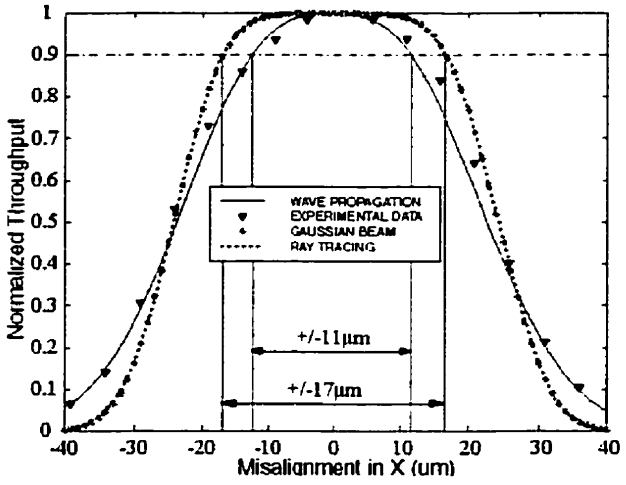

Figure 6. On-axis experimental and numerical data: Throughput versus lateral (X) misalignment of first minilens.

The throughput is slightly under 50% for a 25μm lateral misalignment of the first minilens. This is to be expected as roughly half of the power of the beam is outside the 50 μm circular aperture because of the 25 μm lateral decentration. Most of the power loss can be ascribed to vignetting effects in this case. It can be seen that the wave propagation model results closely match the experimental results. Although ray tracing and Gaussian beam propagation match each other perfectly (this validates the use of a Gaussian apodized extended source to model a Gaussian beam), they are in significant disagreement with the experimental results for the falloff metric selected. The difference is equal to 6 μm or an error of about 55% between ray tracing / Gaussian beam propagation theories and experimental results. This is probably attributable to the

inability of the ray tracing and Gaussian beam theories to model the diffraction spreading effects caused by intensity clipping of the beam as it encounters regions of the minilens possessing different diffraction efficiencies. Only the wave propagation model provides accurate modeling of the clipping effects in this case.

Figure 7 shows a plot of experimentally measured power throughput versus lateral and longitudinal misalignment along the X and Z axes for the first minilens array. The throughput falls off much more rapidly for lateral (X) misalignments than for longitudinal (Z) misalignments. This is not surprising considering that the beam remains centered on the detector as the first minilens array is longitudinally misaligned.

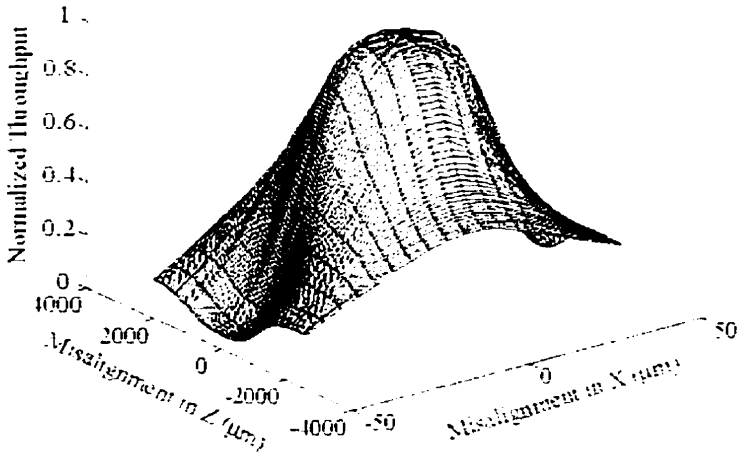

Figure 7. On-axis experimental data: Throughput versus lateral (XZ) misalignment of first minilens.

Figure 8 compares the experimental data with numerical calculations: it superposes the theoretical misalignment tolerance curves on a cross-section of figure 8 taken at the X = 0 plane. Belland and Crenn's approximation was not used because it is not applicable to square apertures.

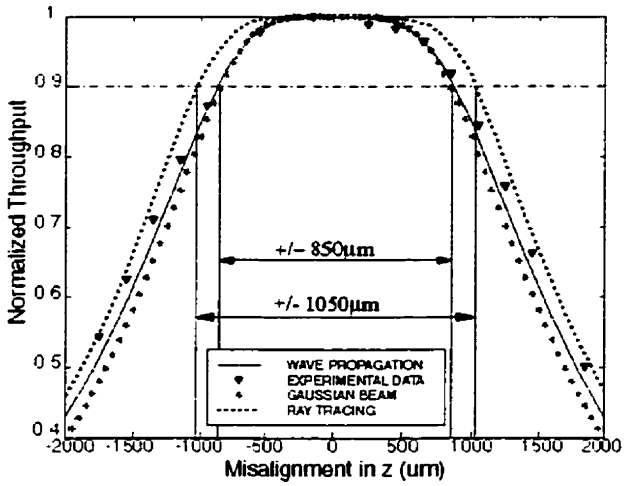

Figure 8. On-axis experimental and numerical data: Throughput versus longitudinal (Z) misalignment of first minilens.

Figure 8 shows that Gaussian beam theory provides results that are effectively as accurate as wave propagation. On the other hand, ray tracing overestimates the available longitudinal tolerances by roughly 200 µm or 24%. Diffraction effects through clipping seem to contribute less to power losses than does defocus of the spot on the detector. This might be because the beam diameter on the second minilens increases less rapidly than the focused spot size on the detector.

4.4.2 Off-Axis Beam

An off-axis beam placed at the cornermost position in the beam array as shown in figure 4 was used. Figure 9 is a plot of experimentally measured power versus lateral misalignment of the first minilens array. As shown in figure 10, the experimental results for lateral misalignment of an off-axis beam seem quite similar to the results for an on-axis beam presented in figure 6.

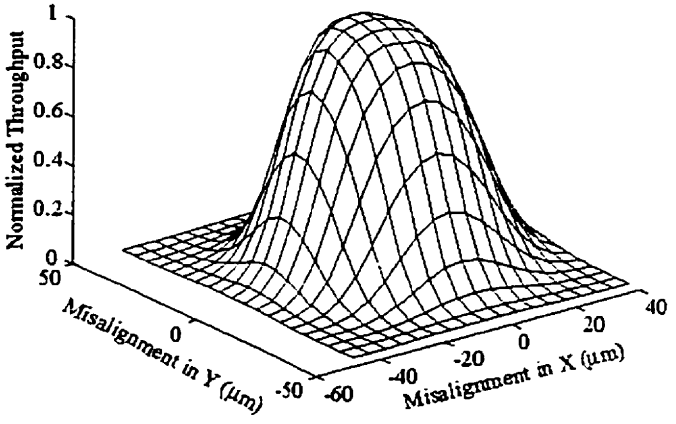

Figure 9. Off-axis experimental data: Throughput versus lateral (XY) misalignment of first minilens.

Figure 10 presents the experimentally measured and theoretically calculated misalignment tolerance curves for an off-axis beam when the first microlens is laterally misaligned (X). The wave propagation results are not presented as the continuous phase profile model of the lens does not provide meaningful results in the off-axis case.

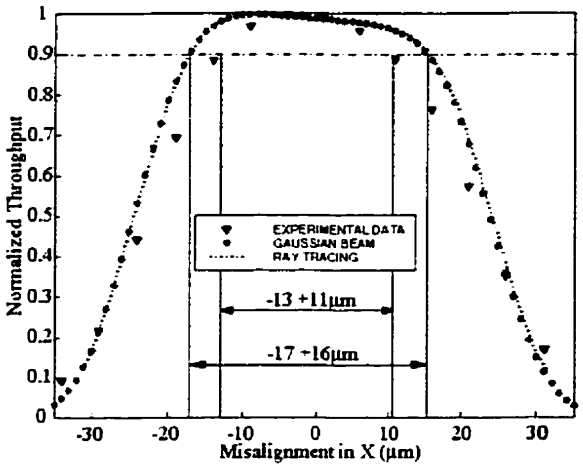

Figure 10. Off-axis experimental and numerical data: Throughput versus lateral (X) misalignment of first minilens.

The experimental throughput curves differ for the off-axis and on-axis cases (see fig. 7): there is a slight asymmetry present in the off-axis case as attested by the misalignment tolerances. The results provided by ray tracing and Gaussian beam propagation are also asymmetrical: the maximum of both curves is located at X = -10 μm. A lateral misalignment actually slightly increases the power falling on the detector. This may be due to a reduced power loss at the second microlens due to a decentration of the beam towards the higher efficiency central region of the second minilens. The accuracy of Gaussian beam and ray tracing is better in the off-axis case compared to the on-axis case. The difference between experimental and numerical results is equal to 30% and 45% for misalignments in the negative and positive X directions respectively.

Figure 11 is a plot of experimentally measured throughput curves versus lateral (X) and longitudinal (Z) misalignment of the first minilens array. Notice the asymmetry in the lateral direction of figure 12.

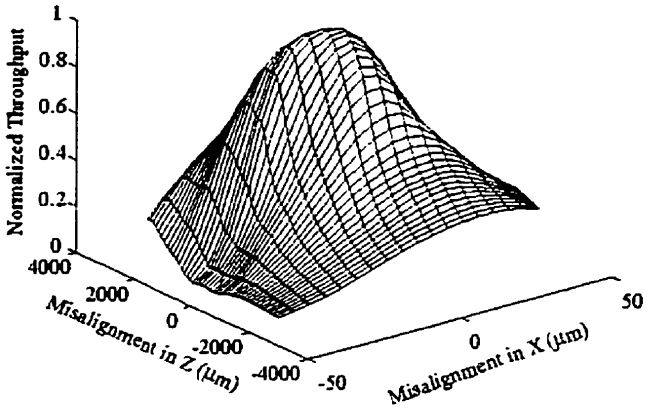

Figure 11. Off-axis experimental data: Throughput versus lateral (X) and longitudinal (Z) misalignment of first minilens.

Figure 12 compares experimental and numerical results for off-axis longitudinal misalignment. One can see that the experimental and numerical results differ widely in the longitudinal off-axis (fig. 12) and on-axis case (fig. 8).

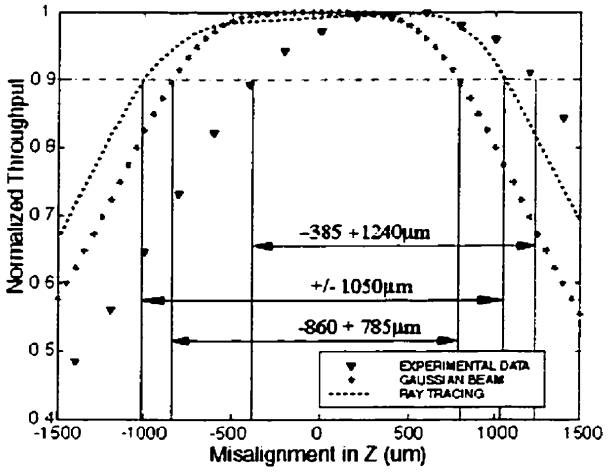

Figure 12. Off-axis experimental and numerical data: Throughput versus longitudinal (Z) misalignment of first minilens.

Figure 12 shows that a large focus shift of about 500μm is present in the experimental results that is not predicted by the numerical models used in this work although such a focal shift effect has been observed and modeled for single lens systems [12]. Notice the difference between the Gaussian beam and ray tracing results: Both models provide results that differ by as much as 265μm or 33%. Both fail to correctly model the real behavior of the system.

4.5. Summary

An analysis of the accuracy of various numerical models for calculating the misalignment tolerances of a free-space optical interconnect system was presented. The case study selected was a clustered, telecentric, 4f system relaying slow Gaussian beams (f/16) through multilevel diffractive minilenses. The system was diffraction limited. A summary of the 10% power falloff tolerances for a misalignment of the first lens in the lateral (X) and longitudinal (Z) directions calculated from experimental and numerical data (figures 6, 8, 10 and 12) is presented in table 2.

Table 2: Summary of tolerancing results.

Model	On-Axis Lateral (X)	On-Axis Longitudinal(Z)	Off-Axis Lateral (X)	Off-Axis Longitudinal (Z)
Gaussian Beam	±17μm	±850μm	+17/-16μm	+785/-860μm
Ray Tracing	±17μm	±1050μm	+17/-16μm	±1000μm
Wave Propagation	±11μm	±850μm	-	-
Experimental Data	±11μm	±850μm	+11/-13μm	+1240/385μm

As can be seen from table 2, wave propagation calculations using scalar diffraction theory show no significant difference for lateral and longitudinal misalignment tolerances compared to experimental results for on-axis beams. This is to be expected, as it is the

only model that implicitly includes diffraction from apertures in its calculations. The simulations for off-axis beams were not accurate and are not presented.

The use of a Gaussian beam or ray tracing model overestimates the available lateral (X) misalignment tolerance by 55% and 45% in the on and off-axis cases respectively. Throughput to the detector would be equal to 77% instead of 90% if the first minilens were laterally misaligned to the extent of the misalignment tolerance boundary indicated by the ray tracing and Gaussian beam propagation models. The first hypothesis used in the design of the interconnect is therefore not accurate. Use of a Gaussian beam model overestimates the available tolerances. This difference can represent a substantial amount of power and could limit the system operating speed. It is worth noting that this error is not constant over the entire misalignment range: it would be higher for more conservative falloff metrics (<10%) and falls to zero for throughputs around 40-50%.

Note that the power that is clipped from the beam propagating in the minilens cannot be assumed to simply exit the system: it will be incident on minilenses adjacent to the target minilens (or "target channel") and probably be guided to optoelectronic devices neighboring the target detector. In the case of a simple lateral misalignment, for example, the energy that is subtracted from the beam will be directed to the adjacent channel (i.e for a misalignment of 11 μm about 10% of the energy launched from the source will probably impact the nearest neighbor to the target detector). The situation is more complex for longitudinal misalignments as the energy truncated from the beam will be picked up by all the channels surrounding the target channel in various proportions.

As a first approximation, the truncated energy can be assumed to be equally divided between the four channels whose sides are contiguous to the target channel (i.e. for a 1000 μm misalignment, about 2.5% of the energy launched form the source will impact each device neighboring the target device). Thus inaccuracies in the modeling will also lead to signal to noise ratios (SNR) which are lower than expected.

Ray tracing and Gaussian beam propagation provide identical results when tolerancing lateral misalignment but show a disagreement when tolerancing longitudinal misalignment. Gaussian beam propagation theory accurately models defocus effects for an on-axis beam which seems to be the greatest source of power loss for a clustered system using oversized minilenses. Both models fail to show a large longitudinal focal shift (500μm) away from the second minilens array and past the nominal position of the detector present in the experimental results for the off-axis beam. The throughput versus misalignment curve provided by the ray tracing model is slightly asymmetrical and peaks around Z = +500μm. However, this is thought to be merely coincidental as the curve does not appear to be shifted longitudinally as would happen if a focal shift effect was taking place.

These results mean that a throughput calculated to be 90% for a misalignment of 1mm in the negative Z direction only actually result in 65% of the power going to the detector. Notice that the slope of the curves for the Gaussian beam and experimental results are relatively similar; if the experimental focal shift were subtracted from the Gaussian beam results, the two curves would provide similar tolerance bounds (to 7% accuracy). It is

interesting to point out that this focal shift effect is corroborated by the results of [7], [12] and [13] where it was shown that clipping by the aperture of a lens causes the waist of a Gaussian beam to be pulled in towards the lens. For a 4f system, this means that the output waist will be moved away from the second minilens if the input waist is moved towards the first minilens. This is demonstrated by the experimental results.

The limited fabrication accuracy of the optical or mechanical components implies that various random misalignments of the components will always be present when constructing a system. It is thus important to know how accurate commonly used optical power propagation models are at predicting power losses due to misalignments in order to set adequate component tolerances. The designer needs to be aware of the tradeoffs involved when using various numerical models: Gaussian beam analysis and ray tracing for example, although very accessible in terms of computational complexity, are liable to overestimate the available tolerances by as much as 50% laterally (X) and are not able to predict the significant longitudinal focal shift present in a clustered 4f system relaying slow Gaussian beams through multilevel diffractive minilenses. Note that if the focal shift were empirically or numerically modeled, then Gaussian beam propagation theory would provide accurate results (within experimental error) when tolerancing longitudinal misalignment tolerance in systems of this type. However, use of a wave propagation model is still necessary to calculate lateral tolerances to an accuracy greater than about 50%.

Future work on this topic should include looking at the impact of the system f-number on the accuracy of the various numerical models used to calculate tolerances. It has been previously demonstrated (see [13]) that when the incident wave is uniform and the angular semi-aperture is small the focal shift is inversely proportional to the Fresnel number N of the aperture (where N is the ratio of the square of the aperture linear dimension over the focal length times the wavelength of the light). Speculating from those results, it can therefore be thought that the numerical error will increase with decreasing f-number as the two quantities (f-number and Fresnel number) are inversely related.

4.6 References

[1] B. E. A. Saleh and M. C. Teich, *Fundamentals of Photonics*, John Wiley and Sons inc., Chpt. 3, 1991.

[2] T. K. Woodward, A. V. Krishnamoorty, A. L. Lentine, K. W. Goosen, J. A. Walker, J. E. Cunningham, W. Y. Jan, L. A. D'Asaro, L. M. F. Chirovsky, S. P. Hui, B. Tseng, D. Kossives, D. Dahringer, and R. E. Leibenguth "1-Gb/s Two-Beam Transimpedance Smart-Pixel Optical Receivers Made from Hybrid GaAs MQW Modulators Bonded to 0.8μm Silicon CMOS", *IEEE Photonics Technology Letters*, Vol. 8, No. 3, pp. 422-424, March 1996.

[3] A. McCarthy, F. A. P. Tooley, B. Robertson, J. Mike Miller, "Broken Symmetry Interconnects for Microchannel Relay Systems", *Proc. Optics in Computing (Snowmass, Colorado)* 1999.

[4] D. T. Neilson, "Tolerance of optical interconnections to misalignment". *Applied Optics*, Vol. 38, No.11, pp. 2282-2290, 10 April 1999.

[5] S. P. Levitan, T. P. Kurzweg, P. J. Marchand, M. A. Rempel, D. M. Chiarulli, J. A. Martinez, J. M. Bridgen, C. Fan, and F. B. McCormick, "Chatoyant: a computer-aided-design tool for free-space optoelectronic systems", *Applied Optics*, Vol. 37, No.26, pp. 6078-6092, 10 September 1998.

[6] P.Belland and J.P.Crenn, "Changes in the characteristics of a Gaussian beam weakly diffracted by a circular aperture". *Applied Optics*, Vol. 21, No.3, pp.522-527, Feb. 1 1982.

[7] K. Tanaka and O. Kanzaki, "Focus of a diffracted Gaussian beam through a finite aperture lens: experimental and numerical investigations", *Applied Optics*, Vol. 26, No. 2, pp. 390-395, 15 January 1987.

[8] R. R. Shannon, *The Art and Science of Optical Design*, Cambridge University Press, Chpt 2, 1997.

[9] J. W. Goodman, *Introduction to Fourier Optics*, McGraw-Hill, Chpts 3-4, 1968.

[10] B. Robertson, "Design of an optical interconnect for photonic backplane applications", *Applied Optics*, Vol. 37, No. 14, p.2974-2984, 10 May 1998.

[11] Y. Liu, B. Robertson, D. V. Plant, H. S. Hinton, and W. M. Robertson, "Design and characterization of a microchannel optical interconnect for optical backplanes". *Applied Optics*, Vol. 36, No. 14, pp. 3127-3141, 10 May 1997.

[12] S. De Nicola, D. Anderson, M. Lisak, "Focal shift effects in diffracted focused beams", *Pure and Applied Optics*, Vol. 7, IOP Publishing, pp. 1249-69, Sept. 1998..

[13] Li, Y.; wolf, E., "Focal shifts in diffracted converging spherical waves" *Optics Communications*, Vol.39, No.4, p.211-215, 15 Oct. 1981

Chapter 5: Tolerance Stackup Effects

5.1 Introduction

The second hypothesis used in the design of the optical interconnect presented in chapter 3 concerns tolerance stackup effects. The tolerances assigned to the components assume that tolerance stackup effects are not significant. This will be verified in this chapter.

The positioning and fabrication tolerances of optical components in free-space optical interconnects are commonly established with the help of a sensitivity analysis [1] sometimes followed by a worst-case analysis [2] or with a root-sum-square (RSS) analysis [3] to estimate the impact of tolerance stackup effects. Although these approaches are commonly used, their accuracy has, to the authors' knowledge, not been verified in the context of optical interconnects. Inadequate tolerances lead to poorly engineered systems that are either too costly or offer low performance. Time-consuming manual alignment must then be performed in the latter case.

There exist three main methods for calculating tolerance stackup; worst-case, statistical and sampled methods [4]. Each provides varying degrees of accuracy and implementation complexity. Use of a worst-case analysis is straightforward but generally results in over-engineered systems as it unrealistically assumes that every parameter is simultaneously defective to the limit of its tolerance range and to the worst possible effect (i.e. the one that leads to the most power loss). Statistical methods such as the root-sum-square (RSS) are more realistic as they take into account the low probability of a worst-

case scenario happening by assuming a Gaussian or normal distribution for the parameter tolerances. However, it assumes that all parameters are linearly independent. The sampled methods (such as Monte-Carlo) are the most accurate as the system is virtually and numerically "assembled" many times while each parameter is varied randomly according to its specified tolerance distribution. It is accurate for systems whose response is non-linear. However, many samples must be calculated to achieve a high accuracy.

This chapter seeks to verify the severity of stackup effects due to positioning errors in free-space optical interconnects with the help of a Monte-Carlo analysis. There are two goals to this exercise:

1) Provide answers as to whether worst-case or RSS analyses are adequate to estimate stackup effects.
2) Provide design guidelines to system designers by investigating how stackup evolves with:
    i) The severity of the loss criteria used to establish the component tolerances.
    ii) The number of tolerance parameters.
    iii) The f-number of the system.

Previous research [5] on the topic did not provide designers with generalized guidelines for system design.

In order to investigate the points stated above, two free-space optical systems possessing identical properties (telecentric relays, identical beam diameter/minilens diameter and beam diameter/detector diameter clipping ratios) but different f-numbers were selected for simulation purposes. The first system has an f-number of f/16 and can be considered to be a "slow" system while the second system has an f-number of f/3.38 and can be considered to be a "fast" system such as would result from using a singlemode optical fiber as the light source. Two systems possessing widely separated f-numbers were selected to investigate whether the "speed" of an optical system affects tolerance stackup.

5.2 Tolerancing Analysis

A sensitivity analysis followed by a Monte-Carlo analysis were performed to assign tolerances to the components of the optical systems and calculate the probable performance when assembling a system using components specified to those tolerances. This tolerancing procedure is commonly employed in the design of optical systems. The main difference with standard practices in this case stems from the fact that whilst the performance criteria for optical imaging systems normally consists in one of the image quality metrics such as the root-mean-square (RMS) wavefront error or the modulation transfer function (MTF) of the system, this is not appropriate for optical interconnects as throughput or the amount of power launched from the source that is incident on the detector and not image quality is the performance criteria of interest. In this case, tolerancing must be performed in order to determine the impact of various parameters on the throughput to the detector. The Monte-Carlo analysis is rarely performed when tolerancing optical interconnects due to its computation intensive nature.

A critical part of the sensitivity analysis consists in selecting a tolerance metric to delimit the tolerable variation range or misalignment tolerance for the parameter. This metric states how much power loss from the maximum (assumed to be located at the nominal parameter value) is tolerable. Let the reader be reminded that the misalignment tolerance as understood here is the misalignment of a single parameter of a single component (the rest of the system remaining perfectly aligned) that produces a decrease in power at the detector equal to the limit of the tolerance. A relaxed metric might render assembly easier and lower costs but might also provide lower performance in the assembled system due to accumulated losses. A more severe metric will mean that the tolerances are tighter, providing a lower loss but also increasing the fabrication cost. In order to highlight how errors accumulate with the severity of the loss criteria used to set tolerances, four tolerance sets were calculated with the help of four loss metrics: 10%, 1%, 0.1% and 0.01% power loss relative to the maximum.

The tolerance limits calculated for the parameters of each component were then used to delimit the statistical distributions to be used with each parameter in the Monte-Carlo analysis. In order to obtain accurate results, it is essential to assign the correct probability distribution to each parameter. The shape of these distributions is highly coupled to the manufacturing process used to fabricate the component. Little data is available from manufacturers regarding this topic. It was decided to use the same statistical distributions as are employed in a commercial optics simulation package [6]. The distributions associated with each parameter are the following: lateral and tilt misalignments are assumed to have a symmetrical Gaussian distribution with the one σ points (σ

representing of course, the standard deviation) located at the tolerance limits and longitudinal misalignments are assumed to have a symmetrical Gaussian distribution with the three σ points located at the tolerance limits given by the sensitivity analysis. Lateral and tilt misalignments thus have a much more uniform probability distribution compared to longitudinal misalignments.

Note that these distributions apply in the case of a system where every component is packaged individually.

5.2.1 Application Examples

Two free-space optical systems were selected for simulation purposes. The systems are scaled versions of one another. The focal length, minilens apertures and detector size are scaled to provide the same clipping ratio (the ratio of the beam diameter over the minilens or detector aperture) for both systems. The Gaussian beam waist radius of the source is adjusted to vary the f-number of the system. Note that the f-number is calculated to be equal to the focal length over the 3ω diameter of the Gaussian beam at the minilens aperture. Both systems use a telecentric relay to transmit the beams from a source to a detector. The length of the relay is varied from 4f, 8f to 12f in order to investigate the effect the number of parameters has on tolerance stackup. Oversized diffractive minilenses and detectors are used to minimize clipping at the minilens aperture.

The first design uses 8.5mm focal length, 800μm on the side square minilenses. The source is assumed to be placed on-axis at the focal point of the lens and to emit a

Gaussian beam possessing a waist radius of 13.1μm. The detector is assumed to be square and 70μm on the side. This design will be referred to as system one or the "slow" system. Note that this design is the same as presented in chapter 3.

The second system uses 3.0mm, 1341.5μm on the side square minilenses. The on-axis source is also placed at the focal point of the first minilens and emits a Gaussian beam possessing a 2.75μm waist radius. The detector is assumed to be square and 14.65μm on the side. This system will be referred to as system two or the "fast" system. Note that the Gaussian beam waist was chosen to correspond to the radius of the beam emitted from a singlemode fiber operating at 850nm (Thorlabs catalog number: 3M-FS-SN-4224).

The layout of the systems used for simulation purposes is illustrated in figure 1.

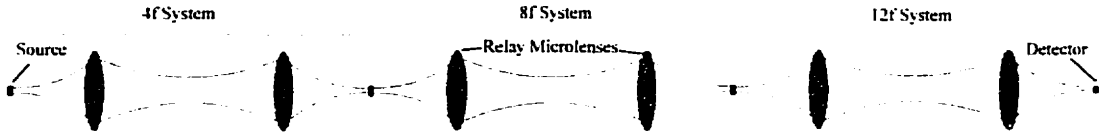

Figure 1. Schematic Layout of Application Examples.

The systems were found to provide diffraction limited performance. The Strehl ratio is equal to 0.99. Aberrations therefore do not modify the power distribution within the Gaussian beams as they propagate through the optical system and should not cause throughput variations. They can therefore be ignored in the simulation process.

Only the parameters related to the physical positioning of the components such as decentrations, tilts and defocus of the minilenses, the source and detector have been considered in the analysis. The tolerances associated with the source numerical aperture, wavelength, micro-optics substrate thickness and index of refraction, etc. have been ignored.

5.3 Results

5.3.1 Sensitivity Analysis

A sensitivity analysis was first performed on the two systems in order to calculate the tolerances on the parameters that will be used in the Monte-Carlo analysis. The sensitivity analysis was performed in the following fashion: the layout of the optical system was first entered on a commercial optics simulation package [6], one of the components in the system was misaligned and a Gaussian beam as well as a ray defining the center of the Gaussian beam were propagated through the system. The intercept coordinates of the ray as well as the waist radius at each surface of the system (minilenses and detector) were then written to a text file. This text file was used to calculate coupling at each interface with the help of a mathematical software package [7].

It is important to note that tilt tolerances for the minilenses and the detector were ignored in the present analysis. A minilens tilt around its center does not induce a deviation in the beam propagating in the interconnect and causes no decentration of the spot on the detector. Tilts of the minilenses should thus have a minimal impact on throughput. However, note that tilt tolerances were calculated for the source as tilting it causes a lateral misalignment of the beam on the minilenses (and thus clipping).

It was found during the course of the sensitivity analysis that the tolerances for each parameter did not vary significantly as the system length was increased from 4f to 8f to 12f. This is true for all the parameters except the source tilt. This is to be expected as the minilenses are oversized with respect to the Gaussian beam passing through them which means that most of the clipping and power loss occurs at the detector and not at the aperture of each component. Thus, the number of minilenses does not substantially affect the final throughput. The use of oversized minilenses thus considerably simplifies the present analysis. Note that the source tilt is the only parameter that decreases as the system length is increased from 4f to 8f to 12f. The source tilt tolerance is dependent on the number of minilenses as clipping at these minilens apertures is the only contributor to power loss (the focussed spot stay centered on the detector). There is roughly a 0.15° decrease in the absolute value of the tolerance for each 4f addition. However, the tilt tolerances for a 4f relay quoted in table 1 are used in the simulation process to simplify calculations.

The tolerances calculated with the sensitivity analysis for each system are presented in tables 1 and 2.

Table 1 presents the tolerances for the slow system. There are a total of 14, 20 or 26 tolerance parameters depending on the length of the system (4f, 8f or 12f). The tolerance parameters are composed of lateral decentrations (Δ_{Xs}, Δ_{Ys}) of the source, the minilenses

and the detector, longitudinal misalignments (Δ_{Zs}) of the source, the minilenses and the detector and tilts ($\Delta\Theta_{Xs}$ and $\Delta\Theta_{Ys}$) of the source.

Table 1. Tolerances for the Slow System.

	Metric			
Parameters	10%	1%	0.1%	0.01%
Δ_{Xs}	±27μm	±20μm	±15μm	±10μm
Δ_{Ys}	±27μm	±20μm	±15μm	±10μm
Δ_{Zs}	±800μm	±500μm	±350μm	±270μm
$\Delta\Theta_{Xs}$*	±1.7°	±1.15°	±0.75°	±0.375°
$\Delta\Theta_{Yx}$*	±1.7°	±1.15°	±0.75°	±0.375°
Δ_{Xm}	±27μm	±20μm	±15μm	±10μm
Δ_{Ym}	±27μm	±20μm	±15μm	±10μm
Δ_{Zm}	±800μm	±500μm	±350μm	±270μm
Δ_{Xd}	±27μm	±20μm	±15μm	±10μm
Δ_{Yd}	±27μm	±20μm	±15μm	±10μm
Δ_{Zd}	±800μm	±500μm	±350μm	±270μm

Note that the tolerances calculated in table 1 are quite large for a free-space optical interconnect: 10s of microns for lateral misalignments and 100s of microns for longitudinal misalignments.

Table 2 provides the tolerances for the fast system.

Table 2. Tolerances for the Fast System.

	Metric			
Parameters	10%	1%	0.1%	0.01%
Δ_{Xs}	±5.7μm	±4.25μm	±3.2μm	±2.25μm
Δ_{Ys}	±5.7μm	±4.25μm	±3.2μm	±2.25μm
Δ_{Zs}	±73μm	±46μm	±34μm	±23μm
$\Delta\Theta_{Xs}$*	±7.2°	±4.8°	±3°	±1.8°
$\Delta\Theta_{Yx}$*	±7.2°	±4.8°	±3°	±1.8°
Δ_{Xm}	±5.7μm	±4.25μm	±3.2μm	±2.25μm
Δ_{Ym}	±5.7μm	±4.25μm	±3.2μm	±2.25μm
Δ_{Zm}	±73μm	±46μm	±34μm	±23μm
Δ_{Xd}	±5.7μm	±4.25μm	±3.2μm	±2.25μm
Δ_{Yd}	±5.7μm	±4.25μm	±3.2μm	±2.25μm
Δ_{Zd}	±73μm	±46μm	±34μm	±23μm

A comparison of tables 1 and 2 provides some interesting insight into the variation of tolerances with the system f-number. Lateral and longitudinal tolerances are much more severe for the f/3.38 system than for the f/16 system. The contrary is true for the tilt tolerances as these are much larger for the f/3.38 than for the f/16 system. A tradeoff is thus present between the lateral, longitudinal and the tilt tolerances. Note that this tradeoff has already been pointed out by Neilson [8]. Also notice that the lateral tolerances of system 2 are scaled versions of the lateral tolerances of system 1. The scaling factor for the lateral tolerances (27/5.7=4.73) is identical to the scaling factor for the systems f-numbers (16/3.38=4.73).

5.3.2 Monte-Carlo Analysis

A Monte-Carlo analysis was performed to verify the effect of the simultaneous interaction of the tolerance parameters. The tolerance sets given in tables 1 and 2 were used to delimit the probability distributions for use in the Monte-Carlo analysis. Twenty five thousand or fifty thousand samples were calculated in each Monte-Carlo run.

Since the output Monte-Carlo distributions cannot be compared easily, ways have to be found to analyze and compare this data in a simple and satisfactory manner. One way of doing this consists in plotting normalized cumulative distributions. This renders the comparison process easier as the probable system performance or yield can be read off the chart directly.

5.3.2.1 Cumulative Histograms

5.3.2.1.1 4-f System

The distributions calculated by the Monte-Carlo simulations for the slow and fast systems are shown in figure 2 in the form of normalized cumulative distribution plots for each of the four tolerance sets. Note that the dashed curves represents data for the slow system while the solid curves represents data for the fast system.

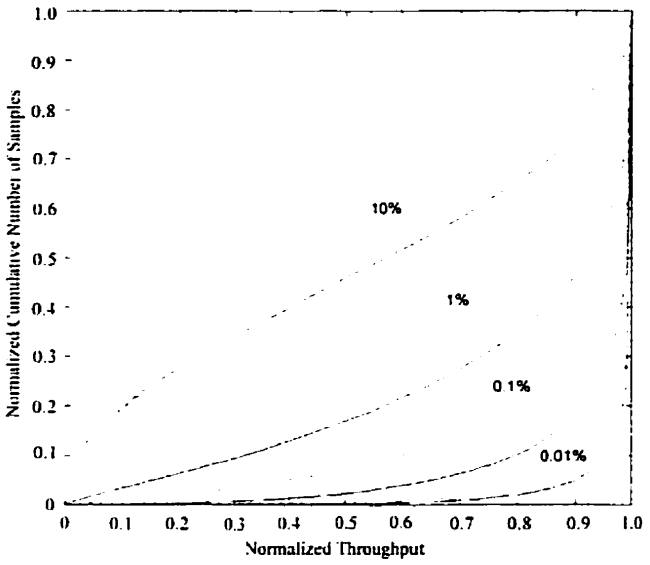

Figure 2. Plot of Cumulative Distribution versus Normalized Throughput for a Slow and Fast 4f System

It can be seen that the curves are paired for each tolerance set with the dashed curve always topmost. Since these are cumulative histograms, this means that more samples possess small throughput values for the slow system. The fast system suffers from slightly less severe stackup effects.

Reading numbers off the dashed curve, it can be seen that there is a probability of 0.5 of obtaining a throughput between 0.5 and 1 when constructing a slow system with

components having tolerances specified using the 10% tolerance set. This means that about half of the systems constructed will possess a throughput above 50% while the rest will have a throughput below 50%. In contrast, it will be much harder to construct systems providing a throughput below 50% when using a 0.01% tolerance set (then the probability is approximately 0).

In reality, of course, the throughtput specification is often formulated as an inferior limit, e.g. a system must possess an 80% throughput efficiency or more. Looking again at figure 2, we can conclude (as might have been expected) that the 0.01% tolerance set provides the best probable performance; most of the samples providing throughputs between 0.9 and 1. The probable performance decreases severely as a more relaxed metric is used to set the tolerances. For the 10% tolerance set, the cumulative distribution is almost a straight line, meaning that samples are distributed more or less evenly across all throughputs from 0 to 1.

The probable performance is slightly better for a fast system than for a slow system. For example, there is a 0.55 probability that systems built using a 10% tolerance set will possess a throughput of 50% or more while there is a 0.95 probability that a system specified to 0.01% tolerances will possess a throughput of 90% or more. There is about a 0.1 maximum increase in probability of obtaining a certain throughput or more when employing a fast system rather than a slow one.

5.3.2.1.2 8-f System

The results of the Monte-Carlo simulation for the slow and fast 8f systems are presented in figure 3. The curves are slightly shifted upwards compared to figure 2 indicating that there are more low throughput value samples. Probable performance degrades slightly as the system length is increased. Note that the dashed curve (for the slow system) is bottommost for each tolerance set indicating that the slow system now provides better performance. There is about a 0.15 maximum increase in probability of obtaining a certain throughput or more when employing a slow system rather than a fast one.

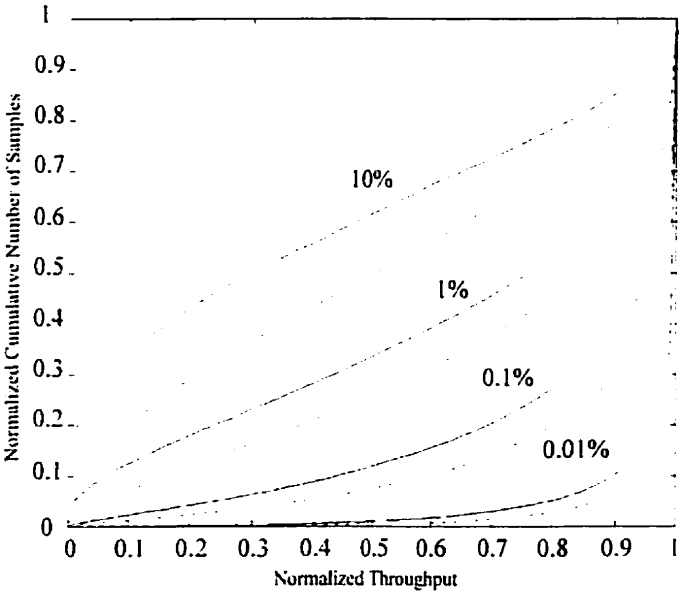

Figure 3. Plot of Cumulative Distribution versus Normalized Throughput for a Slow and Fast 8f System

5.3.1.1.3 12-f System

The results of the Monte-Carlo simulation for the 12f system are presented in figure 4 . Note that the curves are noticeably shifted upwards compared to figure 3

indicating that errors accumulate noticeably as the system length is increased. The slow system again provides better probable performance than the fast system. There is about a 0.18 maximum increase in probability of obtaining a certain throughput or more when employing a slow system rather than a fast one.

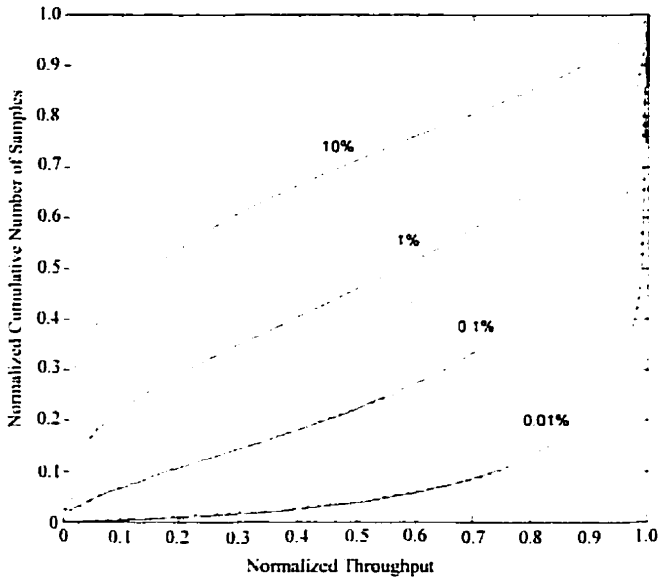

Figure 4. Plot of Cumulative Distribution versus Normalized Throughput for a Slow and Fast 12f System

5.3.1.1.4 Summary of Results

Table 3 presents a summary of the results of the preceeding subsection. The probability of obtaining a throughput of 80% or more was compared for the various tolerance sets for the slow and fast 4f, 8f and 12f systems. This throughput value was selected because it is commonly used in tolerancing work.

Table 3. Summary of Results

Number of Parameters	Tolerance Metric (%)	Probability Slow System	Probability Fast System
4f (14 Parameters)	10	0.275	0.35
	1	0.55	0.65
	0.1	0.8	0.9
	0.01	0.975	0.975
8f (20 Parameters)	10	0.25	0.2
	1	0.5	0.475
	0.1	0.7	0.725
	0.01	0.95	0.95
12f (26 Parameters)	10	0.225	0.15
	1	0.425	0.35
	0.1	0.625	0.6
	0.01	0.875	0.9

Table 3 demonstrates that the probability of obtaining a throughput of 80% or more decreases as the number of parameters increases for both the slow and fast system. It is also shown that the choice of the tolerance metric has a major impact on the yield that can be expected upon assembly. The use of a 10% tolerance metric leads to a very low yield, even for very short systems containing few parameters. Use of a 0.1% or 0.01% metric guarantees much more acceptable performance as 60% or more of the systems constructed will possess a throughput of 80% or more.

5.3.2.2. Comparisons

It is interesting to compare the results of the Monte-Carlo analysis to the results predicted with the help of a worst-case analysis or a root-sum-squares (RSS) analysis. These two methods are often used in tolerancing work to obtain quick estimates of the assembled system performance. A worst-case analysis is sometimes used to verify that a design will still function in the event of an improbable conjunction of defective or misaligned components. An RSS analysis is also used to obtain a quick estimate of the probable system response although it is known that this method is not valid since multiple

parameters are coupled in optical systems. For example, a longitudinal misalignment will decrease the lateral misalignment tolerance as the system loses telecentricity. The power loss for a combined lateral and longitudinal misalignment will not be a linear combination of the power losses for a lateral and longitudinal misalignment taken separately. Parameters can therefore not be considered to be independent.

The RSS system response can be calculated with the following equation:

$$M = \left(N_1^2 + N_2^2 + N_3^2 + N_4^2 + \ldots\right)^{1/2} \qquad \text{Eq. (1)}$$

Where M is the mean of the system response and N are the individual power losses used to set the tolerance of each of the parameters.

Table 4 compares the means of the Monte-Carlo distributions to the mean calculated with the help of the RSS method. Results are presented for the 4f, 8f and 12f systems as well as for the different tolerance metrics. The results predicted by a worst-case analysis are not included in table 4. They are equivalent to the minimum given by the Monte-Carlo distribution. Results were calculated to be equal to or less than 5% throughput for all systems and all tolerancing metrics.

Table 4. Mean of the Monte-Carlo Results for Systems 1 and 2 Compared to RSS Results

Number of Parameters	Metric (%)	Mean (%) Monte-Carlo Slow	Mean (%) Monte-Carlo Fast	Mean (%) RSS
4f (14 Parameters)	10	42.2	53.3	62.6
	1	69.0	78.5	96.3
	0.1	87.9	93.8	99.6
	0.01	98.2	99.3	99.96
8f (20 Parameters)	10	35.9	39.2	55.3
	1	60.1	63.8	95.5
	0.1	80.3	83.3	99.5
	0.01	96.0	96.4	99.95
12f (26 Parameters)	10	28.8	30.5	49.0
	1	50.5	52.8	94.9
	0.1	71.4	73.6	99.5
	0.01	92.3	92.0	99.95

Three conclusions can be drawn from table 4:

1) The means of the Monte-Carlo distributions for the fast and slow systems are almost equal for the 12f systems. A difference between the two appears as the length decreases.
2) Use of an RSS analysis leads to overoptimistic results.
3) Use of a worst-case analysis leads to severely under-optimistic results.

5.4 Summary

A Monte-Carlo analysis has shown that tolerance stackup effects are important and greatly affect the probable performance or yield of passively assembled optical interconnects. The analysis has shown that a sensitivity analysis alone is not sufficient to set tolerances for the components as it takes no account of the simultaneous interaction of parameters. This chapter had two main goals:

1) Provide answers as to whether worst-case or RSS analyses are adequate to estimate stackup effects.
2) Provide design guidelines to system designers by investigating how stackup evolves with:
    i) The severity of the loss criteria used to establish the component tolerances.
    ii) The number of tolerance parameters.
    iv) The f-number of the system.

Table 4 has shown that worst-case or RSS analyses do not provide accurate estimates of probable performance. A Monte-Carlo analysis must be performed. It is interesting to note that software tools able to perform Monte-Carlo tolerancing of optical interconnects are being developed [9]. The present chapter provides a strong motivation for the use of such tools to design optical interconnects.

Figures 2 to 4 demonstrate that there exists a strong relationship between the tolerance metric (10%, 1%, 0.1% or 0.01%) and the probable performance of systems assembled using components specified to those tolerances. As expected, the most severe tolerance metric (0.01%) provides the best probable performance (most of the assembled systems will possess a throughput above 90%) while the most relaxed metric (10%) provides the worst probable performance (throughputs will be spread almost evenly between 0 and 1). Results indicate that the 20% or 10% power loss metrics commonly used to set tolerances will result in severe tolerance stackup effects even for short interconnect lengths.

Tolerance metrics of 1% power falloff with respect to the maximum or less should be used to guarantee reasonable performance for passively assembled systems.

The number of parameters or the length of a system has been shown to affect the probable performance. Looking at table 3, it can be seen that the longer a system is and the greater the number of parameters it contains, the lower the mean of the Monte-Carlo distribution. The decrease can amount to a 10% to 15% loss in the probability of obtaining a certain performance with each 4f (6 parameters) addition. Very long systems containing many parameters should thus be avoided or the number of parameters in a system should be kept small. Progressively more severe tolerancing metric must be used with longer systems to maintain a constant assembly yield. Longer systems will be more costly.

The effect of the system speed or f-number is not clear. Fast systems seem to possess an advantage in comparison to slow systems as regards tolerance stackup. However, the advantage is small; there is approximately a 15% increase in the probability of obtaining a certain throughput over an f-number range of f/16 to f/3.38. Note also that fast systems will possess more severe tolerances, which increases cost. F-number considerations should therefore not be used to guide the design of optical interconnects as regards tolerance stackup.

5.5 References

[1] Y. Liu, B. Robertson,.G. C. Boisset, M. H. Ayliffe. R. Iyer. and D. V. Plant, "Design, implementation and characterization of a hybrid optical interconnect for a four-stage free-space optical backplane demonstrator", *Applied Optics*, Vol. 37, No. 14, 10 May 1998.

[2] X. Zheng, P.J. Marchand, D. Huang, O. Kibar, N.S.E. Ozkan and S.C. Esener, "Optomechanical design and characterization of a printed-circuit-board-based free-space optical interconnect package", *Applied Optics*, Vol. 38, No. 26, 10 September 1999.

[3] D.T. Neilson and E. Schenfeld, "Plastic Modules for free-space optical interconnects", *Applied Optics*, Vol. 37, No. 14, 10 May 1998.

[4] S. D. Nigam and J. U. Turner, "Review of statistical approaches to tolerance analysis", *Computer-Aided Design*, Vol. 27, No. 1, pp. 6-15, 1995.

[5] Zaleta, D.; Patra, S.; Ozguz, V.; Ma, J.; Lee, S.H., "Alignment tolerancing of free-space MCM-to-MCM optical interconnect", *Proceedings of the 45th Electronic Components and Technology Conference*, P. 1286 –1293, 1995.

[6] CODE V available from Optical Research Associates, 3280 E. Foothill Blvd. Suite 300, Pasadena, California.

[7] Mathematica available from Wolfram Research inc., 100 Trade Center Drive Champaign, IL 61820-7237, USA.

[8] David T. Neilson, "Tolerance of optical interconnections to misalignment", *Applied Optics*, Vol. 38, No. 11, 10 April 1999.

[9] Steven P. Levitan, Timothy P. Kurzweg, Philippe J. Marchand, Mark A. Rempel, Donald M. Chiarulli, Jose A. Martinez, John M. Bridgen, Chi Fan, and Frederick B.

McCormick, "Chatoyant: a Computer-Aided- Design Tool for Free-Space Optoelectronic Systems", Applied Optics, Vol. 37, No. 26, 10 September 1998.

Chapter 6: Tolerancing Polarization Losses

6.1 Introduction

The third hypothesis employed in the design of the optical interconnect presented in chapter 3 assumes that power losses through fabrication errors in components that affect the polarization of light are not significant and that therefore it is not necessary to calculate a polarization tolerance budget. However, minimizing optical power losses is important as power losses decrease system performance because receiver switching speeds are energy dependent [1] and the semiconductor lasers which are used as light sources possess limited output powers [2].

While some effort has been spent on tolerancing the optomechanical aspects of optical interconnects [3][4][5], little information is available in the literature on the tolerancing of other system aspects. In particular, polarization losses in optical interconnects have rarely drawn much attention (see [6][7][8] for some discussion of the topic) and the mechanisms of accumulation of polarization losses ("tolerance stackup") in a complex optical interconnect system have not, to the author's knowledge, been previously investigated. The question then arises as to whether the tolerances commonly specified for the polarization-based components (which are often determined by what is standard for the optical shop) are appropriate.

Polarization-based beam combination and routing techniques have been employed in a large majority of the demonstration systems implemented by various research groups [6][7][9][10][11]. The fact that polarization losses in free-space optical interconnects

have received so little attention is surprising considering the fact that in systems that use polarizing beam splitter quarter-wave plate (PBS/QWP) assemblies (figure 1) to perform beam combination functions, the optical power losses can easily amount up to 5% or more of the input light per pass per PBS/QWP assembly when commercial grade components are used. Losses are thus likely to accumulate rapidly in a system employing multiple PBS/QWP assemblies.

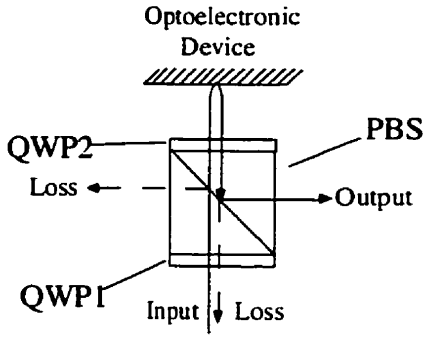

Figure 1: Diagram of PBS/QWP assembly.

The dotted arrows in figure 1 illustrate the leakage paths resulting from polarization losses in a PBS/QWP assembly. This polarization leakage is likely to degrade the contrast ratio of the modulated beams by interfering coherently with them or cause instabilities when reflecting back to a laser source [12].

Polarization losses originate from two factors:

1) Deviations from specifications in polarization based components.

2) Imperfections in the polarization of input light sources.

There is thus a need to rigorously study polarization losses in optical interconnects. This would be useful for a number of reasons:

1) Allow the system designer to calculate a polarization tolerance budget. This budget can be divided into two parts:

i) calculate the tolerances of polarization-based components (extinction ratio of PBS, retardance accuracy of QWPs, etc.) and verify whether commercial tolerances are sufficient to ensure the intended level of performance for a given system.

ii) calculate the tolerances for the polarization properties of the source and delivery system (diode laser, polarization maintaining (PM) fiber, Vertical Cavity Surface Emitting Laser (VCSEL) array).

2) Determine the effect of tolerance stackup, i.e. what polarization loss penalty must be included in the power budget once the source and component tolerances have been set. To perform this analysis, a Monte-Carlo simulation is necessary as the throughput as a function of the polarization components parameters is non-linear (see [13] for some example throughput response functions) and so the moments of the function such as the mean and standard deviation cannot be evaluated analytically [14].

The methodology illustrated in figure 2 is used to respond to the needs outlined above.

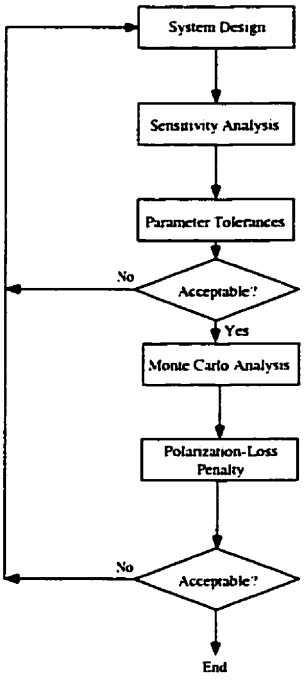

Figure 2. Flowchart of tolerancing method.

An initial system design is converted to a parametric mathematical model by using the Stokes vectors and Mueller matrix representation of polarization states. A sensitivity analysis is then performed and tolerances calculated for the individual parameters. These tolerances must then be judged to be acceptable or not from a manufacturing standpoint. They are then input into a Monte-Carlo analysis in order to predict the probable loss penalty when using those components to construct an actual system. If the loss penalty is deemed acceptable, the design cycle ends. However, if the probable loss penalty exceeds the allocated polarization loss margin, the tolerances must be modified and another iteration made.

The methodology is illustrated with the help of an application example consisting of a free-space optical interconnect designed for board-to-board applications. Other possible applications of this method include the tolerancing of compact disc pickup heads,

telecommunication isolators or circulator components and any free-space optical system that uses polarization-based components.

6.2. Modeling Polarization Properties

Mueller matrices and Stokes vectors are used to model the polarization properties of the polarization components and the laser source. The Stokes vector is a method of describing unpolarized, partially polarized or completely polarized light through the use of four measurable quantities. Mueller matrices describe the interaction of the Stokes vector with a component affecting the state of polarization of the light. A thorough introduction to mathematical methods in polarization analysis can be found in [13].

6.3. Application Example: A Free-Space Optical Interconnect

The optical interconnect presented in chapter 3 was selected to serve as an application example. The components that modify the state of polarization of the beams propagating in the interconnect (PBSs and QWPs) were modeled using Mueller matrices. The optoelectronic reflection modulators only change the handedness of the polarization upon reflection and were therefore modeled as mirrors. Polarization aberrations that could be introduced in the beams by the other optical elements such as the diffractive fanouts and minilens arrays were ignored due to the use of slow, f/16 beams in the system [16]. The angular position of the PBSs was assumed to be perfect with respect to the rest of the system. This is a necessary assumption as the angular mechanical alignment tolerances of a PBS are usually much smaller than a degree [17] whereas the angular field of view for a commercial component is equal to ±2° [16]. This signifies that the power losses caused by tilt introduced into the beams upon reflection from a misaligned PBS cause power losses that are much more significant than the associated polarization

leakage losses. Figure 3 is a schematic drawing representing the components included in the Mueller matrix model.

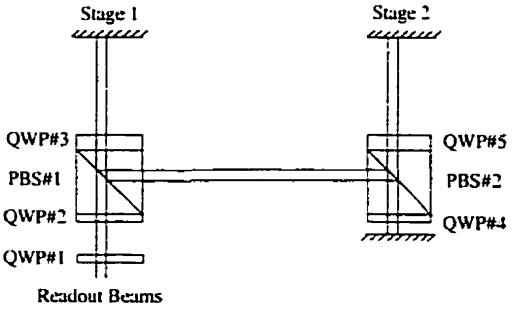

Figure 3. Schematic diagram of system model.

6.3.1 Component Characterization Results

Figure 4 shows the setup used to perform characterization of the components. A 50/50 beam splitter pellicle was mounted at 45° relative to a collimated $2\omega_o$=1200μm diameter beam output from a single-mode polarization maintaining fiber (PM) - collimating lens assembly. Excellent linearity in the output polarization is ensured by placing a polarizer after the PM fiber (specified to at least a 10, 000:1 extinction ratio). The beam reflected from the pellicle was used as a reference to decrease the influence of power fluctuations of the input light source (about ±2%) on the power meter readings. All power measurements were done using a dual-channel power meter.

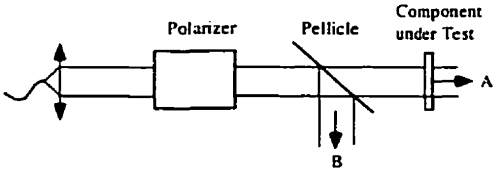

Figure 4. Diagram of setup used for component characterization.

6.3.1.1 Quarter-Wave Plates (QWPs)

The quarter-wave plates used were composed of a layer of thin birefringent quartz sandwiched between two fused silica or BK7 optical windows that provide mechanical

support. The quartz layer must be 23.4μm thick for the plate to function as a zero-order quarter-wave plate at 852nm. Deviations from the nominal quartz thickness will translate into retardance variations for the wave propagating in the crystal. The quarter-wave plates were specified to a $\pm\lambda/200$ tolerance. This means that the thickness must be controlled to a tenth of a micron to respect the specified tolerance.

The QWPs used in this system were fabricated in a single batch which means that a large sheet of quartz was polished and then diced to provide multiple components. It can therefore be assumed that all the QWPs used in the system possess a uniform retardance value. This assumption was experimentally confirmed by measuring the retardance of many QWPs as described below.

The differential retardance of the QWPs could not be measured directly. The indirect method used for characterization consists in sending a linearly polarized beam into the QWP and varying its rotation angle such that the output polarization is as close to circular as possible [21]. From the measurement of the extinction ratio the retardance can be calculated with the following formula:

$$\delta = \sin^{-1}\left(\frac{2\eta}{\eta^2+1}\right) \qquad \text{Eq. (1)}$$

where δ is the differential retardance of the quarter-wave plate and η is the ratio of the amplitudes (not intensity) of both axes of the light output from the QWP.

The precision of this measurement depends on the polarization linearity of the light delivered at the input and the precision of the angular alignment of the retarder fast or

slow axis with respect to the input polarization. The linear polarization at the QWP input was measured to have an extinction ratio better than (12.000:1) which can be assumed to be infinite. The QWP rotational position can be adjusted to about ±1° (estimated manual adjustment sensitivity).

The average circularity at the output was measured to be 1.5:1 (for four QWPs). The maximum variation on the ellipticity measurement for each QWP was 0.05. These numbers translate into a λ/33 differential retardance error from the perfect λ/4 when using equation 1. The QWPs in the system thus possess a retardance of either λ/4+ λ/33 or λ/4- λ/33. This does not respect the specified tolerance of ± λ/200 and represents a serious fabrication error. The uncertainty on the measurement is estimated to be equal to ± λ/350.

6.3.1.2 PBS/QWP Assembly

The PBS/QWP assemblies were pre-assembled by the commercial vendor. They were characterized to determine the throughput coefficients. Two assemblies were cascaded in order to measure the total throughput. This was measured to be 85% ±1. The measured throughput is 5% lower than calculated from the manufacturers specifications ($(kp(1-ks))^2 = (0.96(1-0.01))^2 = 0.95$). The difference is attributable to the poor quality of the QWPs used in the system. Pairs of crossed plates will tend to partially compensate their individual retardance errors and produce polarization of reasonably good quality. This is an interesting result as it signifies that the QWPs in PBS/QWP assemblies do not need to possess a very precise 90 degree retardance value: they only need to have uniform retardances.

6.3.2 Demonstration of the Method

6.3.2.1 Sensitivity Analysis

A sensitivity analysis was performed. A critical part of the sensitivity analysis consists in selecting a power falloff metric to delimit the tolerable variation range. A relaxed metric will mean that components might be easier to fabricate but might provide lower performance in the assembled system due to accumulated losses. A more severe metric will mean that tolerances are tighter, providing a lower loss but also increasing fabrication cost. The number of parameters to simulate is large: each QWP and PBS in the interconnect has two independent parameters for a total of fourteen parameters as shown in equation 2.

$$M_{System} = f(\theta_1, \delta_1, \theta_2, \delta_2, \theta_3, \delta_3, \theta_4, \delta_4, \theta_5, \delta_5, Kp_1, Ks_1, Kp_2, Ks_2) \quad \text{Eq. (2)}$$

Where θ and δ represent the orientation of a QWP fast axis and its retardance value, respectively. Kp and Ks are the PBS transmission coefficients for p and s polarization. Following the sensitivity analysis, two metrics (1% and 10% power falloffs) are used to delimit tolerance ranges for the parameters. Two metrics were chosen in order to compare the loss penalties associated with the choice of a conservative metric (1%) or a more relaxed metric (10%).

6.3.2.1.1 Effect of Imperfect PBS.

Commercial grade PBSs are generally specified to be better than 96% transmissive for p-polarization and 99% reflective for s-polarization. This means that a standard PBS may reflect up to 4% of a perfectly p-polarized beam of light and transmit

up to 1% of a similarly perfectly s-polarized beam of light for a total of 5% loss per PBS/QWP assembly. The light contributing to these losses is often termed "polarization leakage" and will be distributed to stages located before and after the input stage. It is important to mention that the possible impacts of polarization leakage will be greatly influenced by the physical layout of the system, i.e. whether a leaked beam is directed to the detectors or VCSELs/modulators at a previous stage and the type of optoelectronic components used and their tolerance to feedback or crosstalk. Each system has to be analyzed independently and the possible polarization leakage paths determined. This was done for the interconnect system under study.

Note that only three cases have been studied: 1) leakage to previous stage 2) feedback and 3) leakage to next stage. They do not constitute the only possible paths. Higher order leakage affecting stages further removed from the destination stage are possible but the power of the light reaching those stages will likely be much lower than for the cases outlines above. Note that all the cases studied assume that the other components and the source are perfect as regards their polarization properties.

1) Leakage to previous stage

A portion (1-kp) of the p-polarized beam incident on the PBS is reflected and channeled to the previous stage where it meets the second PBS and another portion (1-kp) is reflected to the detectors located at the previous stage (fig. 5). The total percentage of light leaked is $(1\text{-}kp)^2$. Note that this light has not been modulated. This DC signal will be rejected by the differential receivers used in this system but could be a problem in

systems employing single-ended receivers where the leakage DC signal will cause the decision threshold of the receiver circuit to shift.

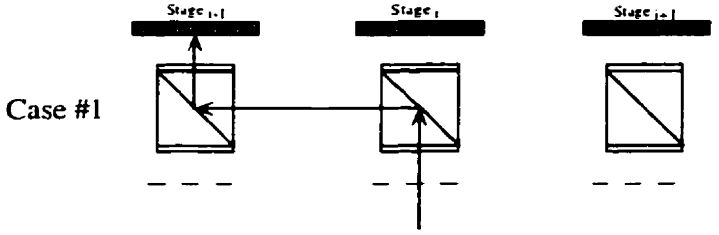

Figure 5. Primary leakage to first stage.

2) Feedback to same stage.

This probably constitutes the most troublesome case: a portion of the signal directed to the detectors at the next stage is reflected back to the modulators (fig. 6). The optical path length of this feedback path is about 10f=85mm, which means that the time of flight will be about 0.25ns between the moment a bit leaves the modulator and the moment it comes back. At high modulation speeds (1Gb/s) this constitutes a significant amount of the bit period and could lead to significant levels of intersymbol interference (ISI). However, it can be calculated that the relative amount of reflected power amounts to a maximum of 0.16% of the light that leaves the modulators. This number can be considered insignificant for a modulator based system but could constitute a problem for VCSEL based systems [15].

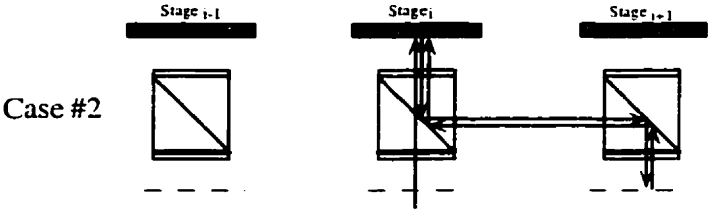

Figure 6. Feedback to stage$_i$.

3) Leakage to next stage

Here, a fraction (ks) of the s-polarized light directed to the second PBS carries on to be reflected to the modulators at the second stage where the light will interfere coherently with the unmodulated readout beams incoming on the modulators (fig. 7). Again, this effect is presumed negligible in this case because of the low power in the leaked beam (less than 1%) but could constitute a problem in VCSEL based interconnects.

In summary, leakage is not likely to affect system operation significantly. However, a VCSEL-based system would be much more sensitive to such leakage because feedback would affect the performance of the active devices.

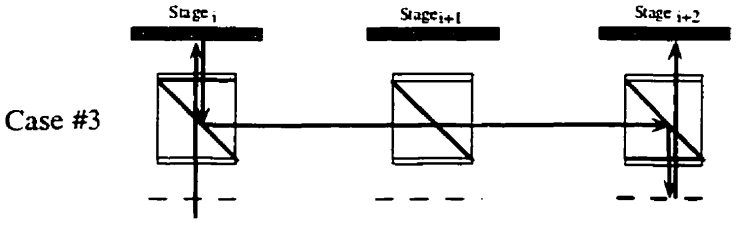

Figure 7. Primary leakage to next stage.

6.3.2.1.2 Effect of Quarter-wave Plates Retardance Errors

A sensitivity analysis of the QWPs retardance on the throughput was performed. Figure 8 shows a plot of throughput versus retardance deviation from the perfect 90° for the five QWPs in the system. Perfectly linear p-polarization is assumed at the input.

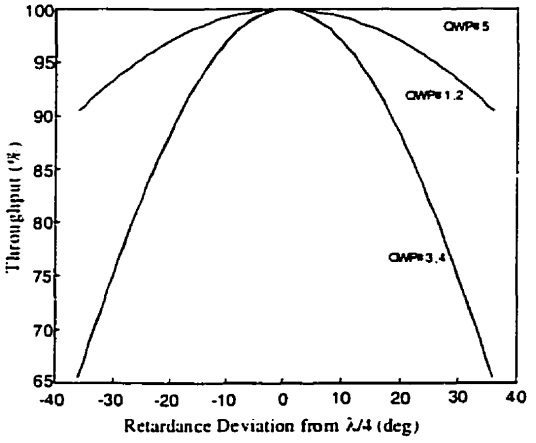

Figure 8. Plot of throughput versus retardance deviation.

Figure 8 demonstrates that the throughput is affected by errors in the retardance values of the QWPs. While errors in QWP #5 have no effect on the throughput measured at the detector (although it would affect the throughput to the next stage), the system is seen to be sensitive to errors in QWP#1,2 and QWP#3 and #4. The much faster throughput fall-off of the curves for QWP #3 and QWP #4 compared to QWP #1 and QWP#2 is due to the degradation in the polarization state of the beam as it passes twice through the same QWP.

6.3.2.1.3 Effect of QWPs Rotational Misalignment

Figure 9 shows a plot of throughput versus QWP rotational misalignment. The curves follow the same order as figure 8.

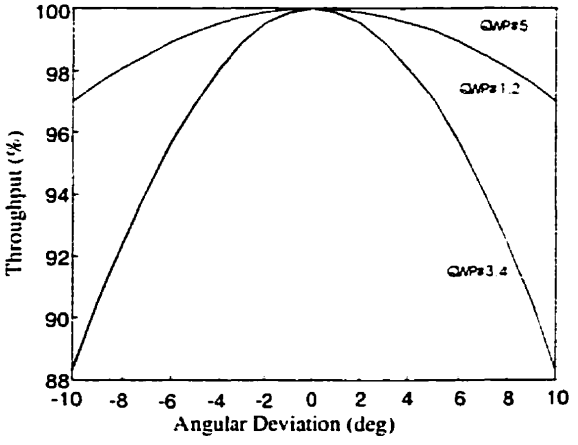

Figure 9. Throughput versus QWP rotational misalignment.

Figure 9 shows that there is a certain similarity between having a rotationally misaligned perfect QWP and a well-aligned imperfect QWP as the two situations will impart a deviation from the nominal $\lambda/4$ retardance on the wave traversing it.

6.3.2.1.4 Input Polarization Azimuthal Orientation

Figure 10 shows a plot of throughput versus the azimuthal orientation of the input p-polarization. Such a variation in the input azimuthal angle would result, for example, from having a rotationally misaligned PM fiber fast or slow axis with respect to the system axis. It shows that power will drop by about 1% when the input linear polarization is rotated by ±6°.

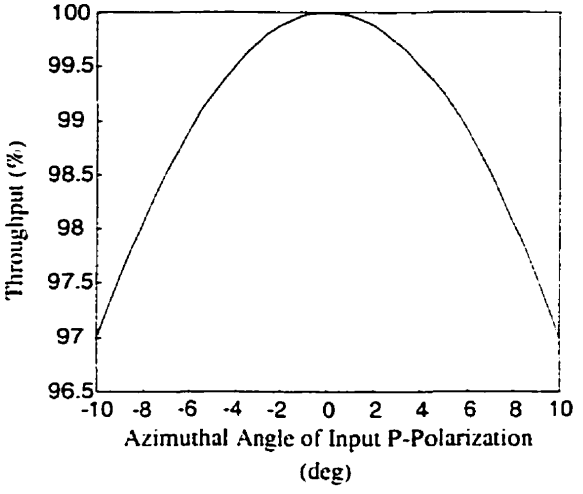

Figure 10. Throughput versus azimuthal orientation of input P-polarization.

6.3.2.1.5 Input Polarization Ellipticity

Figure 11 plots the throughput versus ellipticity for right-hand elliptically polarized light launched from the source. Note that the ellipticity is defined as the intensity ratio of the s axis over the p axis. An ellipticity of 0 thus represents perfectly linear p-polarization.

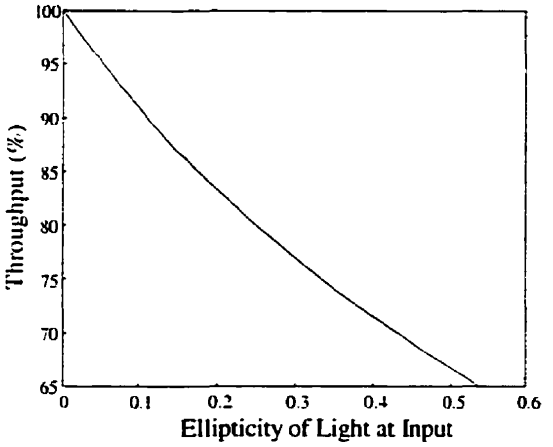

Figure 11. Throughput versus ellipticity at input.

6.3.2.2 Summary of Sensitivity Analysis

A set of tolerances for two falloff metrics (1% and 10%) calculated from the above graphs as well as the commercial tolerances available for each component are presented in table 1.

Table 1. Summary of tolerances

Parameter	Tolerances (1%)	Tolerances (10%)	Commercial Tolerances
QWP#1,2 θ	± 6°	± 18°	± 1°
QWP#1,2 δ	± 10°	± 37°	± 1.8°
QWP#3,4,5 θ	± 3°	± 9°	± 1°
QWP#3,4,5 δ	± 5°	± 18.5°	± 1.8°
Source θ	± 6°	± 18.5°	± 2°*
Source ε	+0.01	+0.11	+0.001
PBS K_p	± 0.5%	± 5%	± 1%
PBS K_s	± 0.5%	± 5%	± 1%

* This is defined for a system using polarization maintaining fiber as a light delivery system.

Note that the commercial specifications are better than the tolerances calculated with a 1% power loss metric in almost all cases except for the PBS transmission coefficients. However, it is necessary to investigate the impact of the accumulation of these tolerances in the system. This requires a Monte-Carlo analysis.

6.3.3 Monte-Carlo Analysis

A Monte-Carlo analysis was performed. The set of tolerances calculated above was used to delimit the range of the input tolerance probability distributions. When performing such an analysis, it is important to understand the impact that the input probability distributions have on the final Monte-Carlo distribution. A proper distribution for each parameter must be chosen in order to obtain useful results. The precise shape of these distributions is highly coupled to the manufacturing process. In this case, after communicating with the manufacturer, it was decided to use a truncated Gaussian distribution with its peak at the midway point between the nominal value and the high side tolerance to represent the retardance value distribution of the QWPs as there is a tendency of optical shops to leave elements on the high side of the thickness tolerance. Truncated Gaussian distributions with the peak located at the nominal value were used to represent the QWP angular alignment and PBS transmission coefficient distributions. Both distributions were truncated at the 3σ points, which lie at the tolerance limits. These probability distributions are thought to be representative of common optical shop practices (see [22] for more details). A hundred and fifty thousand samples were used to obtain stable results and a good accuracy. The calculation necessitated about 5 hours of CPU time on a SunSparc 20 station.

6.3.3.1 Monte-Carlo Analysis for 1% Falloff Metric

The tolerances for each parameter calculated with the 1% power falloff metric were input into the Monte-Carlo analysis. The source ellipticity was assumed to vary between 0 and 0.01. Figure 12 shows a graph of the resulting throughput histogram distribution.

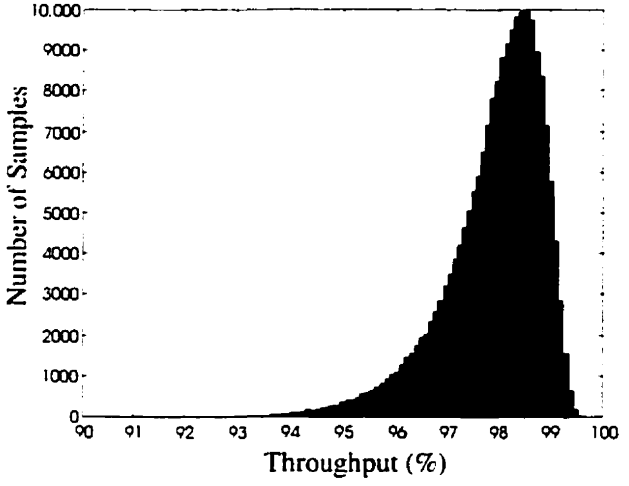

Figure 12. Histogram of number of samples versus throughput for tolerances calculated using 1% falloff metric.

Notice that the distribution is not normal in shape but is skewed towards higher values. The mean of the distribution is located at 97.9% and the standard deviation is 0.94. The 99% confidence interval cutoff value of the distribution was calculated to be located at a throughput value of 94.9% (i.e. 99% of the systems built with components using those tolerances would possess a throughput value greater than 94.9%).

6.3.3.2 Monte-Carlo Analysis for 10% Falloff Metric

The tolerances for each parameter calculated with the 10% power falloff metric were input into a Monte-Carlo analysis. The source ellipticity was allowed to vary between 0 and 0.11. Figure 13 shows a graph of the resulting throughput distribution.

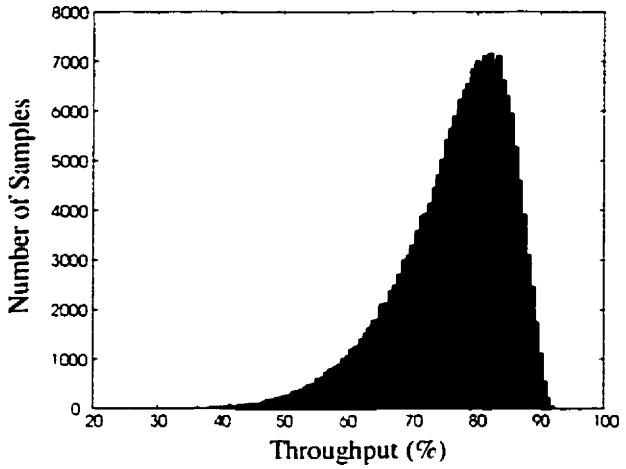

Figure 13. Histogram of number of samples versus throughput for tolerances calculated using 10% falloff metric.

The distribution now occupies a much larger interval of values (from 35 to 92%). The mean is equal to 76.4% and the standard deviation is 8.7. The 99% confidence interval cutoff is now located at a throughput value of 50%. The use of a more relaxed tolerance metric has led to a severe degradation in the confidence interval cutoff value.

6.3.3.3 Monte-Carlo Analysis for Commercial Tolerances

The effect of using standard commercial grade components was studied. The emitter was modeled as a polarization maintaining (PM) fiber emitting linear p-polarized light possessing a nominal contrast ratio of 30dB (0.001 intensity ratio) with an arbitrary ±0.002 s-polarized noise factor superposed 90 degrees in phase (in effect producing right-hand circularly polarized light) to model random mode coupling between the axes of the fiber due to stress or environmentally induced birefringence. This represents the type of source used in this system. The resulting polarization ellipse is assumed to rotate by ±2° around the p-axis (commercial specification for alignment of the fiber fast axis relative to the connector ferrule).

Figure 14 shows the resulting Monte-Carlo analysis results. Again, 150000 samples were calculated. The mean of the distribution is equal to 91.1% and the standard deviation is equal to 0.37%. The 99% confidence interval boundary is located at 90.4%.

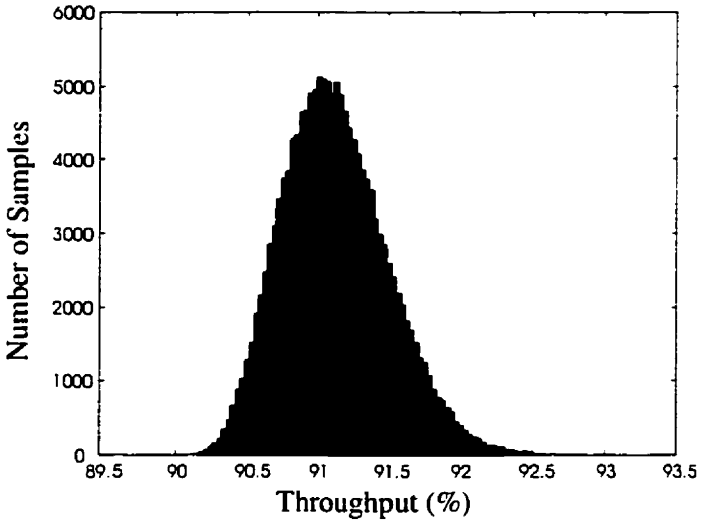

Figure 14. Histogram of number of samples versus throughput for commercial tolerances.

As can be seen on figure 14, standard commercial grade polarization components should guarantee that a worst-case power falloff of slightly less than 10% should be obtained.

6.3.3.4 Monte-Carlo Analysis for Optical Interconnect

The effects of using the components characterized in section 3 to construct an actual system were investigated. Commercial grade components were assumed except that QWPs having a uniform $\lambda/33$ error in the retardance value (as measured) were modeled.

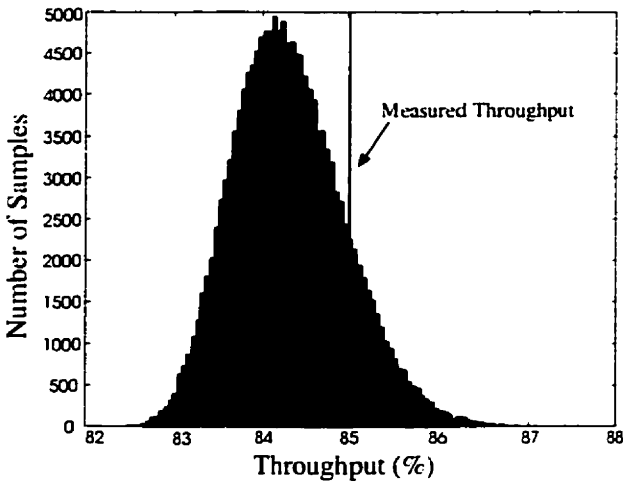

Figure 15. Histogram of number of samples versus throughput distribution for demonstrator system.

Figure 15 demonstrates that the experimentally measured throughput of 85% ±1 (see section 3.1.2) falls comfortably within the calculated distribution. The mean of the distribution is equal to 84.3%. This result validates the simulation method.

6.4. Summary

This chapter has tried to evaluate the importance of polarization losses in free-space optical interconnects. A method to rigorously calculate polarization losses and tolerance polarization-based components in free-space optical interconnect systems was presented. This is necessary in order to accurately quantify power losses resulting from the use of components or sources having imperfect polarization characteristics and answers the needs outlined in the introduction:

1) To specify tolerances of polarization-based components.

2) To specify tolerances for the polarization properties of the source.

3) To determine the effect of tolerance stackup, i.e. the polarization loss penalty that must be included in the power budget.

The method was demonstrated with the help of a free-space optical interconnect application example. The availability of measured data for the interconnect throughput verified the validity of the simulation model. The throughput measured when using components possessing commercial tolerances was found to fall within the simulation result distribution.

A detailed sensitivity analysis for the free parameters in the interconnect was presented. The throughput falloff curves were used to delimit tolerance ranges for the parameters according to two different power falloff metrics (1% and 10%). Table 2 presents a list of tolerances calculated from the throughput curves.

It was found that using pairs of crossed wave plates as present on the PBS/QWP assemblies acts as a partial compensation mechanism for the fabrication errors in the QWPs retardance. Using wave plates possessing equal retardances insures that the power losses due to polarization leakage caused by fabrication errors in the wave plates are kept to a minimum. It is thus preferable to use wave plates manufactured in the same batch when fabricating PBS/QWP assemblies.

The output Monte-Carlo distributions for graphs 12 and 13 (1% and 10% falloff metrics) look very similar in general shape except that the mean and standard deviations of the

distribution calculated using a 10% metric are very different from the distribution calculated using a 1% metric: the mean is about 20% less and the standard deviation is roughly 9 times greater for the distribution calculated using a 10% falloff metric compared to the distribution calculated using a 1% falloff metric. But perhaps more importantly, the confidence interval cutoff value of the two distributions (the value that is included in the power budget to evaluate polarization losses) are also very different: 94.9% for the 1% falloff metric compared to 50% for the 10% falloff metric. Clearly then, the choice of a more relaxed metric has led to a severe and rapid degradation of the probable throughput. This confirms the importance of tolerance stackup in a complex system employing many polarization-based components: this must be taken into account when selecting a throughput falloff metric to set fabrication tolerances.

Commercial tolerances are superior for all parameters (except the PBS transmission coefficients for the p and s polarizations) to the set of tolerances calculated using a 1% power falloff metric. There is then little sense in specifying tolerances calculated using a metric that translate to tolerances looser than those commercially available. The cutoff value for the Monte-Carlo distribution calculated using commercial tolerances is 90.4%. The difference between this value and the cutoff for the distribution calculated using the 1% set of tolerances is entirely due to the lower transmission coefficients of the PBS. Commercial tolerances seem to be sufficient to obtain an adequate level of performance in most cases for this type of system.

The decrease in the cutoff value of the distribution does not seem to be linear with the number of PBS/QWP assemblies used. This means that a very severe power falloff metric (<<10%) must be used to set tolerances for a system cascading three or more PBS/QWP assemblies. Commercial specifications might not be good enough in this case.

Note that the above analysis remains largely valid for a VCSEL-based system employing the same basic optical layout. Replacing the modulators with a VCSEL array would probably slightly increase the tolerances for the source azimuthal orientation and ellipticity. Feedback to the active devices due to polarization leakage might cause power or wavelength fluctuations of the VCSEL output [15]. This might degrade system performance and should be considered in the system design.

6.5. References

[1] T.K. Woodward, A. V. Krishnamoorthy, A. L. Lentine, K. W. Goossen, J. A. Walker, J. E. Cunningham, W. Y. Jan, L. A. D'Asaro, M. F. Chirovsky, S. P. Hui, B. Tseng, D. Kossives, D. Dahringer and R. E. Leibenguth, "1-Gb/s Two-Beam Transimpedance Smart-Pixel Optical Receivers Made from Hybrid GaAs MQW Modulators Bonded to 0.8μm Silicon CMOS", *IEEE Photonics Technology Letters*, Vol. 8, No. 3, pp. 422-424, March 1996.

[2] F. Tooley, P. Sinha and A. Shang, "Time-differential operation of an optical transceiver", Optics in Computing. 1997 Technical Digest Series Vol.8. Postconference Edition, Topical Meeting on Optics in Computing - OC97, Incline Village, NV, USA, pp. 73-75, 18-21 March 1997.

[3] D. Zaleta, S. Patra, V. Ozguz, J. Ma and S. H. Lee, "Tolerancing of board-level-free-space optical interconnects," *Applied Optics*, Vol. 35, No. 8, pp. 1317-1327, 10 March 1996.

[4] S. P. Levitan, T. P. Kurzweg, P. J. Marchand, M. A. Rempel, D. M. Chiarulli, J. A. Martinez, J. M. Bridgen, C. Fan and F. B. McCormick, "Chatoyant: a computer-aided-design tool for free-space optoelectronic systems", *Applied Optics*, Vol. 37, No. 26, pp. 6078-6092, 10 September 1998.

[5] D. T. Neilson, "Tolerance of optical interconnections to misalignment", *Applied Optics*, Vol. 38, No. 11, pp. 2282-2290, 10 April 1999.

[6] F.B. McCormick, T. J. Cloonan, F. A. P. Tooley, A. L. Lentine, J. M. Sasian, J. L. Brubaker, R. L. Morrison, S. L. Walker, R. J. Crisci, R. A. Novotny, S. J. Hinterlong, H. S. Hinton and E. Kerbis, "Six-Stage digital free-space optical switching network using symmetric self-electro-optic-effect devices", *Applied Optics*, Vol. 32, No. 26, pp. 5153-5171, 10 September 1993.

[7] G. C. Boisset, M. H. Ayliffe, B. Robertson, R. Iyer, Y. S. Liu, D. V. Plant, D. J. Goodwill, D. Kabal and D. Pavlasek, "Optomechanics for a four-stage hybrid-self-electro-optic-device-based free-space optical backplane", *Applied Optics*, Vol. 36, No. 29, pp. 7341-7358, 10 October 1997.

[8] M.H. Ayliffe and D. V. Plant, "A Generalized Method for Tolerancing Polarization Losses in Free-Space Optical Interconnects", Optics in Computing. 1997 Technical Digest Series Vol.8. Postconference Edition, Topical Meeting on Optics in Computing - OC97, Incline Village, NV, USA, pp. 221-223, 18-21 March 1997.

[9] D. T. Neilson, S. M. Prince, D. A. Baillie and F. A. P. Tooley, "Optical Design of a 1024-channel free-space sorting demonstrator", *Applied Optics*, Vol. 36, No. 35, pp. 9243-9252, 10 December 1997.

[10] F. B. McCormick, T. J. Cloonan, A. L. Lentine, J. M. Sasian, R. L. Morrison, M. G. Beckman, S. L. Walker, M. J. Wojcik, S. J. Hintelong, R. J. Crisci, R. A. Novotny and H. S. Hinton, "Five-Stage free-space optical switching network with field-effect transistor self-electro-optic-effect-device smart-pixel arrays", *Applied Optics*, Vol. 33, No. 8, pp. 1601-1618, 10 March 1994.

[11] M. Yamaguchi; T. Yamamoto; K. Yukimatsu; S. Matsuo; C. Amano; Y. Nakano; T. Kurokawa, "Experimental investigation of a digital free-space photonic switch that uses exciton absorption reflection switch arrays", *Applied Optics*, Vol. 33, No. 8, pp. 1337-1343, 10 March 1994.

[12] S. Jiang, Z. Pan, M. Dagenais, R. A. Morgan and K. Kojima, "Influence of External Optical Feedback on Threshold and Spectral Characteristics of Vertical-Cavity Surface-Emitting Lasers", *Photonics Technology Letters* , Vol. 6, No. 1, pp.34-36, January 1994.

[13] R.M.A Azzam and W.M. Bashara, *Ellipsometry and Polarized Light*, North-Holland Editor, Amsterdam, 1977.

[14] S. D. Nigam and J. U. Turner, "Review of statistical approaches to tolerance analysis", Computer-Aided Design, Vol. 27, No. 1, pp. 6-15, 1995.

[15] B. Robertson, "Design of an optical interconnect for photonic backplane applications", *Applied Optics*, Vol. 37, No. 14, pp. 2974-2984, 10 May 1998.

[16] J. L. Pezzanti and R. A Chipman, "Angular dependence of polarizing beam-splitter cubes", *Applied Optics*, Vol. 33, No. 10, pp. 1916-1928, 1 April 1994.

[17] F. Lacroix, "Analysis and Implementation of a Clustered, Scaleable and Misalignment Tolerant Optical Interconnect", Chpt 3, Master of Engineering Thesis, McGill University, Montréal, Canada, 1999.

[18] P. A. Williams, A. H. Rose, C. M. Wang, "Rotating-polarizer polarimeter for accurate retardance measurement", *Applied Optics*, Vol.36, No. 25, pp. 6466-72, 1 Sept. 1997.

[19] CODE V Version 8.30 Reference Manual, Chapter 6, pp. 65-67, Optical Research Associates, 3280 East Foothill Boulevard, Pasadena, California, California 91107, August 1998

Chapter 7: Implementation of a Photonic Backplane.

7.1 Introduction

This chapter presents the assembly and characterization results for the multi-stage, scalable, point-to-point optical interconnect designed to link optoelectronic chips at the backplane level presented in chapter 3. It is designed to tolerate large amounts of lateral and longitudinal misalignments (in the tens of microns laterally and hundreds of microns longitudinally) and is thus seen as an ideal candidate for the implementation of a passively aligned optical interconnect where modules can be inserted and extracted in a repeatable fashion.

Two sets of goals are pursued in this thesis: 1) Demonstrate a functioning photonic backplane possessing certain optomechanical properties and 2) Verify hypotheses used in designing the optical interconnect. Implementation constitutes the only way to verify whether the experimental performance matches the predicted theoretical performance. The two series of goals are listed below:

1) Optomechanical Properties

   i) Passive alignment of the optical modules within the supporting optomechanical structure. This would guarantee systems that are simple to assemble.

   ii) Repeatable insertion and extraction of the modules making them easily replaceable in case of failure (this is especially important for the Optoelectronic Chip Module as it houses an active device).

iii) Stability. The system stays aligned without needing adjustment once optimal alignment has been achieved.

2) Design Hypotheses. In designing the system, the following hypotheses were made:

i) Gaussian beam propagation theory is adequate to calculate misalignment tolerances.

ii) There is no simultaneous interaction between multiple tolerance parameters when assembling a system. Tolerance stackup is negligible.

iii) Power losses due to imperfections in components that affect the state of polarization are negligible.

Note that the accuracy of the design hypotheses have already been investigated in chapters 4, 5 and 6.

Module and system assembly results will be presented in this chapter. Experimental measurements such as spot profiles at the modulator and detector planes, throughput efficiency and power uniformity are presented. These are useful to characterize the optical performance of the interconnect and diagnose the alignment quality.

7.2 Optical Module Assembly

Recall that the optical system was modularized in order to shift the critical alignment steps away from the system integration phase to the module alignment phase. The optical components were cemented together to give robust, all-glass modules. Various active

alignment techniques were used for assembly. The assembly procedure and results for two of the four modules composing the optical interconnect (BCM and Relay Module) are presented in this section. The remaining modules (Chip Module and OPS) are the subjects of other theses [1][2].

Two interferometric-based alignment techniques were employed to meet the severe lateral and angular specifications: i) one technique uses pairs of low-efficiency diffractive minilenses and gives a theoretical lateral alignment precision in the micron range while the other ii) exploits the fringes produced as a result of a Fabry-Pérot effect between the two uncoated angularly misaligned substrates and achieves an angular precision of up to one wave over the area of the substrate (14mm) or about 0.0035°. Interferometric techniques provide an unsurpassed degree of alignment precision, far ahead of the precision usually attained through visual techniques. For example, a lateral precision of about 20μm can be achieved through visual alignment compared to 6μm or less through interferometric techniques.

The first technique is described in [3]. It uses pairs of extra diffractive minilenses etched around the array of signal minilenses. These minilenses incorporate an etch depth error (they are designed to operate at 632.8nm but are etched at 852nm) to purposely render them inefficient at their design wavelength. This means that a significant undiffracted 0 order is present in the output beam. This 0 order recombines with the +1 order at the second minilens and forms an interference pattern. Misalignments between the two minilenses do not affect the undiffracted 0 order but vary the tilt and radius of curvature

of the +1 order wavefront collimated by the second minilens and thus give rise to interference fringes when the two wavefronts recombine, the number and period of which enable to quantify the misalignments present between the two lenses. Lateral misalignments, for example, result in a tilted collimated output beam because of the displacement of the optical axis of the second minilens with respect to the +1 order and thus produce a set of linear fringes at the output when this beam recombines with the undiffracted 0 order. A longitudinal misalignment results in improper collimation of the +1 order and produces circular fringes. Tilt and roll misalignments result in a combination of circular and linear fringes. Figure 1 is a schematic diagram illustrating the interferometric alignment technique.

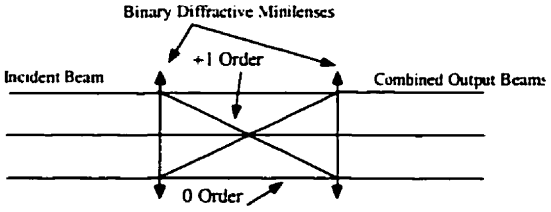

Figure 1. Schematic Diagram of Interferometric Alignment

The interferometric minilenses used in the BCM and Relay Module alignment possess a long focal length (8.5mm) and large apertures: 800μm on the side for the lenses used in the BCM alignment and 2000μm on the side for the lenses used in the Relay module alignment. The BCM minilenses thus possess a slow f-number of f/10.6 while the Relay minilenses possess a relatively fast f-number of f/4.25. This difference made it possible to experimentally test the variation of alignment precision of this technique with respect to f-number.

Wave optics calculations can be performed to calculate the resolution limit of the interferometric minilens technique. The resolution limit is considered to be the amount of misalignment needed in order to produce one fringe over the surface of the minilens. This is the minimum that is considered easily detectable through visual inspection. The derivations relating lateral and longitudinal misalignments to the number of fringes produced can be found in [3]. The number of fringes produced by a lateral misalignment can be calculated with the following equation:

$$N = \frac{D\sin(\tan^{-1}(\frac{\Delta x}{f}))}{\lambda} \qquad \text{Eq. (1)}$$

Where N is the number of fringes, D is the size of the minilens. Δx is the lateral misalignment, f is the focal length and λ is the wavelength of the light. From equation 1, notice that the number of fringes is directly proportional to the size of the minilenses and inversely proportional to the wavelength used.

The lateral resolution is calculated to be 6μm for the BCM minilenses and 2.5μm for the Relay Module minilenses. This is enough to meet the lateral tolerance specifications (see [4]). Calculations indicate that the BCM minilenses have a longitudinal resolution of approximately 600μm while the larger Relay Module minilenses have a resolution of about 100μm. These are rather poor resolutions. Notice that the longitudinal resolution scales much faster than the ratio of minilens diameters. The interferometric minilens alignment technique is not sensitive enough to longitudinal misalignments and cannot be used to meet the very severe tilt tolerance specifications (see [4]) by monitoring the

number of circular fringes present in two or more interferometric minilenses. Therefore, an alternative technique was used for tilt alignment.

Since the substrates are not anti-reflection coated, a beam propagating through them suffers multiple reflections between their respective surfaces giving rise to Fabry-Pérot fringes. Any tilt between the substrates will then result in a set of linear fringes appearing across the area of the substrate since the optical path length within the cavity varies spatially as a function of the tilt. Since the substrates are 14mm square, the theoretical alignment resolution (one wave) using this technique is equal to 0.0035°. This is more than an order of magnitude below the required precision (0.05°).

7.2.1 Beam Combination Module Alignment

The BCM is composed of 5 components: the polarizing beam splitter (PBS), two quarter-wave plates (QWP), an Interface plate and a patterned-mirror grating (PMG). The PBS and QWPs were pre-assembled by the commercial vendor. The PMG and Interface Plate had to be aligned and glued in-house in order to meet severe misalignment tolerances (see [4]). These tolerances are of the order of ten microns laterally and a twentieth of a degree angularly. Visual alignment under a microscope can achieve precisions of about 20μm laterally depending on the kind of alignment markers available, magnification, skill of the operator, etc. This is insufficient. Other methods had to be employed.

This alignment was performed by using the two glass substrates as a transmission Fabry-Pérot etalon and monitoring the number and fringe spacing present on the two substrates. A collimated laser beam was used to produce the fringes and a motorised tilt stage was used to align one of the substrates relative to the other (perfect alignment is obtained when no fringes can be seen on the two substrates).

Two pairs of diffractive interferometric alignment minilenses are present on the PMG and Interface Plate substrates. These were used to align the PMG with respect to the Interface Plate. The setup constructed in order to assemble the BCM is schematically illustrated in figure 2. Alignment of the PMG substrate with respect to the Interface Plate was achieved in four steps:

1) Alignment and gluing of the Interface Plate with respect to the PBS on to the PBS/QWP assembly.
2) Collimation of the beam.
3) Alignment of the beam to be perpendicular to the surface of the Interface Plate
4) Alignment and gluing of the PMG with respect to the Interface Plate onto the PBS/QWP assembly.

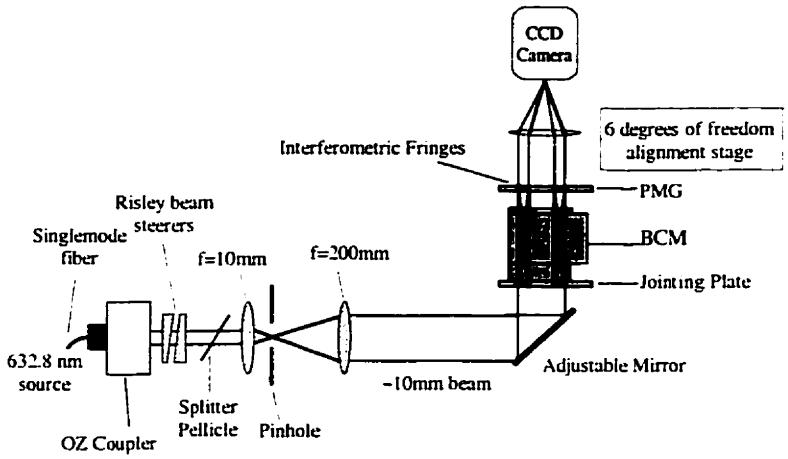

Figure 2. Diagram of the Setup used for BCM Module Assembly

The details of the alignment steps are explained below.

1) The Interface Plate was first visually aligned under a microscope with respect to the sides of the PBS and glued on to the QWP using UV curable adhesive (Norland 61). This operation was difficult due to three problems: 1) The alignment marker on the Interface Plate is separated by 4.75 mm from the PBS, which means that the microscope had to be continually focused back and forth 2) A chamfer was present on the periphery of the PBS which means that the outline of the PBS against which the square metal marker present on the Interface Plate was aligned to was smaller than designed (design value is 7mm but in practice about 6.4-6.5mm) 3) The glue tended to spill over the sides of the QWP when the Interface Plate was brought into contact thus obscuring the periphery of the PBS used as a reference. All these factors decrease the alignment precision.

2) A shear plate was used to collimate the 10mm diameter HeNe beam (632.8nm).

3) A second 1mm diameter pinhole was then placed after the 200mm lens to serve as an aperture and the beam was perpendicularly aligned with respect to the Interface Plate surface by looking at the reflection from the Interface Plate surface through a 250μm pinhole off a splitter pellicle. The reflected spot was centered in the pinhole by varying the orientation of the adjustable mirror. An estimated accuracy of 0.05° could be obtained since the path length from the Interface Plate surface to the pinhole was 30cm. The previous number sets a lower limit on the resolution that can be obtained on the tilt and lateral alignment using the interferometric minilenses since the incident beams need to be perfectly perpendicular to the substrates to produce the correct fringe pattern.

4) A 6 axis positioning system (composed of a Klinger XYZ stage coupled to a Polytec PI tilt and rotation stage) was then used to align the PMG with respect to the Interface Plate by making use of the interferometric fringe information. The PMG was mounted on a custom designed vacuum chuck. The PMG had to be firmly held in place to prevent walkoff from occurring due to the viscosity of the glue during the curing procedure. In general, while the lateral alignment was found to be quite easy to perform using the interferometric minilens technique, the tilt alignment was more difficult: the fringes resulting from the Fabry-Pérot effect between the two substrates could never be totally eliminated and were sometimes found to be slightly curved in shape. This is thought to be due to curvature of the substrate caused by stresses induced by the viscosity of the glue and the vacuum chuck. The resulting tilt correction was not better than approximately 0.03° which is an order of magnitude above the theoretical precision of this technique.

In all and once the procedure was firmly established, the assembly of one BCM required approximately one hour's time, most of this being spent effecting the very fine alignments required. Figures 3 and 4 are two CCD camera images taken during the assembly of a BCM.

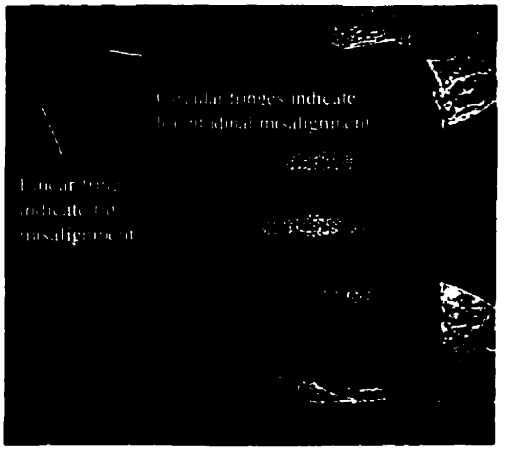

Figure 3. BCM showing Longitudinal and Tilt Misalignments

The fringes in figure 3 shows the PMG to be:

1) Laterally aligned since there are no linear fringes present in the aperture of the minilenses. The lateral alignment precision is estimated to be better than 6μm.
2) Tilted with respect to the Interface Plate as witnessed by the linear fringes present outside the apertures of the interferometric minilenses and resulting from the Fabry-Pérot effect between the two substrates.
3) Longitudinally misaligned as about one circular fringe is present in each minilens indicating that the two substrates are misaligned by about 600μm from their nominal longitudinal position.

Figure 4 shows that the tilt misalignment has been largely corrected (notice that only about 5 long period fringes are present outside the minilens aperture, which translates into about 0.03° of tilt). The PMG is ready to be moved down and glued on to the QWP. The 5μm lateral and 0.03° angular alignment precision meet the misalignment tolerance budget of 32μm laterally and 0.05° angularly.

Figure 4. BCM showing Final Alignment

A completed BCM module is shown in figure 5 below.

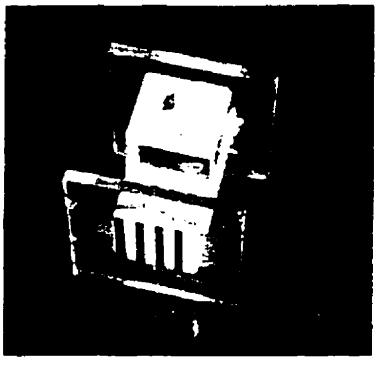

Figure 5. Assembled BCM (scale in mm).

Notice the compactness of the module.

7.2.2 Relay Module Alignment

The Relay Module was assembled following the same four-step procedure as used with the BCM. The first minilens array was visually aligned to a corner of the optical spacer and glued. Much the same problems were encountered in this first step as during the BCM assembly (presence of a chamfer, spatial separation of the alignment references). The alignment precision is estimated to be about 20μm. Figures 6 and 7 show pictures taken during the Relay Module alignment process. The rest of the alignment process was much more straightforward in this case as the tilt of the minilens arrays did not have to be tightly controlled and was fixed by the parallelism of the supporting block of glass (0.05°). Once again, the interferometric alignment technique was found to be simple and effective in meeting the required alignment precision. Figure 6 shows a relatively large number of fringes (12) to be present in the minilens aperture. The fringe curvature indicates that some longitudinal misalignment is present. The lateral misalignment is estimated to be 30μm.

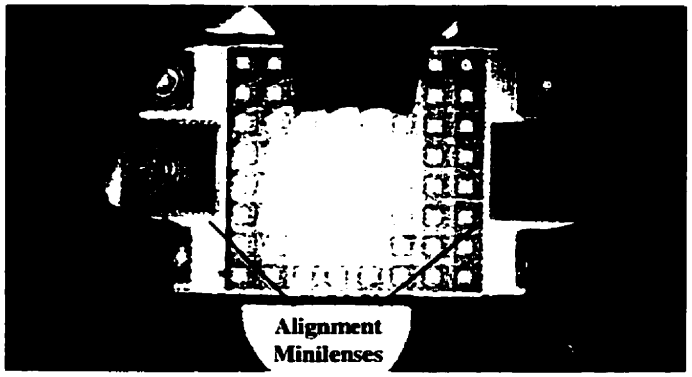

Figure 6. Interference Fringes observed during Relay Assembly showing Lateral and Longitudinal Misalignment.

Figure 7 shows the final alignment. It is difficult to clearly distinguish circular or linear fringes within the minilens aperture. The lateral misalignment is estimated to be less than 2.5μm. The remaining fringe pattern may be the result of thickness or refractive index variations in the glue used to bond the minilens array to the optical spacer.

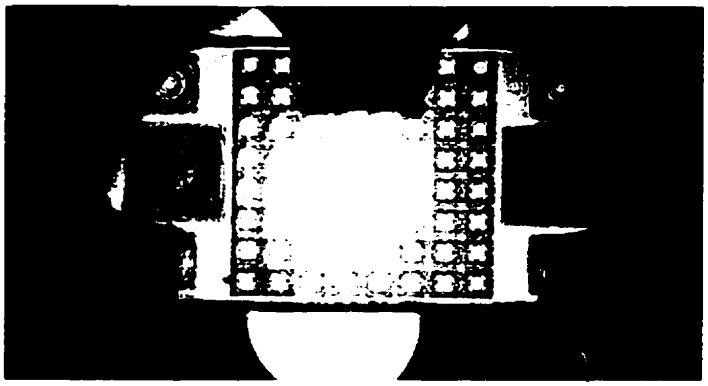

Figure 7. Final Alignment.

Figure 8 is a picture of the assembled Relay Module.

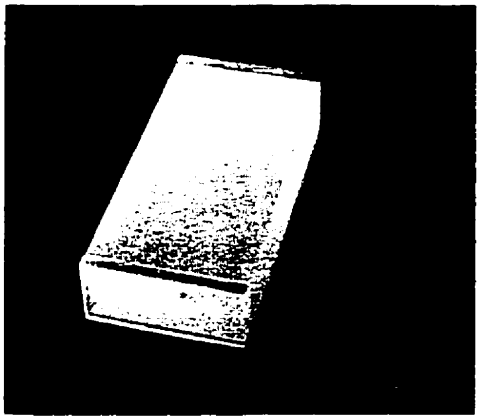

Figure 8. Assembled Relay Module (scale in mm).

7.2.3 Module Assembly Summary

The interferometric minilens alignment technique was found to be a simple and effective method to meet the severe lateral alignment specifications. The lateral alignment resolution of this technique is directly proportional to the minilens aperture size. An 2000μm aperture was found to provide greater alignment precision than an 800μm aperture. However, the minilens footprint on the diffractive optical element (DOE) increases proportionally to the square of the aperture size. Thus the cost of the minilens probably increases more rapidly than its resolution. This limits the minilens aperture size. Also, the maximum aperture size is dependent on the f-number of the minilenses. F-numbers faster than f/2.3 will not be supported by the binary diffractive fabrication technology [5].

The interferometric technique does not provide tilt alignment. This alignment has to be performed by monitoring the fringes present on the substrates due to Fabry-Pérot effects. This technique is extremely sensitive as it possesses a resolution of one wave over the

area of the substrates. A disadvantage is that the contrast between the fringes is low due to the low reflectivity of the substrates (4%). Alignment is thus slightly more delicate as it is more difficult to identify the fringes on the substrate. Increasing the reflectivity of the substrates is not desirable as it will induce greater optical losses. The interferometric minilens alignment technique could be used for tilt alignment on the condition that a mirror is deposited on one of the substrates and the interferometer is used in reflective mode [3]. This would then provide the precision necessary to meet the tilt alignment tolerances.

7.3 System Assembly

Once the modules are assembled, they must be integrated into the baseplate to construct the optical system. Alignment must be monitored to guarantee that a maximum of the optical power emitted by the source falls on the appropriate detector. However, the experimental data that can be collected is often limited due to the difficulty of performing the measurements. The main problem is often simply a question of space constraints: the necessary viewing ports cannot be accessed easily. For example:

1) The optoelectronic chips prevent direct access to the beams at the optoelectronic chip plane. This means that alignment and beam quality cannot be monitored at this critical plane.
2) The system is very compact (~5cm on the side). This means that an instrument such as a power meter or CCD camera is too bulky to position within the optical layer.

Ways have to be found to circumvent these problems. In particular, it is crucial to be able to image the optoelectronic chip plane to insure that the focused spots actually fall on the modulators and detectors. Diagnostic and testing thus constitutes a critical part of the design of an optical interconnect. Various diagnostic tools must be planned and incorporated in the system design.

7.3.1 Diagnostic Modules

One way to overcome the first problem outlined above is to render the optoelectronic chip transparent so that "through-the-chip" imaging can be performed to monitor the spot alignment at the detector plane. A Chip Diagnostic Module (CDM) combining a minilens array with a transparent substrate containing alignment markers was constructed for this purpose.

The second problem can be alleviated by inserting mirrors in the baseplate to allow imaging to be performed perpendicularly to the optical layer. A Relay Diagnostic Module (RDM) was constructed to perform this function.

In this way, the system can be assembled and its alignment monitored without inserting the optoelectronic chips. Together these two modules can monitor the angular and lateral position of the beams at the optoelectronic chip and within the baseplate. They can then be removed when alignment is satisfactory and replaced by the appropriate optical modules.

The RDM is shown in figure 9. It is designed to substitute a Relay Module within the baseplate in order to diagnose the beam position and angle at the Relay Module position. The module is composed of a minilens array and of a patterned photomask reproducing the features of the optoelectronic chip. A beam splitter is added between the minilens and the photomask to act as a mechanical support. Note that there is no special reason to use a beam splitter; it was used merely because it is a cube of high quality optical glass of the appropriate dimensions and was readily available. A prism is glued at the back of the photomask in order to provide a viewing port so that the photomask surface can be imaged. The minilens array and the photomask are visually aligned relative to each other by monitoring the position of the focused spots on the photomask surface. The alignment precision of the photomask relative to the minilens array is estimated to be 10μm.

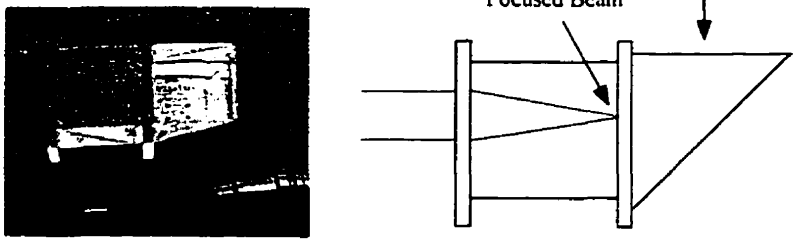

Figure 9. Relay Diagnostic Module

An angular misalignment of the beams in the interconnect is recognised as a lateral displacement of the spots with respect to the detectors outlined in chrome at the surface of the photomask. A lateral misalignment of the beams with respect to the optical axis will not displace the spots laterally on the photomask targets but will be evident when looking at the position of the beams within the aperture of the RDM minilenses. This is illustrated in figure 10.

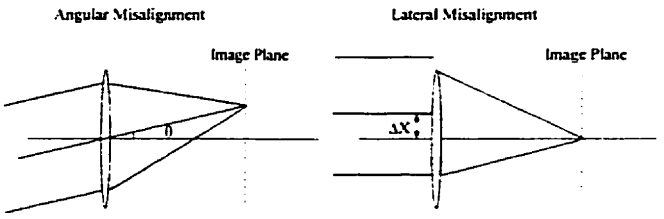

Figure 10. Effect of Angular and Lateral Misalignments at the Image Plane of a Minilens.

Note that the lateral misalignment at the image plane is a function of the tangent of the angular misalignment of the beam at the minilens times the focal length of the lens. The longer the focal length, the greater the effect of angular misalignment. This is a fundamental tradeoff when designing optical interconnects. Longer focal lengths decrease the effect of longitudinal misalignments but increase the effects of angular misalignments.

The CDM is shown in figure 11. The CDM is a replica of the Chip Module except that a transparent photomask replaces the optoelectronic chip. The photomask possesses thin chrome patterns mimicking detectors and modulators. An opening is present at the back of the module for imaging purposes. The CDM makes it easy to visualize where the optical signal arrives by imaging the photomask with the help of a CCD camera. If a misalignment is present, adjustments can be performed by using the Risley prisms or the Corner Prism before the actual optoelectronic chip is inserted in the system. This module can also be used to evaluate other system performance metrics such as beam profile and power distribution.

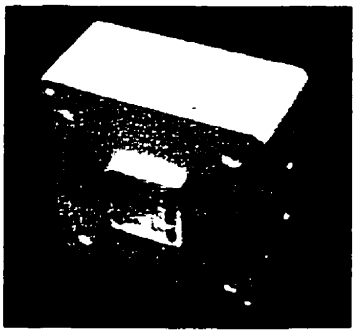

Figure 11. Chip Diagnostic Module.

Several "flavors"of CDMs i.e. using different photomasks were produced in order to perform a variety of functions:

1) Image through the substrate to monitor the alignment of the spots with respect to the detectors or modulators. Thin lines of chrome outline the structure of the detectors and modulators on the photomask. The CDM is mostly "transparent" in this case.
2) Reflect the beams impinging on the modulators in order to direct them to the next BCM. The modulator targets are then filled with chrome. The CDM is mostly "opaque" i.e. reflective in this case.

Figures 12 and 13 are pictures of the focused spots imaged through a "transparent" and "opaque" CDM.

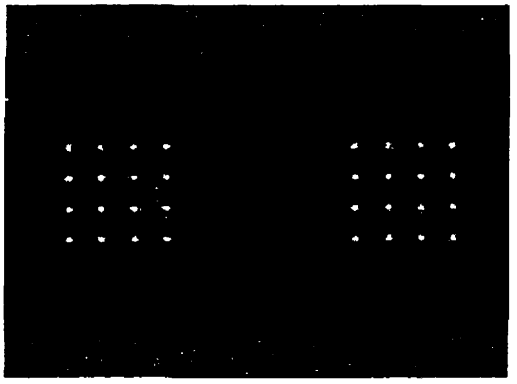

Figure 12. Picture of Clusters Imaged through CDM.

Figure 12 shows the spots imaged through openings in the chrome pattern of the photomask that mimic the outline of the detectors on the actual optoelectronic chip.

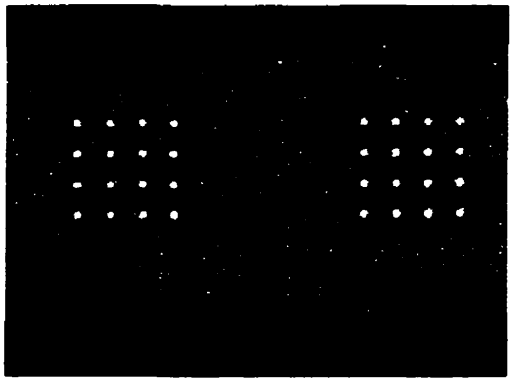

Figure 13. Picture of Spots Imaged through CDM.

Figure 13 shows the purposely misaligned spots imaged through a CDM containing circular targets filled with chrome that mimic the modulators on the actual optoelectronic chip.

7.3.2 System Alignment

The demonstrator system presented here seeks to demonstrate a series of optomechanical goals related to passive alignment, repeatability and stability. Were these goals achieved?

System alignment was found to be more complicated than originally planned. One stage (two BCMs) was assembled in a purely passive manner and alignment was monitored using the diagnostic modules. The focused spots at the detector plane of the second BCM were misaligned by more than 100μm and were severely clipped causing fringing to appear in the spots.

Passive strategies failed to provide satisfactory alignment. The first goal of this demonstrator (passive alignment) was therefore not achieved. Note that the Risley prisms cannot be used to correct such a large misalignment. However, the alignment proved remarkably stable. No drift in the spot position could be observed in the course of several days.

In order to permit system assembly, active alignment strategies had to be employed. This meant varying the position of the modules through the use of pads to bring them into alignment.

It was decided to dimensionally characterize the BCM module in order to try and identify the source of the misalignment. Such a characterization is useful to help determine if

fabrication errors are present and to determine where and how much compensation is required to obtain alignment. The BCM possesses the most stringent alignment tolerances in this system (see [2]). Small fabrication errors might thus indicate large deviations in the optical beams.

A high magnification microscope combined with a precision XY translation stage was used to measure various coordinates on the BCM. These coordinates were then used to calculate the error on the angular value of the PBS reflecting plane (this should be 45°) as well as the lateral displacement of that plane with respect to the system optical axis (ideally, the system optical axis should pass through the center of the PBS reflecting plane). The angular error is caused by fabrication errors while the lateral error is due to a combination of fabrication errors and alignment errors when glueing the PMG onto the PBS/QWP assembly. Note that the effect of angular errors will be to induce lateral misalignments at the modulator/detector plane while the effect of lateral errors will be to shift the beam laterally with respect to the nominal optical axis of the system causing clipping at each minilens.

The following table lists the measured values for the four BCMs used in the backplane demonstrator system.

Table 1. Characterization Results for BCM Reflecting Plane.

BCM Number	Angular Error (Degrees)	Lateral Error (μm)
1	0.055	124
2	0.094	51
3	0.114	90
4	0.940	84

It can be seen that there is a wide variation in angular (from 0.055° to 0.94°) and lateral (from 51μm to 124μm) errors across the BCMs. It was decided to compensate for lateral and angular errors by placing pads of the appropriate thickness at the contact points between the BCM and the baseplate in order to modify the tilt and height of the module.

The alignment procedure outlined in chapter 3 needed to be modified and active alignment measures introduced in order to overcome these alignment difficulties. This was done and all four stages of the ring were assembled. Three to four days were necessary to align each stage once the alignment procedure was firmly established. Alignment was then deemed satisfactory for all the stages except the final one. The spots could not be brought on to the detectors at the last stage. This is thought to be due to the accumulation of errors across the four stages of the ring which lead to a progressive elevation of the optical axis with respect to the mechanical axis of the baseplate.

The following conclusions were arrived at in the course of assembling this system :

1) Passive assembly techniques did not guarantee alignment. Active alignment techniques had to be used in the system integration phase.

2) The optical module placement was repeatable to within, or better, than the allowed tolerances.

3) The system alignment was stable (in a laboratory environment). Once aligned, the system alignment did not drift in any measurable fashion.

The alignment procedure outlined in chapter 3 was modified. The revised version is substantially more complex than the original.

Revised Alignment Procedure

1) Place and align the first BCM within its kinematic mount. Place and screw in the brass clamp around the BCM to secure it in place.

2) Position the Chip Diagnostic Module and evaluate the spot alignment on the modulators of the first BCM. If an angular error is present (this shows up as a translation of the spots on the image plane of the CDM), the Risley prisms present in the OPS can be rotated to position the spots on the modulators. If a lateral error is present (this shows up as a lateral misalignment of the beams on the surface of the CDM minilens array), the tilt plates present in the OPS can be rotated to displace the beams laterally on the surface of the minilens.

3) Position the Corner Prism.

4) Place the Relay Module into position.

5) Place and align the second BCM within its kinematic mount. Place and screw in the brass clamp around the BCM to secure it in place.

6) Monitor alignment with the Chip Diagnostic Module. If a minor angular error is present (less than 0.633°), this can be corrected by adjusting the Risley prisms present in the interconnect. If the angular error is too large, it is necessary to tilt the second BCM in order to direct the spots onto the detectors. If a lateral alignment error is present on the CDM minilenses then it will be necessary to either vary the height of the Corner Prism or the height of the first BCM to properly position the beams in the Chip Diagnostic Module minilenses. The Relay Module must then be realigned with respect to the beams travelling in the interconnect so that they are not clipped. This can be done by placing pads between the Relay /baseplate rods contact points to vary the lateral position of the Relay Module.

Looking at the revised alignment procedure, it can be seen that aligning one stage (two BCMs) involves considerable work. The optical modules must be actively aligned with the use of pads to modify their positioning within the baseplate. Analytical relationships were derived to calculate the pad thickness required to achieve a desired displacement of the spots on the Modulator/Detector plane. System assembly thus becomes a labour intensive procedure comprising many delicate and time consuming alignment steps. Below are a few photographs of the assembled system.

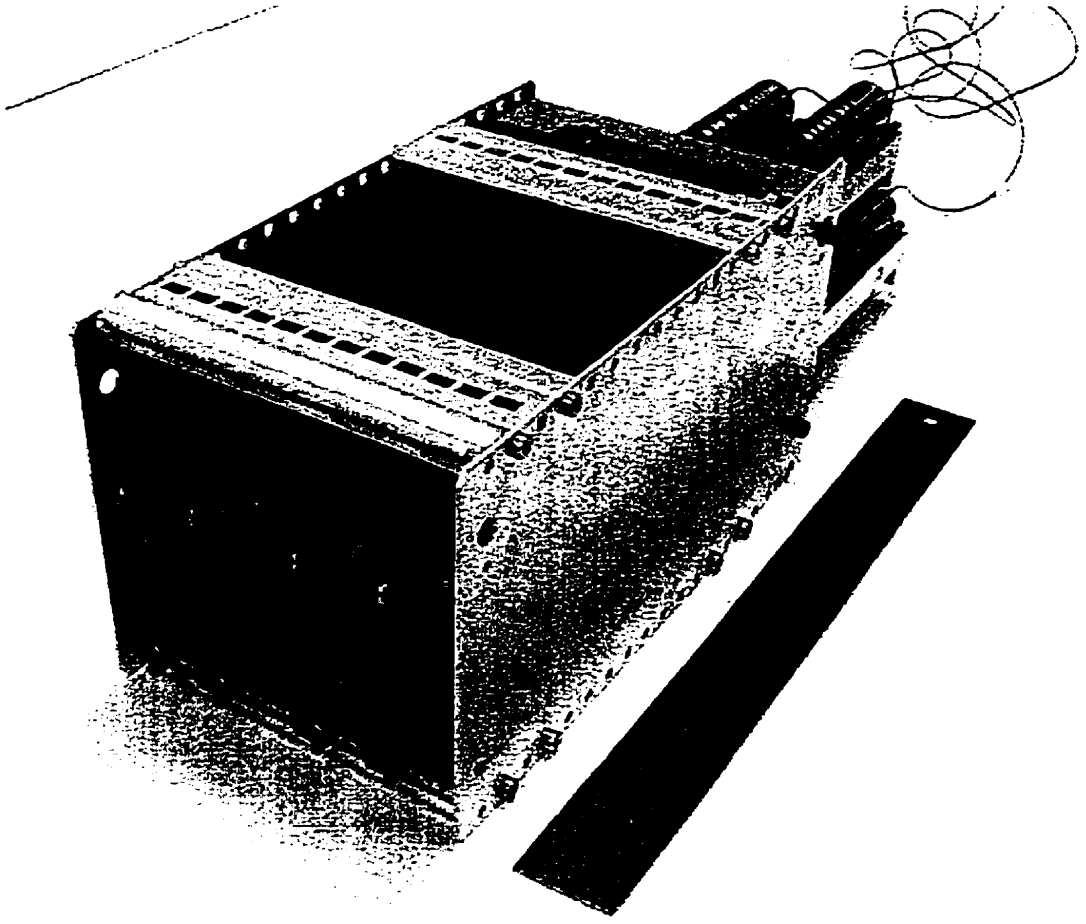

Figure 14. Assembled System with Boards.

Picture 14 shows the system packaged in an industry standard 3U chassis (13.97cm wide and 37.465cm deep) complete with electronic boards.

The following picture shows the optics and optomechanics. A CDM has been removed to show the optical components underneath.

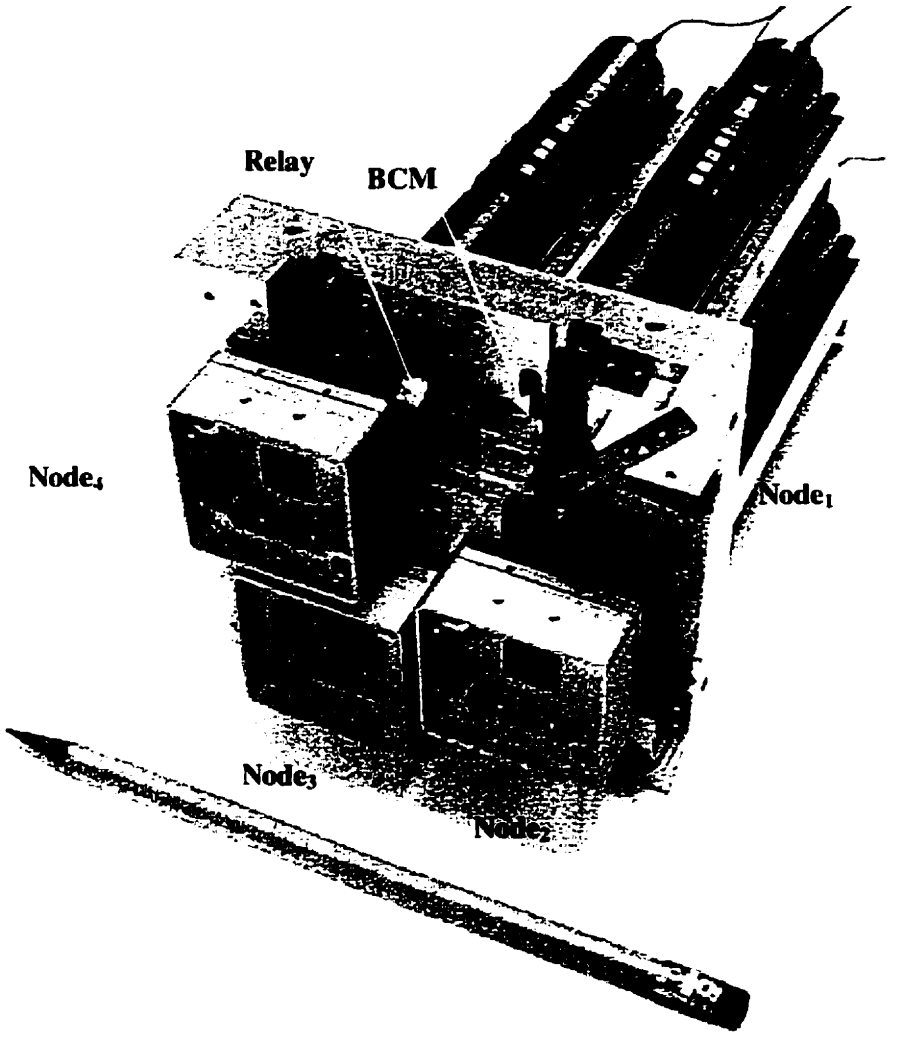

Figure 15. Assembled System.

Each node in the system is numbered from 1 to 4 in a clockwise fashion starting from the upper-right corner. Note the compactness of the system.

The following picture is a close-up of the optical layer.

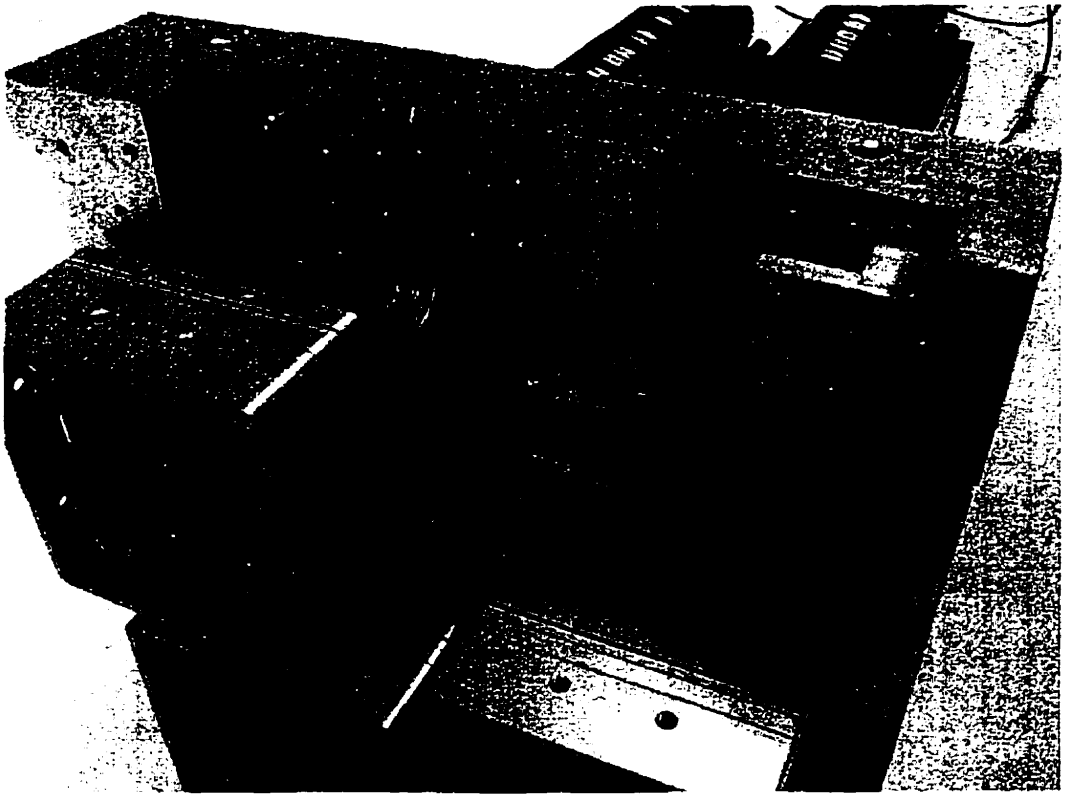

Figure 16. Close-Up of Assembled System.

The various modules composing the interconnect can be seen. Notice the brass clamps that hold the modules in place.

7.3.3 Characterization Results

Optical characterization results are useful to quantify the performance of the interconnect and the degree of alignment. The spots falling on the appropriate detector does not guarantee that alignment is perfect. Some degree of misalignment might still be present which is not detectable visually. Measurements such as throughput and uniformity are useful to verify this.

7.3.3.1 Optical System Power Throughput

The power throughput efficiency between the modulators at $node_2$ and the detectors at $node_3$ was measured. A 95% reflective mirror was placed at the modulator plane and only a minilens array was placed in front of the detector plane. This was done in order to eliminate possible cavity effects in the uncoated photomask fused silica substrate. The throughput efficiency from modulator to detector was measured to be equal to 23% ±2% (-6.4 dB). This is quite good considering the number of interfaces (38) and minilenses (6) that the beam has to traverse when going from the modulator plane to the detector plane. The diffractive minilenses possess eight phase levels giving them a theoretical diffraction efficiency of 95%. The real diffraction efficiency is lower considering Fresnel losses (90%). The beam must go through six minilenses before reaching the detectors (0.9^4 = 65%). The optical components are composed of various types of glass having different indices of refraction. For example, the PBS is made of SF56A having an index of 1.76 at 852nm while the diffractive components are made of fused silica having an index of 1.48 at 852nm. The UV curable glue used to assemble the modules (Norland 61, index of 1.548 at 852nm) does not perfectly index match to all these surfaces. The loss suffered by the beam when going from the PBS to the QWP is calculated to be equal to 1.5%.

Considering all these sources of loss, the predicted theoretical throughput should lie between 21% and 36% (see the power budget calculated in [2]). Note that this theoretical value does not include power losses due to clipping or misalignment. The experimentally

measured value is within that range. This means that clipping does not contribute significantly to power losses. The system is well aligned.

7.3.3.2 Spot Quality.

Spot quality is the degree to which the measured spot profile corresponds to the theoretical profile. It constitutes another way to verify both the imaging quality of the optical system and the degree of clipping which the beams suffer upon propagation through the system. Deviations from a Gaussian spot profile indicate that aberrations or clipping are present. In particular, the presence of fringes in the spots would be a sign that optical power is being guided by multiple minilenses and recombining at the image plane. This would clearly be undesirable.

Figure 17 shows a CCD picture of the array of 1024 spots at node$_3$. The columns coming in from node$_2$ are interlaced with the columns produced by the OPS Module attached to node$_3$. The first column contains the spots generated by the second OPS Module.

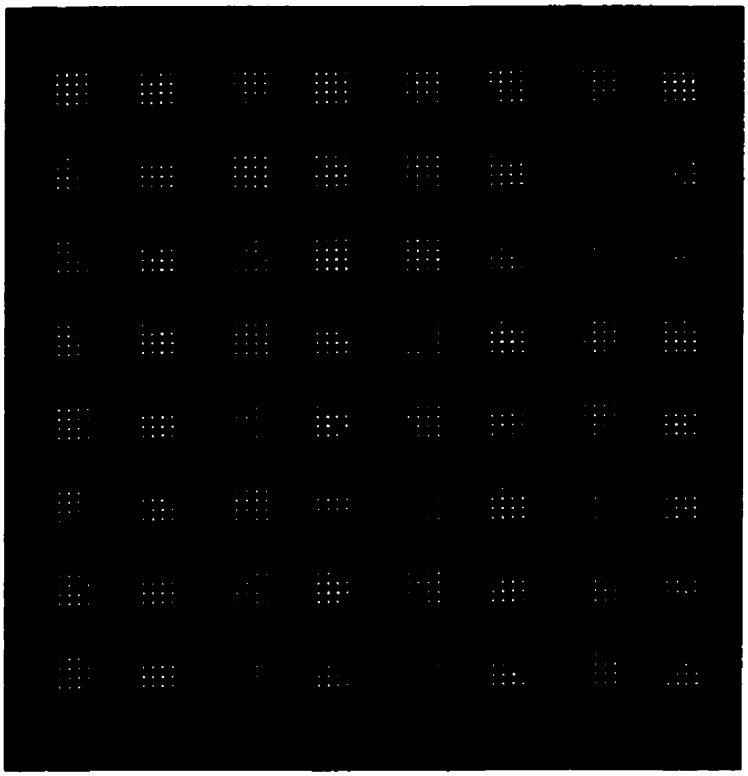

Figure 17. 1024 Spots at Node$_3$.

Notice that the columns of clusters coming from the previous stage are indistinguishable from the ones produced by the second OPS in this low-resolution CCD image.

A 10x microscope objective (Alessi) mounted on a CCD camera (Hitachi) was used to image clusters at the modulator and detector planes. The automatic gain control was disabled and the camera was verified to respond linearly to variations of input power. Figure 18 shows an image of a 4x4 cluster at the modulator plane.

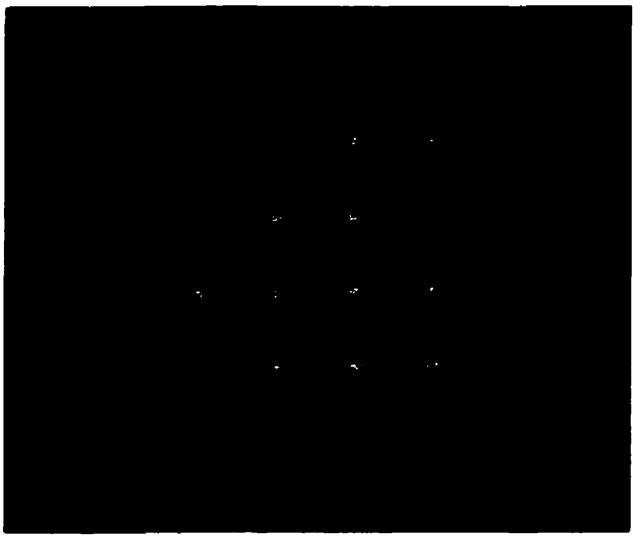

Figure 18. Modulator Cluster.

The power distribution in the cluster present at the modulator appears to be quite uniform. Note that the spots appear to be of good quality. No fringing can be discerned. Figure 19 shows a picture of the same cluster at the detector plane.

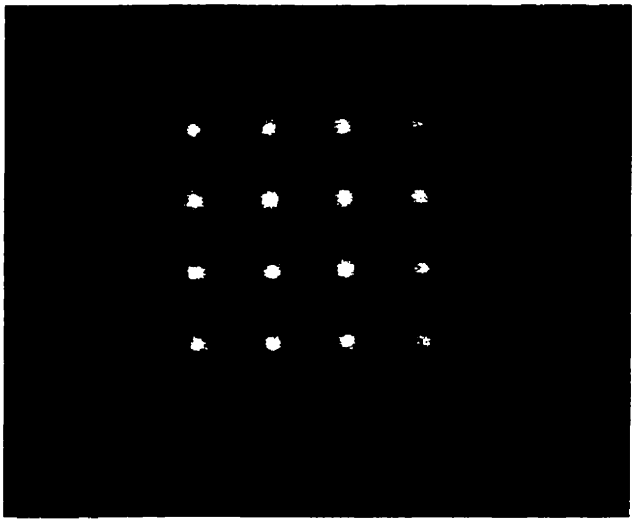

Figure 19. Detector Cluster.

Note that the central spots appear to be slightly more intense than the outermost spots of the 4x4 array.

Figure 20 below shows the result of a multiple Gaussian fit performed on the first column of the 4x4 cluster at the modulator plane. The maximum peak intensity varies by about 15% across the row and the spots can be seen to closely follow a Gaussian. Notice the excellent fit to a Gaussian profile and the absence of fringes. Spot quality at the modulator plane is excellent.

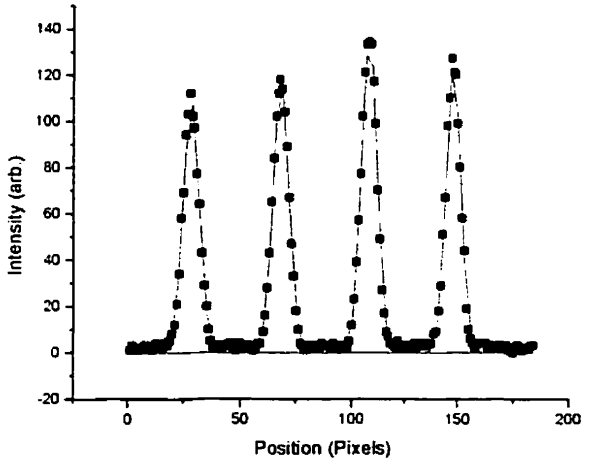

Figure 20. Multiple Gaussian Fit of Spots at Modulator Plane.

The spot size at the modulator plane can be calculated from the multiple Gaussian fit performed in figure 20. The standard deviation of each Gaussian provided by the curve fitting routine of the commercial software used [6] corresponds to the Gaussian beam radius ω_0. The targets on the CDM are of a known size. An image can therefore be taken with the 10X Alessi objective and used to calibrate the CCD. The calibration constant (μm per pixel) can then be used to calculate the Gaussian beam radius in microns. This was done for the spots at the modulator plane. A mean beam radius of 14.1μm ±1.5μm was obtained. This is larger than the theoretical value of 13.1μm. This would seem to indicate that the system is slightly non-telecentric or that the OPS does not produce the

required input beam characteristics. The measured value is also larger than the calculated tolerance (13.1 ±0.3μm). However, note that the uncertainty on the measured value is larger than the discrepancy with the theoretical value.

Figure 21 below shows the result of a multiple Gaussian fit performed on the first column of the 4x4 cluster at the detector plane. The maximum peak intensity varies by approximately 20% across the column. The spots can be seen to closely follow a Gaussian. Spot quality at the detector plane is excellent. A more accurate measurement of power uniformity will be presented in section 7.3.3.3.

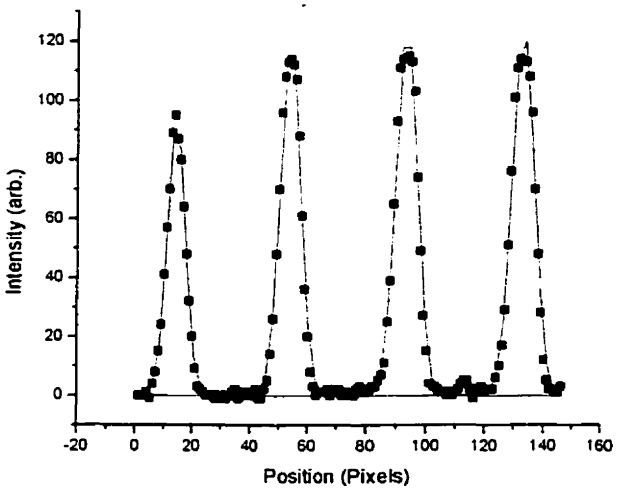

Figure 21. Multiple Gaussian Fit of Spots at Detector Plane.

The beam radius at the detector plane was calculated to possess an average value equal to 13.7μm ±1.5μm. This is again larger than the theoretical value and slightly smaller than the value measured at the modulator plane. This would seem to indicate that a slight asymmetry is present in the interconnect (if the interconnect were perfectly telecentric,

the modulator and detector beam radius would be identical). This is thought to be due to optical path increases induced by uncontrolled glue thicknesses used to assemble the BCM and Relay modules. Simulations indicate that a 200μm increase in the optical path length traveled by the beams through the Relay module is sufficient to produce a 13.7μm spot size on the detectors. A small 250μm longitudinal shift in the placement of the OPS minilens array is sufficient to produce 14.1μm spots on the modulators.

Since the adhesive used to assemble the Relay was Norland 61 UV curable glue (n=1.548 at 852nm), then only 161.5μm microns of glue are necessary to induce a 250μm optical path length difference. This would mean that an 80μm layer of glue would have had to be used to glue the two diffractive minilens arrays on each side of the supporting block of glass. While this does constitute a rather thick layer of glue, let us also note that optical components are specified to ±50μm dimensionally (this includes the substrates on which the DOEs are etched) which could also have contributed to optical path length variations.

In conclusion, the slightly larger than designed spot sizes at the modulator and detector planes are not surprising and are not critical because the interconnect is an f/11 system where the beams increase in diameter slowly over hundreds of microns (the Rayleigh range is 633μm). The focused spots are still accommodated by the oversized modulators (50μm) and detectors (70μm).

While a CCD picture is a good way to estimate spot quality, more quantitative measurements are needed to measure the power distribution uniformity within the cluster.

7.3.3.3 Array Uniformity

A good method to perform uniformity measurements is the "scanning pinhole" method, which consists in scanning a pinhole across a grid and recording the power passing through the pinhole at each grid point. A plot of power versus position can then be obtained. This method is quite accurate provided that the pinhole is small enough compared to the size of the beams under measurement and that the laser source has a stable power output. In this case, the SDL external cavity tunable laser source that was used has a power stability of 0.1%. A 5μm pinhole was used to scan the 40μm spots. The scanning was done on a 5x5μm square grid to eliminate convolution effects between successive readings. The large grid size used meant that each scan lasted several hours.

Note that uniformity constitutes a particularly critical measurement in this system as a dual-rail encoding scheme is used. Each bit is encoded in the power difference between two optical beams. There must therefore be enough power difference between the two channels for the receivers to switch. Any non-uniformity will degrade the power difference and affect the ability of the receivers to switch.

Figure 22 shown below presents a power versus pixel position map for one of the clusters present at the modulator plane.

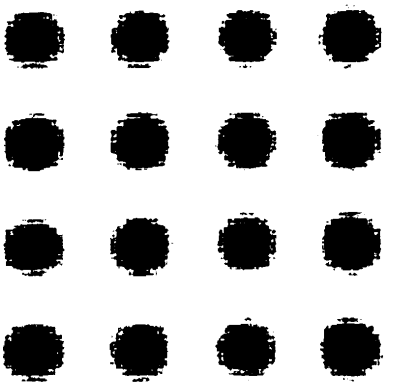

Figure 22. Map of Power Measurements at Modulator Plane.

Figure 23 tabulates the total relative power present in each spot at the modulator plane. A 3D chart helps to visualize the power uniformity in the cluster.

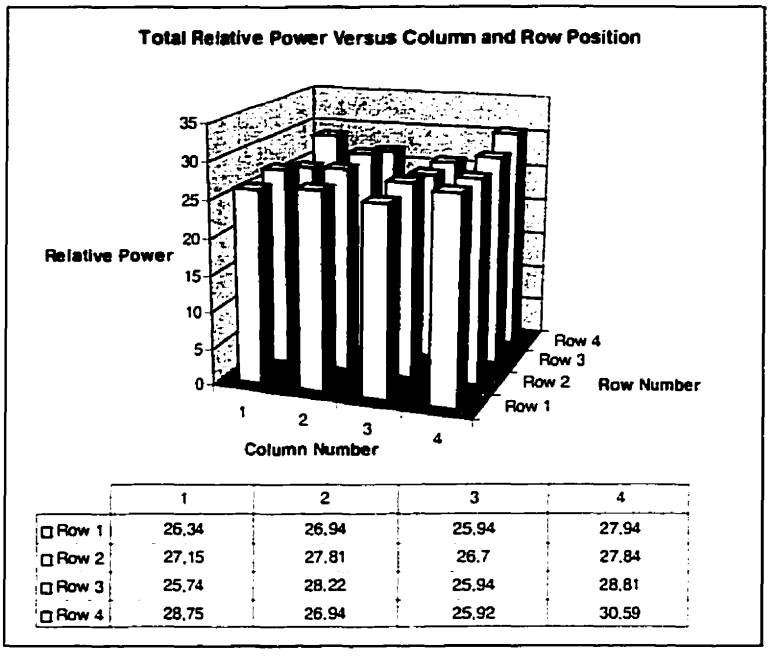

	1	2	3	4
Row 1	26.34	26.94	25.94	27.94
Row 2	27.15	27.81	26.7	27.84
Row 3	25.74	28.22	25.94	28.81
Row 4	28.75	26.94	25.92	30.59

Figure 23. Total Relative Power versus Spot Column and Row Position at Modulator Plane.

The average value in the cluster is 27.23. The standard deviation is one way to characterize the "spread" in values in the data assuming that it has a normal distribution. In this case, the standard deviation is equal to 5.07%. However, since a dual encoding scheme is used, perhaps a more accurate way to characterize the uniformity is to look at the maximum power difference between pairs of spots. Here, the maximum power difference takes place between the two bottom left spots which possess relative powers of 25.74 and 28.75 respectively. This is an approximately 10% power difference. The rest of the spots are nearly identical in power. Uniformity is therefore quite good.

Figure 24 shows a map of power versus pixel position for the same cluster after it has traveled through the interconnect up to the detector plane. The central spots appear to be

stronger in intensity than the peripheral spots which points to a decrease in uniformity compared to the spots at the modulator plane

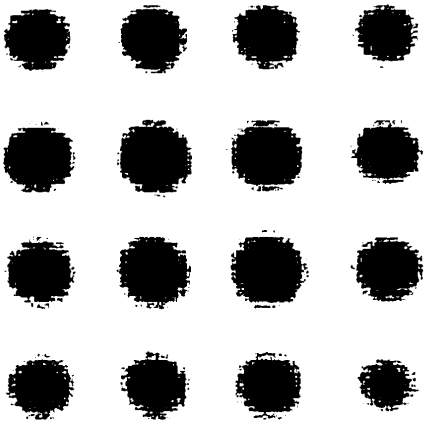

Figure 24. Map of Power Measurements at Detector Plane.

Figure 25 tabulates the total relative power present in each spot at the modulator plane. A 3D chart helps visualize the power uniformity in the cluster.

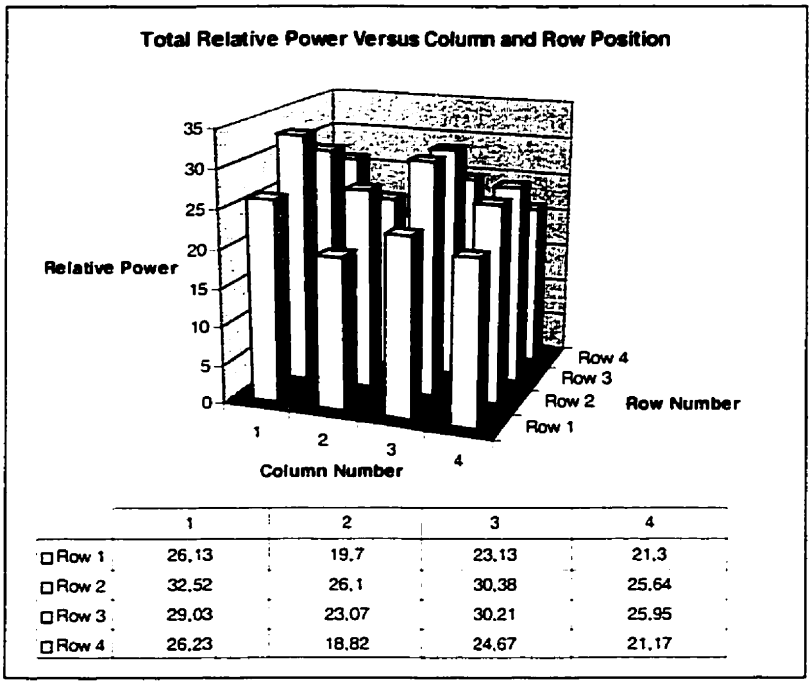

	1	2	3	4
Row 1	26.13	19.7	23.13	21.3
Row 2	32.52	26.1	30.38	25.64
Row 3	29.03	23.07	30.21	25.95
Row 4	26.23	18.82	24.67	21.17

Figure 25. Total Relative Power versus Spot Column and Row Position at Modulator Plane.

The average power value is equal to 25.25 and the standard deviation is equal to 31%. This is a 5.7 times increase over the standard deviation calculated at the modulator plane. The two pairs of center top spots possess a power difference of about 30% while the bottom left spots differ by only 10%. The average power difference between pairs of spots is about 20%. This is a significant increase over what was seen at the modulator plane. The 4x4 cluster at the detector plane is significantly less uniform than the 4x4 cluster at the modulator plane.

This decrease in uniformity as the beams travel through the optical system can be attributed to fabrication errors in the diffractive minilens arrays used for focusing and

collimation properties. The minilenses possess eight phase levels. Fabricating such a diffractive minilens requires the use of three masks to define the patterns that will be etched in the fused silica. Any misalignment between these masks combined with possible mask fabrication defects leads to inaccurate fabrication of the fine features located at the edges of each minilens [7]. The result will be a decrease in the diffraction efficiency at the edges which induces non-uniformities in the intensity of beams propagating through the minilens. This is precisely what is observed at the detector plane.

The effect of non-uniformity is to introduce a power difference "floor" that is to be respected if the system is to function properly (i.e. if the receivers are to switch). Dual-rail receivers are known to be quite tolerant to variations of input optical power (receivers have been demonstrated having common-mode dynamic ranges of 16dB at 622Mb/s) however, the tolerance to variations of the relative power between the two beams encoding the data is much lower. There is little data available on this topic in the literature however, one reference [8] quotes a 3dB variation as being the tolerance limit at 622Mb/s for transimpedance type receivers. While applying this data to our system directly is slightly dubious as we do not use the same receiver circuits, it can nonetheless be used as a guideline. This would then mean that a 50% differential power variation is the maximum that can be tolerated if the system is still to function properly. A 20% differential power decrease due to non-uniformity should therefore be tolerable.

7.3.3.4 Image Mapping

The image mapping properties of the interconnect described in chapter 3 were verified experimentally. The letter "J" was patterned in filled circular chrome targets of a modulator cluster on a photomask. The photomask was used to reflect the spots at $Node_2$. Pictures were taken at $Node_2$ and $Node_3$ and compared to verify that they match figure 16 of chapter 3. The position of the reflected cluster in the 4x8 matrix was found to correspond to a mirroring of the matrix as shown in figure 15 of chapter 3.

Figure 26 shows a picture taken at $Node_2$. The "J" patterned in filled circular chrome targets can be distinctly seen.

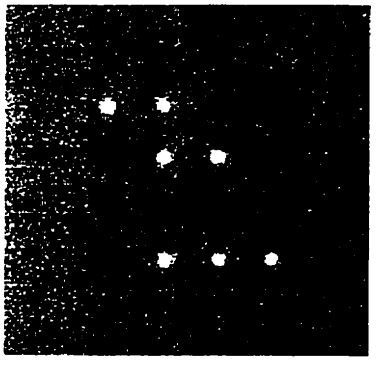

Figure 26. Cluster at $Node_2$ showing the Patterned "J".

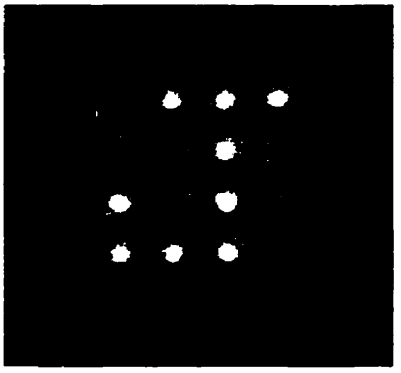

Figure 27. Cluster at Node$_3$ showing the "J".

It can be concluded from figures 26 and 27 that the cluster-level image mapping corresponds to that predicted in chapter 3.

7.3.4. Discussion of Alignment Results

The difficulties encountered during the alignment of this system can largely be ascribed to improper fabrication tolerances on the polarizing beam splitter (PBS) cube that constitutes the heart of the beam combination module. In particular:

1) The presence of chamfers on the PBS perturbs the alignment of the diffractive components (the patterned-mirror grating and Interface Plate) that are glued on to the PBS/QWP assembly to constitute the BCM. Highly polished optical components possess extremely sharp edges. These edges are polished away to prevent injury giving rise to chamfers. As the PMG is used as an alignment reference in the baseplate, then any misalignment of the PMG with respect to the PBS will displace the beams perpendicularly to the mechanical axis of the system.
2) Departures from 45° in the angle of the reflecting plane of the PBS cause a tilt to be introduced in the beams exiting the BCM.

7.3.4.1 Effect of Chamfers

Figure 28 below is a picture of the bottom left corner of a typical PBS/QWP assembly. A schematic diagram of a chamfered PBS is also included to illustrate the effect that the presence of chamfers has on the PBS geometry. Note that large chamfers are present on the sides of the polarizing beam splitter. The left-side chamfer is approximately 500μm wide while the bottom chamfer is approximately 400μm. In contrast, the right side chamfer (not shown here) is only about 50μm. In general, the chamfers present on the PBSs are either quite large (between 350 and 500μm in width) or rather narrow (50μm).

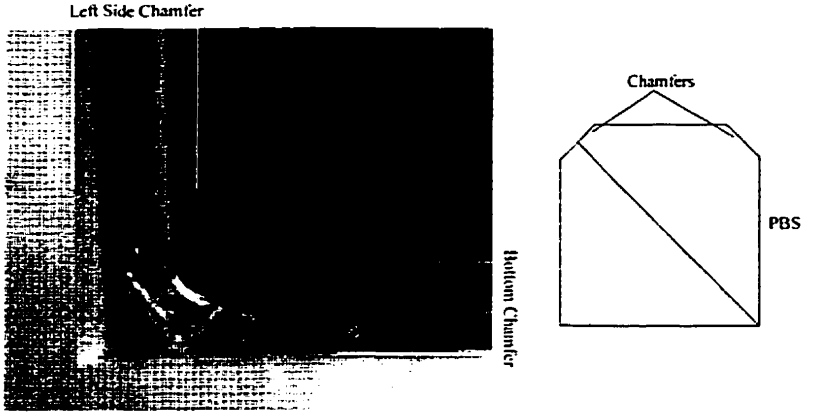

Figure 28. Chamfers Present on a PBS.

Note that the PBS is specified to be 7.0 ±0.1mm on the side. The optical beams occupy a 6.4mm on the side square area. If the PMG is perfectly centered within the PBS, then this means that only 300μm extra room is available on each side of the beams to accommodate for possible misalignments. The presence of substantial chamfers at the sides of the PBS mean that part of the beams might be blocked or refracted and will not arrive at the modulator or detector plane.

Furthermore, the presence of chamfers causes problems when gluing the Interface Plate on to the PBS/QWP assembly. The reference frame on the PBS (that is, the topmost surface) is then no longer a 7mm on the side square that neatly fits within the 7mm metal frame present on the Interface Plate. Some alignment precision is then lost. In fact, any misalignment of the Interface Plate/PMG with respect to the PBS will misalign the PBS reflecting plane with respect to the system optical axis as the PMG is used as an alignment reference when aligning the BCM within the baseplate. Misalignments of the PMG relative to the PBS will only serve to block a larger fraction of the beams. Below is a picture of the spot array at node$_4$.

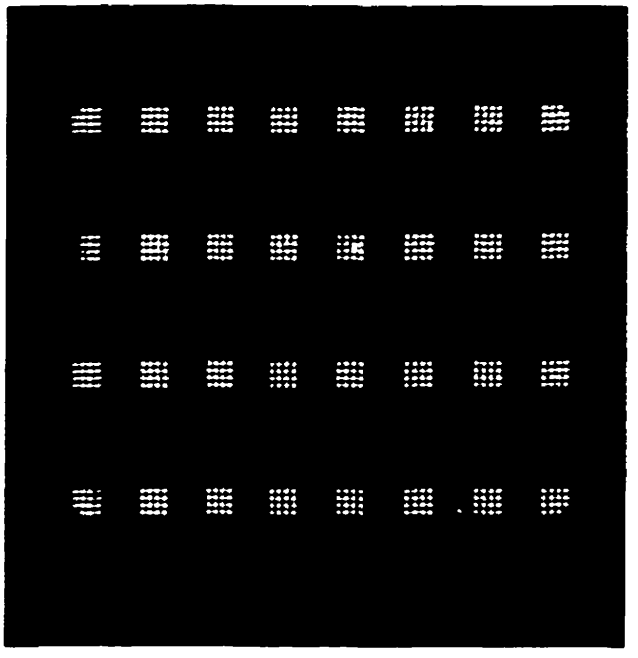

Figure 29. Spot Array at Node$_4$.

Notice how the clusters of the first row of the array are slightly blurred. This is due to the presence of the chamfer that blocks a part of the beams. Figure 30 shows a picture of the

spots as they leave the PBS with the minilenses removed. A schematic diagram of the deviation introduced in the optical beams by the presence of a chamfer is also included. Note how approximately half of the cluster is blocked.

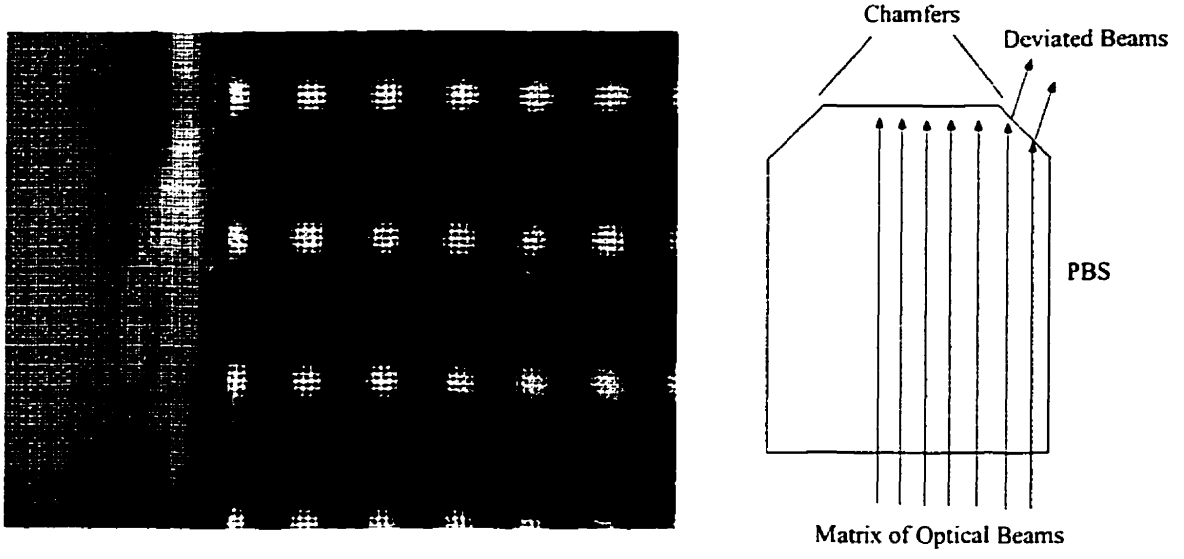

Figure 30. Picture of Spot Array exiting the PBS.

7.3.4.2 PBS Angular Error

The reflecting planes of the PBSs were measured to possess deviations ranging from 0.055° to 0.94° with respect to 45°. These constitute small but extremely important fabrication errors. It is important to remember that the angular error in the beams will increase upon reflection from the PBS and that angular errors will translate to lateral errors at the modulator/detector plane. Figure 31 presents a diagram of the effect of an angular error on the PBS reflecting plane.

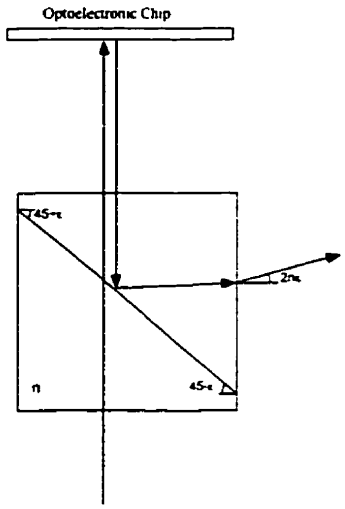

Figure 31. Schematic Diagram of Effect of PBS Angular Error

It was calculated that the deviation suffered by a beam upon propagating in a BCM possessing a fabrication error will be equal to twice the refractive index of the PBS times the angular error present in the PBS [9]. Knowing that the index of refraction of the PBS is 1.76 at 852nm, this can be expressed as:

$$\Delta = 3.52\,\varepsilon \qquad \text{Eq. (1)}$$

Where ε is the angular error in the PBS. A small angular error will be magnified and will lead to a large deviation in the output beam. Note that no deviation will be induced as the beams propagate from an OPS to the modulator plane as no reflection on the PBS takes place. When a beam propagates from the modulator to the detector plane, it will be reflected once by the PBS in each BCM. The resulting total angular deviation at the output of the second BCM can be expressed as:

$$\Delta = 3.52(\varepsilon_1 + \varepsilon_2) \qquad \text{Eq. (2)}$$

Where ε_1 is the angular error in the first PBS while ε_2 is the angular error in the second PBS. Calculations shows that depending on the combinations of BCMs used, the total

beam deviation can vary from 0.5° to 3.7°. This translates to 77μm and 290μm lateral misalignments at the detector plane. As misalignments above 90μm cannot be corrected using the Risley prisms, it was necessary to tilt the BCM using pads of unequal thicknesses in order to direct the spots on to the detector. While this solves the tilt problem for the BCM under alignment, it will worsen it for the next BCM as the induced tilt will add to the fabrication error tilt. Progressively thicker pads and greater induced tilts will be necessary to align each successive node. For example, 500μm pads were necessary to align $Node_1$ to $Node_4$. This meant that the optical axis of $Node_1$ was 500μm higher than the optical axis of $Node_2$. This prevented the ring from being closed.

Below is a picture of the spot array at $node_2$. Figure 32 shows that an entire column of clusters is missing; of the 4x8 array of spots reflected from the modulators at $node_1$ only a 4x7 array of spots can be seen at the detector plane of $node_2$.

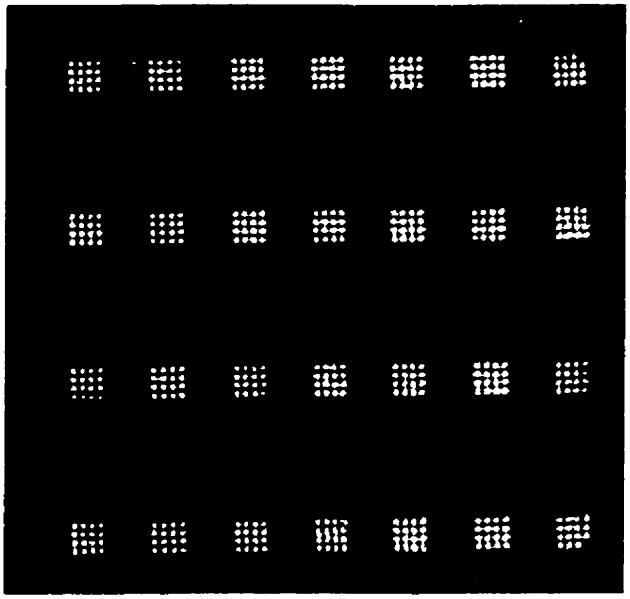

Figure 32. Spots at $Node_2$.

It could be assumed that the loss of a row is due to a chamfer blocking the spots, however, figure 33 which is a close-up of the bottom right cluster, show that the cluster focuses on the wrong targets (the left detector targets instead of the right one). The cluster could not be aligned in its proper target. This is thought to be due to a progressive elevation of the system optical axis due to fabrication errors on the PBS as each stage is assembled.

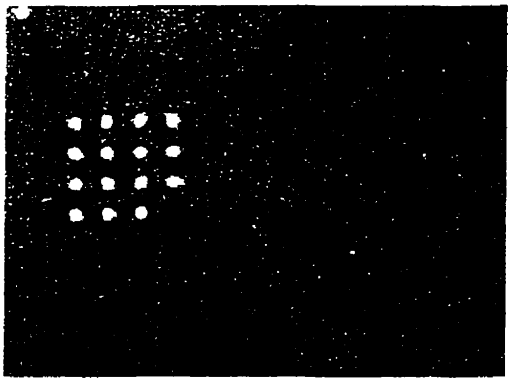

Figure 33. Cluster at Node$_2$.

7.4 Summary

The implementation of a four-stage, scalable optical interconnect for photonic backplane applications was described. The complete backplane consists of four 12f interconnects linked in a ring configuration. Although the optical signals are terminated at each 12f relay, the use of a ring configuration where the first chip is optically linked to the last one means that we are really aligning a 48f optical system. This is one of the most complex optical backplane demonstrators ever assembled.

The main goals of this project were to demonstrate:

1) Passive alignment of the optical modules within the supporting optomechanical structure.
2) Repeatable insertion and extraction of the modules.
3) Stability.

The first goal was not achieved. Fabrication errors in the angle of the PBS reflecting plane induced large misalignments in the beams propagating in the interconnect. Use of a ring configuration meant the tolerance stackup continued throughput the whole 48f system. The presence of chamfers on the edges of the PBS means that part of the beams were blocked or deviated upon propagation. The modules had to be actively aligned and compensation pads used. This greatly complicated system assembly. The use of pads also meant that the optical axis of the system deviated from the mechanical axis of the baseplate. This gap between the baseplate mechanical axis and the interconnect optical axis was perceptible as closing the ring was attempted. There was a difference of about 800μm between the actual position of the beams and where they should have been. This made it impossible to close the ring.

However, the second and third goals of the demonstrator were achieved. Module insertion and extraction were found to be highly repeatable. Once achieved, the system alignment was stable. No drift in alignment could be observed in the course of several days. This is a significant achievement as it means that once aligned, the system stays aligned.

It is believed that the use of highly accurate polarizing beam splitter cubes possessing well-controlled reflecting angles could largely solve the alignment problem at least when assembling short interconnects. The tolerance stackup analysis performed in chapter 5 indicates that the passive alignment of extremely long systems such as a 48f system require extremely severe component tolerances (metrics specifying less than a 0.01% loss must be employed). The passive alignment of a 48f system might be too costly to be practical. It might be appropriate to investigate the use of active alignment techniques when assembling very long systems such as this one in order to decrease costs. For example, multiple sets of Risley prisms properly positioned along the relay (for example, Risleys positioned both before and after the Relay Module) might be used to bring the system into alignment. The use of an active alignment step might be less costly than the use very severe tolerances that guarantee passive alignment. The strength of this design is that once aligned, the system stays aligned.

Alternatively, using a linear configuration instead of a ring configuration to implement the backplane would mean that the last optoelectronic chip would not have to be aligned relative to the first one. This would limit tolerance stackup effects and greatly decrease the requirements on component tolerances and might render passive alignment achievable. However, a more complex bi-directional optical system would be required.

7.5 References

[1] Daniel F-Brosseau, "Design, Implementation, and Characterization of a Kinematically Aligned, Cascaded Spot- Array Generator for a Modulator-Based Free-Space Optical Interconnect", Master's Thesis, McGill University, 1998.

[2] Michael, H. Ayliffe, "Alignment and Packaging Techniques for Two-Dimensional Free-Space Optical Interconnects", Ph.D. Thesis, To be published.

[3] B. Robertson et al., "In Situ interferometric alignment systems for the assembly of microchannel relay systems", *Applied Optics*, Vol. 36, No. 35, 10 December 1997.

[4] F. Lacroix, "Analysis and Implementation of a clustered, scalable and misalignment tolerant optical interconnect", Master's Thesis, McGill University, 1998.

[5] H. P. Herzig, "Micro-Optics: Elements, Systems, and Applications", Taylor & Francis, London, 1998.

[6] Origin Lab Corporation, One Roundhouse Plaza, Northampton, MA, 01060 USA - (800)969-7720 - (413)586-2013.

[7] J. Jahns, "Diffractive Optical Elements for Optical Computers", Optical Computing Hardware, Chapter 6, p. 137-167.

[8] T. K. Woodward, et al., "1-Gb/s Two-Beam Transimpedance Smart-Pixel Optical Receivers Made from Hybrid GaAs MQW Modulators Bonded to 0.8μm Silicon CMOS", IEEE Photonics Technology Letters, Vol. 8, No. 3, March 1996.

[9] W. J. Smith, "Modern Optical Engineering, Second Edition, McGraw-Hill inc., ISBN 0-07-059174-1.

Chapter 8: Future Work and Conclusions

As the demand for bandwidth keeps increasing, electrical-based interconnects are quickly reaching their limits. Frequency-dependent attenuation and crosstalk limit the bit-rate that can be transmitted across interconnect lines while space constraints limit the number of lines that can be laid out between electronic processing elements. Optical interconnects represent an attractive alternative technology for the implementation of dense, high-speed interconnects, as they do not suffer from many of the problems plaguing electrical interconnects. For example, crosstalk and attenuation are largely frequency-independent at optical frequencies. Either guided-wave or free-space optical interconnects can be used to establish links. Arrays of points can be imaged between two planes allowing dense, high-speed, two-dimensional interconnects to be implemented. One advantage of free-space optical interconnects is that the interconnection density that can be established between two planes is limited only by the resolution limit of the imaging lenses. In contrast, the interconnection density of guided-wave systems is limited by the diameter of the waveguides used to guide the light (e.g. 125μm diameter for optical fibers).

However, optics has still not been accepted commercially as an interconnect technology. There is concern regarding the cost and complexity of the optomechanics needed to achieve the very fine alignments necessary to guarantee that the light emitted from the source actually falls on the receiver. This thesis has sought to address some of the questions concerning the practicality of this approach.

The demonstration of a simple-to-assemble, dense and robust optical interconnect would constitute an important proof of the practicality of this technology. The system presented in this thesis addresses these issues through a novel approach; the system uses slow Gaussian beams (f/16) and a clustered design to maximize misalignment tolerances. This in turn relaxes the positioning and packaging requirements for the components, thus simplifying assembly.

This thesis has pursued two sets of complementary goals; the first set is concerned with the demonstration of some desirable optomechanical characteristics for optical interconnects such as passive alignment, repeatability and stability while the second set of goals is concerned with a verification of hypotheses often used in the design and implementation of optical interconnects. Such hypotheses are often used in practice to design optical interconnects despite the fact that little data exists in the literature to warrant their use. It therefore makes good sense to spend some time verifying the accuracy of these models. This will provide a solid engineering foundation for the design of future systems.

The two sets of goals of this thesis are listed below for clarity:

1) Photonic Backplane Demonstrator Goals:

   i) Passive alignment of the optical modules within the supporting optomechanical structure. This would guarantee simple to assemble systems.

ii) Repeatable insertion and extraction of the modules making them easily replaceable in case of failure (this is especially important for the Optoelectronic Chip Module as it houses an active device).

iii) Stability. The system stays aligned without needing adjustment once optimal alignment has been achieved.

2) Design Assumptions:

i) Gaussian beam propagation theory is accurate to calculate misalignment tolerances

ii) There is no simultaneous interaction between multiple tolerance parameters when assembling a system. Tolerance stackup is negligible.

iii) Power losses due to imperfections in components that affect the state of polarization are negligible.

The first demonstrator goal (passive alignment) was not achieved. The modules had to be actively aligned and compensation pads used. This greatly complicated system assembly. The use of pads also meant that the optical axis of the system deviated from the mechanical axis of the baseplate. This gap between the baseplate mechanical axis and the interconnect optical axis became perceptible when closing the ring was attempted. There was a difference of about 800μm between the actual position of the beams and where they should be. This made it impossible to close the ring.

However, the second and third goals (repeatability and stability) of the demonstrator were achieved. Module insertion and extraction were found to be highly repeatable. Once

achieved, the system alignment was stable. No drift in alignment could be observed in the course of several days. This is a significant achievement as it means that once aligned, the system stays aligned and that modules can be replaced upon failure without need to realign the system.

The verification of the design assumptions led to some interesting results. It was shown in chapter 4 that the use of a Gaussian beam model overestimates lateral tolerances by as much as 50%. This means that throughput will be equal to 77% instead of 90% when a component is misaligned to the limit of its tolerance range.

It was demonstrated in chapter 5 that tolerance stackup effects are significant for a 12f system unless extremely severe tolerancing metrics were employed (0.01% power loss for each parameter). Results indicate that there is only a 40% probability of obtaining a throughput of 80% or more when using such a metric to tolerance a 12f system. Note that a 1% power loss metric was employed to set the tolerances for this system. The results can be extrapolated to mean that the passive alignment of extremely long systems such as a 48f system require extremely severe component tolerances (metrics specifying less than a 0.01% loss must be employed). It was argued in chapter 7 that the use of a ring-based configuration for the photonic backplane meant that the four 12f relays effectively behaved as a 48f system for purposes of alignment. The assembly of such a system might therefore be too costly to be practical. It might be appropriate to investigate the use of active alignment techniques when assembling very long systems in order to decrease costs. For example, multiple sets of Risley prisms properly positioned

along the relay (for example, Risleys positioned both before and after the Relay Module) might be used to bring the system into alignment. The use of an active alignment step might be less costly than the use very severe tolerances that guarantee passive alignment. The strength of this design is that once aligned, the system stays aligned.

Chapter 6 has demonstrated that power losses due to imperfections in the components that affect polarization are negligible. Use of commercial components will generally insure less than a 1% power loss except for the PBS.

The combination of a large error on the PBS reflecting plane, the use of a 1% tolerancing metric and of an inaccurate Gaussian beam propagation model to calculate tolerances were probably responsible for the failure to close the ring. It is thought that the use of highly accurate polarizing beam splitter cubes possessing well-controlled reflecting angles could largely solve the alignment problem at least when assembling short interconnects.

The assembly method for this system resembles the current assembly procedures for optical components used in optical networks: components are aligned by hand or with the help of motorized micro-manipulators while coupled power is monitored. They are glued in place once alignment is optimal. Telecommunication grade components aligned and glued using this method have been demonstrated to withstand temperature cycling, drop tests, ageing, etc. Passive alignment might not be absolutely required, i.e. there is no reason why optical interconnects could not be assembled actively and components

glued in place once everything is aligned. The key requirement would then be stability once aligned, which this system has demonstrated.

Alternatively, using a linear configuration instead of a ring configuration to implement the backplane would mean that the last optoelectronic chip would not have to be aligned relative to the first one. This would limit tolerance stackup effects and greatly decrease the requirements on component tolerances and might render passive alignment achievable. However, a more complex bi-directional optical system would be required.

The use of fiber image guides (FIGs) to perform point-to-point interconnections between two planes should also be considered. Their use minimizes the number of alignment steps that must be performed i.e. the FIG need only be aligned with respect to the emitter array and the detector array. The price to pay is a reduced interconnection density. However, note that free-space optical interconnects need to be employed to perform beam combination.

In conclusion, this thesis has demonstrated that free-space optical interconnects can be designed to be mechanically stable and provide repeatable alignment of various optical modules. These constitute key properties to render them acceptable from a commercial point of view.